Protein Diffusion Analysis and Aberration Correction in Single Molecule Localization Microscopy

Ting Yan

Yunnan, China

B.S. in Chemistry, Peking University, 2015

A Dissertation presented to the Graduate Faculty of the University of Virginia in Candidacy for the Degree of Doctor of Philosophy

Department of Chemistry

University of Virginia

May 2021

Andreas Gahlmann

Ku-lung Hsu

David Cafiso

Kateri DuBay

Stefanie Redemann

ACKNOWLEDGEMENTS

As I sit down here to write this, it is hard to believe it's been six years since I landed on this country. Looking back, I could not feel more grateful to people who have given me support in this wonderful journey.

First, I want to give many, many thanks to my advisor Dr. Andreas Gahlmann. I decided to join his research group when I was admitted to University of Virginia. Through ups and downs of my Ph.D. time, he was always patient and supportive. We worked on many projects through the years and he was always showing great enthusiasm, which is truly inspiring. He is a great mentor in that he gives unwavering support and that he is always calm to guide me through the mist of research failures. With his supervision, I was able to develop the ability to design a good experiment, to critically think and to articulate. These skills, I believe, will benefit me greatly in the future. I wish him great success in the future.

It is not possible to tell my story without mentioning my wonderful labmates. I had the privilege of working with former post-doc Dr. Charles Richardson when I first joined the lab. He helped me with genetic engineering projects and later we worked closely on the same project which led to my first authored paper. Charles was generous with his help in work and in life. "Welcome to graduate school", which he always said when our experiments failed, was my motto for the first two years of my graduate school. I also want to thank Dr. Julian Rocha for helping me with coding, single-molecule imaging and random questions. We worked on the same project for a while, during which he taught me how to use the single-molecule localization microscope. He was my desk-mate and good friend. Dr. Mingxing Zhang was my desk-mate in my fourth year. He knew a lot and we had great

conversations on sciences, research and Chinese literature. Eugene Cai, a former undergraduate, patiently walked me through my first Matlab code. Alecia, not just a labmate but also a great friend, is one I will miss. She helped me with cloning, and we had great walks and talks. She gave insightful advices generously. I am very grateful that she is always patient and understanding to me. Ji is the one I discuss microscopy with. We were both excited to learn a newly published microscopy paper and he has an insight in these techniques. Alecia and Ji gave me generous help when I was writing my dissertation, which I really appreciate. Yibo helped me with Rivanna computing system and gave me great advices on genetic cloning. I wish them great success in work and life.

My committee members, Dr. Ken Hsu, Dr. David Cafiso, Dr. Kateri DuBay and Dr. Stefanie Redemann, need to be mentioned here. It is my honor to have them oversee my research.

I also want to express my gratitude to Mrs. Anne Waite, who is my friend and my counselor, and to Ms. Madeleine Hendrick, who is a dear friend and spent a lot time together before she moved away. They helped me learn another culture and supported my greatly all the time. I am very grateful to Johanna J. Loomba, Serena B. Loomba and the Bush family. They shower me with love and support. Johanna is a wonderful friend. I am beyond fortunate to know her since my first year and become her friend. I love her wisdom, kindness, honesty, directness and her cooking, without which I could not survive the last two years at all.

Many thanks are going to Prof. Weihong Li, my favorite professor from undergraduate. As years pass by, we still keep in touch and become close friends. She has been giving unending support, encouragement and love to me.

Of course, I need to give thanks to my family. I could not have led the life I have now without them. I want to tell my younger brother that I will always support him.

There are so many I want to give thanks to, but there is only limited space. I would like to give special thanks to the sitcom *Friends*. It helped me when I was preparing for TOEFL back in China. In these years, whenever I was not in a good mood, it had the power to make me laugh. I could not remember how many times I've watched it. At the very end, I will give the acknowledgement to myself. I know how hard it is for me to fight all the way from an impoverished town in China to another continent on the other side of earth. The fight is not against the environment or other people, but against fear, insecurity and doubt about myself deep inside my heart. I struggled through my Ph.D., and now it is time to tell myself that this battle is ending. The fight will never end and I will still try my best.

ABSTRACT

Single molecule localization microscopy (SMLM) is a powerful tool to measure the spatial localization of molecules with tens of nanometer precision and tens of millisecond time—resolution. When applied to living cells, it can provide the spatial and temporal information of molecular localization and diffusive behaviors of individual proteins *in vivo*. To fully characterize the distribution of molecular behavior, analysis of a large number of individual measurements is required. The work presented here focuses on the accurate extraction of protein diffusive states from experimental measurements using aberration corrected SMLM. The computational analysis framework fits well-sampled experimental distributions. The robustness of this approach is demonstrated using single-molecule trajectories acquired at different exposure times. The diffusive states are resolved. The results indicate that the fluorescent protein mEos3.2 undergoes confined Brownian diffusing in live *Y. enterocolitica* cells. To further the quality and quantity of single-molecule localizations, a phase-retrieved vectorial PSF model is introduced to account for aberrations in ultra-wide fields-of-view imaging. The spatially-variant aberrations in two color channels of a 3D single-molecule microscope are quantified. By computationally correcting spatially-variant aberrations during data post-processing, emitters can be localized with improved precision throughout the ultra-wide field-of-view.

Table of Contents

Chapter 1: Introduction

1.1 Overview

Since the advent of microscopy, it has been widely used in various scientific fields. Its use in biology has made it possible to observe single eukaryotic cells and even smaller bacterial cells which are not observable with the naked eye. However, the resolution of conventional light microscopy, defined as the minimum distance between two distinguishable objects, is limited by diffraction. The diffraction limit, determined by the wave nature of light, is roughly half of the wavelength at the lateral direction, around 200-300 nm if visible light is used, which is two orders of magnitude larger than the size of individual molecules. The diffraction limit had long been a major barrier to observe molecular behavior and inter-molecular interactions with light microscopy.

Fluorescence microscopy is a powerful tool to observe targets of interest in different environments by tagging them with a fluorescent probe. The fluorescent probes provide high specificity, high contrast against unlabeled background and minimal invasiveness. Still, conventional fluorescence microscopy suffers from the diffraction limit. Since 1994, scientists have found ways to surpass the diffraction limit of fluorescence microscopy, i.e., super-resolution microscopy, which was awarded the 2014 Nobel Prize in Chemistry [1-5]. Super-resolution microscopy can be roughly divided into two families.

The first family improves the resolution by engineering the illumination pattern. Such methods include STimulated Emission Depletion microscopy (STED)[1], the REversible Saturable OpticaL Fluorescence Transition microscopy (RESOLFT) family [6-8] and Structured Illumination Microscopy[9]. By forcing molecules encompassing a spot smaller than diffraction limit into a dark state which does not emit fluorescence, STED and RESOLFT microscopy are able to detect the fluorescence signal from the encompassed

spot, thus achieving a resolution below diffraction limit. SIM employs a different methodology by illuminating the sample with a series of phase-shifted patterns to obtain information of higher spatial frequency otherwise unobservable, thus bypassing the diffraction limit.

The second family breaks down the barrier of diffraction limit by localizing individual molecules with a precision and accuracy that is tens of nanometers or even smaller, depending on the magnitude of collected photons and background signals. Such microscopy is termed Single Molecule Localization Microscopy [Fig. 1.1], which includes STochastic Optical Reconstruction Microscopy (STORM) [2], (fluorescence-)Photo-Activation Localization Microscopy (PALM/f-PALM)[3, 4] and different derivatives thereof, for instance, direct-STORM [10]. Structures of interest are densely labelled with fluorescent probes, which can be organic dyes or fluorescent proteins. When a probe is in a fluorescent ON state, its emitted photons are captured on camera, resulting in a distribution of photons called Point Spread Function (PSF). By actively controlling the concentration of these emitting fluorescent probes through different mechanisms, SMLM allows to separate nearby molecules spatially and temporally, avoiding the overlap of PSFs on camera. The spatial information of molecules can be extracted from individual PSFs by fitting them with appropriate algorithms.

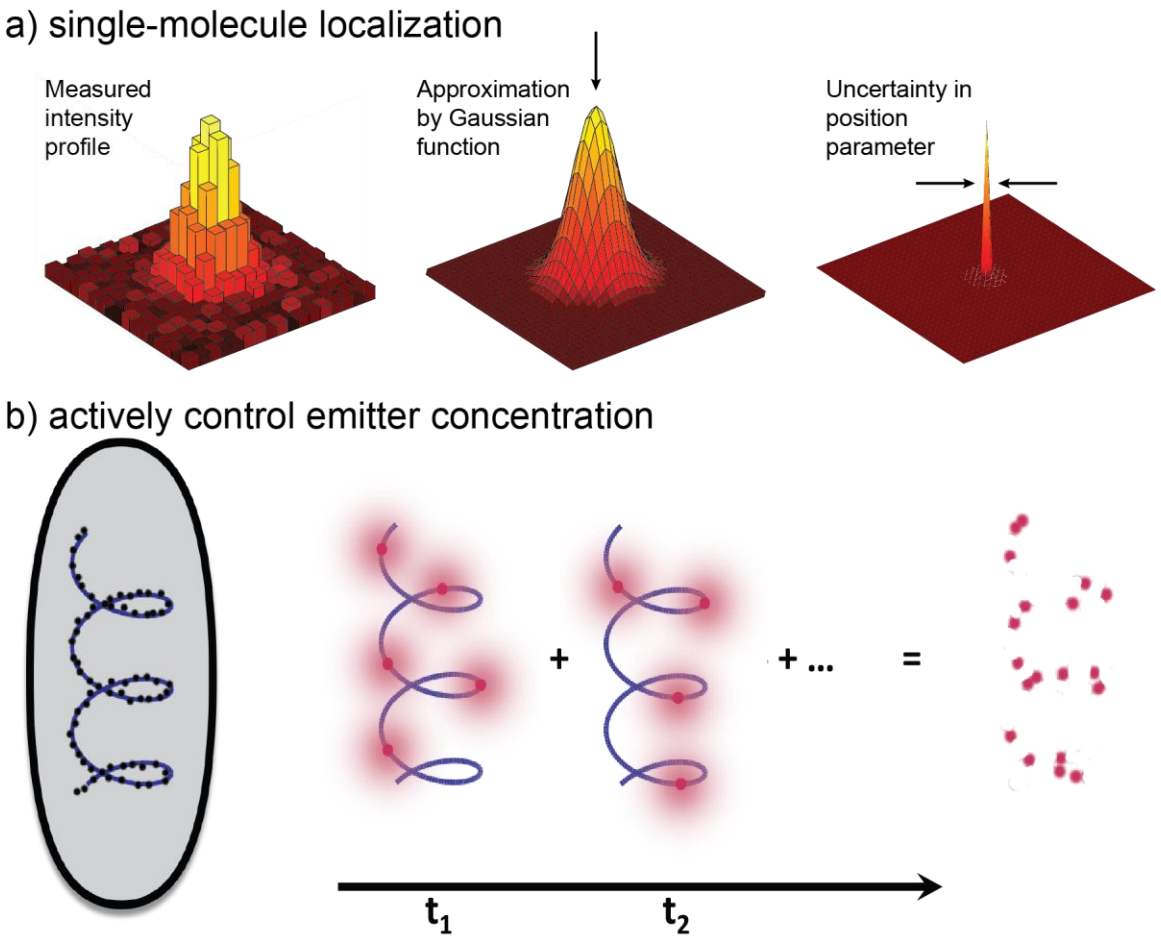

Figure 1.1. the principle of Single-Molecule Localization Microscopy. a) photons from an emitter are distributed on camera detector, resulting in an extended 2D intensity profile, i.e., Point Spread Function. The size of the PSF is dependent on the wavelength and the numerical aperture of the objective lens. By fitting the PSF with an appropriate model, for example the Gaussian model shown here, the center can be measured with a precision at the scale of a few tens of nanometers, an order magnitude smaller than the PSF size. b) by actively controlling the concentration of emitters in fluorescing state, one can separate emitters spatially and temporally. Here a hypothetical structure, densely labeled with fluorophores, within a cell is shown. At different time points, t_1, t_2 and so on, different subsets of fluorophores are detected and localized. By combining all localizations, one can super-resolve the underlying structure. Figure reproduced from ref. [11].

The work in this dissertation is performed on a home-built single molecule localization microscope (SMLM), which belongs to the second family. With the ability to detect and localize individual molecules over time in living cells, we aim to extract single-molecule dynamic information from the localizations. Meanwhile, it is important to study the dynamic behavior of fluorescent proteins for future assessment of their potential use for labeling in live cell imaging. To localize molecules with a good accuracy and precision, an appropriate PSF model is required.

1.2 Single Molecule Localization Microscopy

SMLM has been widely used in different scientific fields and has facilitated many great discoveries. For instance, it enables the mapping of a non-fluorescence process by imaging its competing auxiliary fluorescence reaction and provides quantitative information of reactant adsorption affinities on the surface [12]. Because of the excellent resolution, it has revolutionized the biology field and deepened the understanding of biostructure and biomolecules. By tagging molecules of interest with a fluorescent probe and collecting thousands of frames at high time resolution, SMLM facilitates a deeper understanding of molecular behaviors. Each frame contains PSFs of a subset of densely labeled molecules, which can be fitted to retrieve the spatial information of these molecules. With these localizations, one can construct a super-resolved structure, which contributes to a precise mapping of spatial organizations within a complex structure, such as the nuclear pore complex in U2OS cells [13]. SMLM with the capacity of multicolor imaging facilitates the measurements of protein-protein interactions or the spatial distribution of many proteins [14]. Furthermore, by connecting the localizations of a single molecule from frame to frame,

one can analyze the movement of fluorescently labeled molecules or nanoparticles, leading to observing the conformational change of a molecule during a certain biological process [15] or the movement of molecules in real time [16].

Notably, it requires three-dimensional information to reconstruct a structure and it requires a fourth dimensional information, i.e., time to monitor the movement of molecules. From frame to frame, one can gain the time information of the emitter and the specimen. The key point lies in deciphering the 3D spatial information of a molecule from the PSFs. A regular PSF from an in-focus emitter can be approximated to a Gaussian spot or more accurately, an Airy disc. The lateral information of a molecule can be decoded from the center of PSF. However, due to the high symmetry of PSFs around the focal plane and the quick dispersion of photons when out of focus, it is hard to pinpoint the axial information with good accuracy and precision and the range is limited to less than one micrometer. To overcome this disadvantage of regular PSFs, several forms of microscopy have been developed to enable the extraction of 3D information of emitters. One form is multifocal plane microscopy or biplane microscopy [17]. In this methodology, the emitted photons are collected on two cameras which are focused on different object planes a known distance apart. By combining PSFs on different cameras, the axial information of the emitter can be derived. A second way to encode the axial information is by a 4π interferometric configuration[18]. The wave-particle duality of photon allows a single photon to travel through two distinct paths at the same time and later interference with itself. The detected intensities after self-interference, determined by the optical length difference between two optical paths, can be utilized to decode the axial position of emitters. Many groups employ a different method to encode the axial information, that is to engineer the PSF by

introducing artificial aberration into the optical system. By introducing artificial aberration, the shape of PSF is able to change appreciably relative to axial position of emitter. Double-Helix PSF [19], is one of such engineered PSFs which we employ to encode the axial information of emitters in our microscope system. Briefly, we introduce a 4f system into the optical path and then insert a phase mask in the Fourier plane which is conjugated to the focal plane of objective lens. Through the phase mask, emitted fluorescence photons are split into two lobes instead of the regular PSF. As the axial distance of an emitter to the focal plane changes, the relative angle between these two lobes changes while the intensities of the two lobes stay unchanged or the change is negligible. Thus, from the center of the two lobes the lateral position of emitter is known and from the angle the axial position of emitter is determined. DH-PSF has an improved working axial range of about 2 μm, which is suitable to study molecules inside a bacterial cell.

1.3 Single-Molecule Tracking

Due to its ability to resolve 3D information of molecules or nanoparticles, SMLM has been widely used by many groups to study biological molecules or complex structures. Moreover, unlike other high-resolution methods such as electron microscopy [20] or cryo-electron tomography [21], fluorescence microscopy does not mandate sample fixation, thus enabling collection of real-time images of living cells. Thus, SMLM is an ideal candidate to study the 3D dynamics of molecules in biological sample. One important application is to track the movement of fluorescently tagged molecules, which reveals the spatial and temporal information of molecular behavior. Notably, SMLM is equipped with the power to observe individual molecules, of which the dynamics can be very different from

ensemble-averaged dynamics that are provided by other methods such as fluorescence recovery after photobleaching (FRAP) [22]. Each individual molecule's trajectory can be sampled by connecting its localizations at different time points. From the trajectory, an apparent diffusion coefficient or molecular displacement between different time points can be calculated. When combined with the cell space information, it provides insights into how a molecule moves within a cell. If sufficiently sampled, the distribution of apparent diffusion coefficients or molecular displacements provides a quantifiable measure to study the motion behavior of molecules in the cell. Single molecule tracking with SMLM has been used to study various biological molecules. For instance, Bayles et al. employed PALM to investigate the dynamics of membrane proteins in live cells of plant *Arabidopsis thaliana* [23]. Persson *et al.* used sptPALM to study the diffusion of RNA helper protein Hfq in *E. coli* cytoplasm [24].

If a molecule is moving in a Brownian way, it has long been shown that the mean squared displacement is proportional to the diffusion coefficient at a given time point. However, due to the confinement imposed by the cell membrane, the apparent diffusion coefficient may deviate from the true diffusion coefficient. Further, multiple diffusive states can exist at the same time due to self-interaction or interaction with other cellular components, resulting in a drastic change in the diffusive behavior of the molecule. To resolve the diffusive behavior of molecules, such as the type of diffusion, diffusive state number and respective populations of these states, it requires careful data collection, processing and analysis to extract the underlying information.

In the work presented in this dissertation, the robustness of a framework to extract the diffusive states of fluorescent proteins and the relative abundancy of these states is

validated. First, a library consisting of distributions of different unconfined diffusion coefficients are obtained by simulating molecular diffusion in a confined volume. Then, the library is used to fit the experimentally acquired distribution of apparent diffusion coefficients through linear combination of multiple diffusive states. This approach is used to fit two datasets acquired with different exposure times of the same fluorescent protein and the same result are reached for the two datasets. The results will be described in detail in Chapter 3.

1.4 Optical Aberrations

Powerful as SMLM can be, it does suffer from artefact. The property of fluorescent probes, such as its brightness and on- and off-duration times, fundamentally determines the precision of SMLM. Many important factors should be taken into account, such as noise model, PSF approximation model and possible optical aberrations present in the optical system. Optical aberrations, which distort the shape of PSF and lead to inaccuracy in localizing molecules, results from the instrument itself and the sample. For instance, wavelength-dependent chromatic aberration in the system makes it hard, if not impossible, to focus lights of different wavelengths at the same position, which leads to chromatic shift in both lateral and axial directions [25, 26]. As implied before, photon budget is of key importance to localization precision [27], so current SMLM uses an oil-immersion objective lens with a high numerical aperture to collect as many photons as possible. Experimentally, biological samples are mounted on top of a glass coverslip and immersed in water or water-based medium. This introduces as least one interface between different media with a refractive index mismatch. To be specific, the mismatch is between oil/glass

and the water-based biological sample, which results in spherical aberration. As the depth of imaged emitter increases, sample-induced aberration becomes significant and deteriorates imaging quality.

To correct for the abovementioned factors, a proper localization algorithm must be used and optical aberrations should be experimentally or computationally corrected. To experimentally correct optical aberrations, adaptive optics are usually employed by adding a phase correction component, such as Spatial Light Modulator, in the optical path [28]. To computationally correct the aberrations in the system, piecewise polynomial functions are used to interpolate experimentally acquired PSFs [29] or theoretical models based on scalar or vectorial diffraction theory are used to account for the actual light propagation in the system [30-32].

As mentioned before, to distinguish individual molecules, only sparse molecules are allowed to stay in fluorescent ON state in each frame. To increase the throughput and reduce possible phototoxicity induced by long time exposure to laser, sCMOS cameras with an ultrawide field-of-view are used [33], which enables the simultaneous imaging of many cells. Notably, the aberrations are spatially variant across the field-of-view [34], which increases the difficulty of localizing single molecules with simultaneous high throughput and high precision and accuracy. Local calibration curves can be generated to correct the spatially variant aberration [34]. This method is not satisfactory because it requires many experiments to obtain curves that cover a large portion of the field-of-view or it requires an extra step of interpolation to correct aberration in the space between curves.

In the work we employ a vectorial PSF model to characterize the misalignment of phase mask and the spatially variant aberrations in two color channels of a single molecule

localization microscope. This model provides maps of the magnitude of different aberrations, specifically, Zernike mode 4-15, throughout an ultrawide field-of-view. The maps enable query of aberration magnitude(s) at any location in the field-of-view for localization. This vectorial PSF model outperforms commonly used double-Gaussian model for DH-PSF. The details of the model and the performance of it will be described in Chapter 4.

1.5 Dissertation Overview

SMLM provides a method to pinpoint the positions of individual molecules of interest with a precision and accuracy that is two orders smaller than the diffraction limit. The dissertation will detail the properties and instrumentation of SMLM in Chapter 2. Then I will focus primarily on two aspects of SMLM: its application to track protein diffusion and the characterization of aberrations in the optical system in Chapter 3 and Chapter 4, respectively. Specifically, in Chapter 3, I will detail the calibration of the camera and how localization and single particle tracking are realized, followed by diffusion analysis of the fluorescent protein mEos3.2. Chapter 4 will first describe how we characterize the spatially variant optical aberrations of Zernike modes 4-15 in our system. Then the performance of our model will be compared with double-Gaussian model that is commonly used for DH-PSF, followed by how the model helps optimize the experimental data collection and simulation. Finally, Chapter 5 will discuss the significances and future directions of the described work.

Chapter 2: Single Molecule Localization Microscopy

2.1 Single Molecule Localization Microscopy

Fluorescence microscopy is a powerful tool to study specifically labeled molecules and has been used in many fields. In the field of biology, it provides information about events occurring inside cells, tissues and whole organism in a non-invasive way. However, it is fundamentally limited in its resolution by diffraction. The diffraction limit was first described by Ernst Abbe and is known as [35]:

$$d_{x,y} = \frac{\lambda}{2 \cdot n \cdot sin\theta} \tag{2.1}$$

where d is the diffraction-limited resolution when a light of wavelength λ travels through a medium with refractive index n and converging to a spot with half-angle θ. The portion of $n \cdot sin\theta$ is called the numerical aperture (NA). The resolution, defined as the minimum resolvable distance between two objects, is roughly 200-300 nm when a visible light and high-NA (about 1.4-1.6) are used. The abovementioned number only describes lateral resolution. The resolution along the z-axis is worse than that along x, y-axis and is written as follows [36]:

$$d_z = \frac{\lambda}{n \cdot (sin\theta)^2} \tag{2.2}$$

Many subcellular structures have features that are an order of magnitude smaller than this limit. For instance, the diameter of microtubules are about 25 nm revealed by electron microscopy [37]. Super-resolution microscopy has been developed to overcome this diffraction barrier, allowing a deeper understanding of molecular behavior and interaction in cells.

The first family of super-resolution microscopy is illumination-based, which was briefly described in Chapter 1, so discussion thereof will be omitted here. The work in this dissertation is accomplished with a photoactivation localization microscope (PALM), which belongs to the second family of super-resolution microscopy termed single molecule localization microscopy (SMLM). Different approaches of super-resolution microscopy are thoroughly reviewed [38-41]. The rest of this chapter will discuss several important aspects of SMLM, including its concept, the property of fluorophores, extension to 3D SMLM, localization algorithms, phototoxicity, and photobleaching.

2.1.1 Single Molecule Localization Microscopy

The second family of super-resolution microscopy, termed single-molecule localization microscopy, relies on actively switching fluorophores ON and OFF and then localizing individual fluorophores with high precision, at a so-called "super-resolution" level. This family was first independently developed by three groups and given different names [2-4]. PALM/fluorescence-PALM use photoactivatable or photoconvertible fluorescent proteins, whereas stochastic optical reconstruction microscopy (STORM) was first realized using organic fluorophore pairs Cy3 and Cy5.

Single molecule imaging was firstly realized by Moerner *et al.* at cryogenic temperature [42]. It has been extended to standard microscopy at room temperature [43, 44]. When photons emitted from an infinitely small emitter reach the camera detector, they cannot be focused to an infinitely small point. Instead, they converge, interfere at the focal plane, producing a diffraction pattern, which is the point spread function (PSF). The size of the

PSF is dependent on the NA of the objective lens and the light wavelength. The two-dimensional PSF originating from a single emitter allows one to pinpoint the center of that emitter with a much higher precision well beyond diffraction limit.

When the signal collected is predominately from a static single emitter, i.e., the background noise is sufficiently low, the best localization precision of SMLM for an isotropic emitter at or near the focal plane can be described as [27]:

$$\sigma = \frac{s}{\sqrt{N}} \tag{2.3}$$

Where σ is the lateral localization precision, s is the standard deviation of 2D PSF intensity profile fit with a Gaussian function, and N is the number of photons collected from the emitter. However, this is an over-optimistic assumption. In practice, the background noise and pixilation of camera detectors cannot be neglected, ultimately contributing to the localization precision. Taking all these factors into account, the precision can be described as [27]:

$$\sigma^2 = \frac{s^2 + \frac{a^2}{12}}{N} + \frac{4\sqrt{\pi}s^3b^2}{aN^2} \tag{2.4}$$

Where a is the size of the pixel and b is the background noise. The localization precision can also be experimentally estimated as the standard deviation of repeated localization measurements of the same stationary fluorescent emitter, such as fluorescent beads. Further, the resolution of a microscope is heavily dependent on the localization precision as well as the labeling density, quantified by the Nyquist criterion [4]. It requires the mean distance between neighboring localized molecules to be at least twice as fine as the resolution. To optimize these imaging parameters, one can modulate the laser intensity which directly

affects localization precision and effective labeling density [45]. It is recommended to experimentally optimize imaging parameters for each system being probed.

Localizing with a good precision only is not enough for resolving many biological structure or dynamics since a vast majority of proteins of interest in biological samples has a significantly higher density than one molecule per diffraction-limited volume. In such cases, the fluorescence image of molecules appears as a fuzzy diffraction-limited spot, which is the summation of many overlapping PSFs. The way to surpass this problem is to limit the concentration of emitting molecules so that their PSFs are spatially separated. The discovery of photoactivable fluorescent labels made this possible [46]. It starts with a vast majority of fluorophores in a dark state and then thousands of sparse subsets of fluorophores are excited to fluoresce sequentially in time [2-4]. The sparsity of emitting fluorophores ensures that PSFs from individual emitters don't overlap spatially, while the separation of different subsets in time makes it possible to sample as many labelled molecules as possible in a volume. The accumulated localizations are used to reconstruct a super-resolved structure or reveal the motion of molecules.

2.1.2 Fluorescent Probes

SMLM relies on the sequential activation of a sparse subset of fluorophores which are first in a dark state to ensure that individual emitters are probed. The temporal and spatial separation is fundamentally limited by the employed labelling strategies as well as the physical and chemical properties of the fluorophores, e.g., the brightness, specificity, and photostability etc. Commonly used probes are fluorescent proteins, organic fluorescent

dyes, quantum dots, and hybrid systems which combines a genetically encoded target peptide with a separate fluorophore. Despite their distinct features, all classes of the fluorophores used in SMLM share the same quality that they can be photoactivated, photoswitched, or photoconverted by light of a specific wavelength for detection [47]. Photoactivation is the process during which a fluorophore is activated from a dark state to a bright fluorescent state upon illumination with UV or violet light. Alernatively, photoconvertible fluorophores is capable of being optically transformed from one fluorescence emission bandwidth to another by UV or violet light. In contrast to photoactivatable and photoconvertible fluorophores, photoswitchable fluorophores can be alternatively turned on or off with specific wavelength of light. All of them can be collectively termed optical highlighting[48].

In 1962, green fluorescent protein (GFP) was first discovered by Shimomura et al. from *Aequorea victoria* jellyfish [49]. Later, its spectrum and the chromophore were described [50-52]. Since this initial discovery, fluorescent proteins from other organisms have been reported [53-55]. These fluorescent proteins and their variants provide the capability to observe fluorescently labeled target of molecules against the otherwise dark background. More importantly, they can be genetically encoded together with the protein of interest, which is compatible with live-cell imaging. The genetic fusion of the protein of interest with fluorescent proteins provides high specificity but also may suffer from artifacts such as molecular behavior changes in the molecular behavior of the labelled molecule, resulting in its dysfunction and possibly cell death if the non-functional molecule is required for vital cell process. Aside from the requirement that they should be able to exhibit features of optical highlighting, the brightness, chromophore maturation rate and oligomerization

tendency of fluorescent proteins should be considered. For instance, the fluorescent protein mEos2 provides high photon budget but it can form dimers and high-order oligomers, which are more likely to perturb the function of the protein of interest. This has led scientists to design a truly monomeric variant mEos3.2 [56]. The other disadvantage of fluorescent proteins is that they are ~10 times dimmer than organic dyes, which means a lower resolution. Ultimately, one must consider the trade-off of high-specificity in labelling when using fluorescent proteins with the disadvantages of possible perturbation of function, as well as their relative dimness compared to organic dyes. It is highly recommended to carefully compare genetically modified cells with wild-type cells. In addition, the study of the dynamic behavior of fluorescent proteins is necessary if it is used in living cells, and the possible effect of a fluorescent protein on the behavior of protein of interest must be taken into consideration.

The first use of fluorescent organic dyes in SMLM dates back to the first report of STORM where the photoswitchable fluorophore combination of Cy3 and Cy5 is used [2]. Organic dyes, as well as inorganic quantum dots, exhibit desirable features, such as small size, high brightness, and excellent photostability [57]. However, targeting them to molecule of interest inside the cell is difficult, especially in live cell imaging where the membrane of cells functions as a barrier. Of the commonly used organic dyes, rhodamines have a high potential for intracellular live cell imaging due to their membrane permeability [58]. Moreover, an extra linker is required to connect the label with the target molecule, which adds uncertainty to the spatial relationship between the label and the target molecule. Low labeling efficiency is another disadvantage, which actually affects the resolution according to Nyquist criterion [59, 60]. The bulky size of the linker, in many case

antibodies, prohibits dense labeling. Many of these organic or inorganic fluorophores are not membrane permeable, therefore incompatible with live cell imaging. This restricts their use to cell-surface proteins or fixed cells.

It is ideal if one can combine fluorescent proteins' high specificity with small-sized organic dyes' excellent brightness. The hybrid systems haven't fully achieved the aim yet, but they offer a promising future. These systems combine a genetically encoded self-labeling protein tag or site-specific incorporation of non-natural amino acids in live cells and a small synthetic fluorophore[61-63]. SNAP-, CLIP-, and Halo-tags are used to achieve live-cell staining with fluorescent dyes [64-66]. For example, the Halo-tag, which is a modified bacterial enzyme, can form a covalent bond with synthetic molecules [66]. As is the case of fluorescent proteins, the relatively large size of these tags (~25-30 kDa) can be prohibitive and perturbative. Chemical dye labeling can suffer from high background levels if excess dyes are not sufficiently removed. If multiple wash steps are involved to remove excess dyes, artifacts may be introduced. On the other hand, labeling proteins in the cytoplasm through noncanonical amino acids (ncAAs) requires fixation of sample, as well as additional chemical manipulation and expression of specific orthogonal tRNAs and aminoacyl-tRNA synthetases [67]. Other methods are employed to amplify the fluorescence signal by binding many fluorescent proteins, such the use of the Sun-tag [68]. However, the drawback of bulky size discourages universal implementation.

To choose a labelling method, one needs to consider many factors. For instance, is it *in vitro* or *in vivo* imaging, fixed sample or live cell imaging? Organic fluorophores are easy to use for *in vitro* or fixed sample imaging, and they provide good localization precision for its brightness. However, as stated before, it requires multiple wash steps to eliminate

possible background fluorescence from non-specifically or unbound probes. If it is live cell imaging, the location of protein of interest is important in determining the labelling methods. Nikic *et al.* demonstrated the use of organic fluorophores to label proteins on the cell surface via ncAAs and click chemistry [69]. However, this method can be difficult for proteins inside the cells because the membrane poses a barrier for organic fluorophores. Moreover, the labelling efficiency and specificity of organic fluorophores need to be considered. In the case of intracellular proteins or proteins of unknown location, fluorescent proteins are better candidates for their high specificity through genetic fusion. To sum up, the cons and pros of each kind of labeling must be carefully thought through, and it needs to be experimentally tested.

2.1.3 Axial Position

To fully understand the molecular arrangement or dynamic inside a cell, a vertical z-axis information is needed. This axial information can be revealed by a variety of means. Many microscopes use an oil-immersion objective lens with high-NA to image water-based samples. When the emitter is close to the refractive index mismatch boundary, the evanescent fluorescence signal, also called the supercritical angle fluorescence, can be used to infer the axial position of emitters with a precision down to 15 nm [70, 71]. The fraction of supercritical angle fluorescence to total fluorescence monotonically decreases as the emitter goes deeper into the sample. However, this method can only localize emitters with a distance to the refractive index mismatch boundary less than a wavelength. Recently, the technique has been combined with astigmatic imaging to extend the imaging depth to about 2 μm with a weak anisotropic resolution [72].

The PSF itself contains axial information which can be derived through imaging processing. A defocused PSF is broadened in size compared to an in-focus PSF. However, the size of a regular PSF does not change appreciably when the z-position of the emitter is near focus or when the photons are too dispersed because the emitter is far from focal. Biplane microscopy was used for 3D tracking before its application to SMLM [73]. It derives depth of the emitter by capturing two images set to two different object planes with known distance between them [17]. The ratio of PSF sizes in the two images changes monotonically with the emitter's axial position. It achieves live-cell imaging with a sub-100 nm resolution with a depth of field less than 1 μm without scanning.

Another way to derive the z-position of an emitter is to harness the interferometry along the axial direction with a 4π interferometric configuration[18]. The wave-particle duality of photon allows a single photon to travel through two different z-dependent paths at the same time. These paths are ultimately combined, which results in self-interference of the photon. The detected intensities on different cameras after self-interference, determined by the optical length difference between different optical paths, are utilized to decode the axial position of emitters. The implementation of dual objectives in 4π detection geometry increases the number of collected photons, thus improving localization precision in all dimension. PALM using multiphase interferometry, known as iPALM, achieves sub-20 nm 3D localization resolution with fluorescent proteins. It has demonstrated its superior performance by resolving membrane, microtubules, endoplasmic reticulum and focal adhesion architecture [18]. However, the requirement for self-interference highlights the relatively complex instrumentation of iPALM. It is also sensitive to perturbations of the microscope stage. At its early development stage, the imaging depth was limited to less

than 1 μm. Huang et al. has successfully extended the vertical range to image cells as thick as ~10 μm, increasing its applicability to different systems [74].

A third way to encode axial information is to engineer PSFs so that its shape changes appreciably with an emitter's z-position. One of such methods introduces astigmatism into the optical system by inserting a cylindrical lens in the emission path [75]. The cylindrical lens creates slightly different focal planes for the *x* and *y* directions. In this way, the PSF is changed to from a circular to an elliptical PSF of which the ellipticity and orientation change as the *z*-position of the emitter varies. By fitting the PSF with a 2D Gaussian function, the *x*- and *y*-localizations are determined from the center of the Gaussian function while the z-localization is determined from the widths at *x*- and *y*-directions using a calibration curve. Double-helix PSF is another commonly used engineered PSF [19, 76]. In particular, the regular PSF is replaced by two lobes, which can be approximated as Gaussian spots. The relative angle between its two lobes indicates the axial position while the midpoint of the two lobes determines the x, y-position. Compared to regular PSF, DH-PSF at least has two advantages: 1) extended working distance (~ 2-3 μm) and 2) relatively bright lobes. DH-PSF also provides higher Fisher information for 3D localization [19]. This is done by inserting a wavelength-specific phase mask in the emission pathway. Similarly, by employing different phase masks, PSFs can be engineered to other shapes, such as tetrapod [77], corkscrew [78], bisected-pupil[79] and self-bending PSF[80]. Notably, deep learning approach has been used to design the optimal PSF for high-density emitter case, which can help improve imaging throughout [81]. In this dissertation, DH-PSF is used. In addition to abovementioned advantages, it can be approximated as two

Gaussian spots, which is easy to process. The working distance of it is particularly suitable for imaging bacterial cells.

2.1.4 Emitter Localization Algorithms

PSFs generated from emitting probes are used to infer the emitters' positions by using certain localization algorithms. When a sufficient fraction of all emitters is detected, a super-resolved image can be constructed. The effective attainable resolution is closely related to the precision of the localization algorithm used. Precision measures the random statistical variability of many repeated measurements and it is commonly expressed in terms of the standard deviation of repeated measurements. Here, it is important to note the difference between resolution and precision. Resolution is directly affected by precision, but also is deeply intertwined with the labeling approach. Precision is dependent on many parameters, such as the fluorescence signal, the background photons, noise, the camera pixel size, motion blur from moving molecules and the localization algorithm [11, 27, 82]. Theoretically, the best achievable precision for an unbiased localization algorithm is the square root of the Cramer-Rao lower bound (CRLB), which is given by the inverse of the diagonal terms of the Fisher information matrix [83, 84]. The achievable accuracy of a localization algorithm, which describes how close the measurement is to the truth, has no such a fundamental limit.

Several algorithms are used in the field to localize individual emitters that are well spatially separated in a frame. The simplest estimator is the centroid [27, 85]. QuickPALM is such an estimator which computes the spot position by finding the center of mass of the

PSF [85]. Another way is to localize emitters by computing the radial symmetry center of the PSF, which can lead to systematic error when aberrations exist [86]. The most commonly used method fits the detected PSFs to a model, which is slower than the previously mentioned methods but provides more accurate result. This involves an optimization routine to minimize the mismatch between data and the model. Commonly used estimators are Least Square (LS) and Maximum Likelihood Estimation (MLE) algorithms. LS fits are to minimize the weighted or unweighted squares of the difference between the two-dimensional Gaussian model and actual pixelated data [3, 87]. MLE is a more accurate estimator because it takes into account the signal and the noise model. Using the latter algorithm, emitters are localized by maximizing the likelihood of obtaining the observed data, assuming estimated parameter values, such as photon counts, position and background etc. More importantly, it can achieve the CRLB, the theoretical limit which unbiased algorithms can approach [88]. Others have done exhaustive work comparing LS and MLE [88-90].

To reconstruct a super-resolved image, one has to sample as many fluorescently labeled molecules as possible. This is done by repeatedly exciting a set of sparse molecules over many frames. Individual, non-overlapping PSFs are localized with high precision in each frame and their localizations are pooled, which requires long data acquisition times. Issues of localizing emitters occur when a large PSF is used, or when the labeling density is high, as this leads to overlapping PSFs. To account for these situations, overlapping PSFs are rejected [87, 91] or localized with algorithms specially developed to localize high-density emitters [92-95].

2.1.5 Phototoxicity and Photobleaching

One advantage of fluorescence microscopy is that it is compatible with live cell imaging. Live cell imaging enables the observation of the dynamic processes within cells in real time. For example, Yu *et al.* directly observed real-time expression of yellow fluorescent protein-tagged membrane targeting peptide with single-molecule sensitivity [96]. During data acquisition for SMLM, high-intensity excitation laser or near-violet laser is used for optical highlighting. This may alter the cell physiology or even cause cell death (phototoxicity) [97-99]. It can photoconvert organic fluorophores to a blue-shifted fluorescent molecule [100], or even lead to the loss of fluorescence signal of fluorophores (photobleaching) [98]. This unwanted result is mainly induced by reactive oxygen species (ROS), the generation of which depends on the properties of the fluorophores and the laser dose [101-104]. ROS are varied, and are involved in a range of biological processes such as aging and signaling [105]. Generally, they cause oxidative damage to DNA, proteins, lipids and fluorophores. Antioxidant-rich media are used to reduce the cellular damage caused by ROS, allowing cells to endure a higher laser dose [106]. To decrease sample damage, one can reduce the illumination laser dose by adjusting the laser intensity or the exposure time. Controlled light-exposure microscopy reduces photobleaching and phototoxicity two- to ten-fold by spatially controlling the light exposure time in a confocal microscope [98]. Total internal reflection fluorescence (TIRF) microscopy [107] and light-sheet microscopy [108, 109] are used to limit the illuminated sample volume. Point accumulation for imaging at nanoscale topology (PAINT) ideally can surpass the photobleaching problem because it relies on transient binding of imager to docking site in a medium where the imager is abundant [110]. For the work in this dissertation, we used

epi-illumination with high-intensity laser but limited the exposure of the sample to only a few minutes when imaging live cells. It is confirmed that living cells under such conditions can still divide on the coverslip [111, 112].

2.2 Instrumentation

Since the advent of super-resolution microscopy, it has gained attention from different scientific fields. Due to its wide applicability, the commercialized super-resolution microscopes are now available. For instance, Nikon offers SIM, STORM and STED microscopes. These commercialized products save the customers the time devoted to constructing a complex optical system. However, they lack some flexibility which a home-built 3D single molecule localization microscope can offer. Home-built microscope reduces the cost in maintenance because it can be performed by the research group members when needed. More importantly, its flexibility allows the optical system and the customized software to be tailored to the requirements of specific experiment or projects.

The work in this dissertation is done with a home-built 3D single-molecule localization microscope. It consists of an excitation pathway and an emission pathway. The former is equipped with three different lasers to activate and excite fluorescent proteins according to their absorption spectrum, while the latter is split into two color channels, both containing a 4f system. An additional phase contrast pathway in the microscope converts the phase shift of light through the cells into brightness change, thus allowing us to know the shape of individual cells. The pathways will be detailed in following sections. Optical set-up is shown in Fig. 2.1.

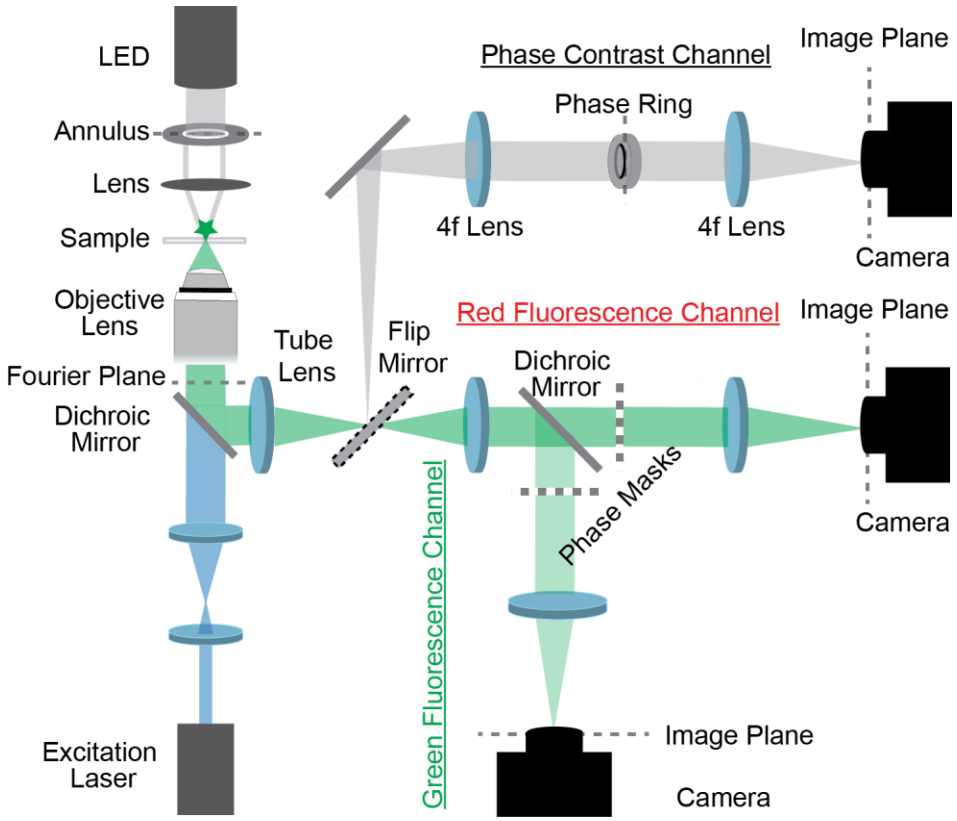

Figure 2.1. Optical set-up of 3D single-molecule localization microscope containing a phase contrast channel. Adapted from [113]. Reprinted with permission. All lasers (here only excitation laser shown) are first expanded and then combined in the same pathway to enter the inverted objective lens. The objective lens also serves as the detection lens. A tube lens is used to form an intermediate image. A dichroic mirror is inserted to split the fluorescence pathway into a 'red' and 'green' fluorescence channels which shares the first 4f lens. In each color channel, a 4f sysem consisting of two lenses enables manipulation of light phases with a wave-specific phase mask. The red LED is used as the illumination light source for the phase contrast optical path. A motorized 'flip-mirror' is used to switch between the fluorescence (colored) and phase contrast (grey) pathways. The lasers, LED, 'flip-mirror' and camera detectors are controlled with a program written in Matlab.

2.2.1 Fluorescence Imaging

During imaging, the sample is activated and/or excited with an emitter-specific wavelength of light which depends on the absorption spectrum of the emitter. After the emitter is excited to a higher energy level, it releases energy in the form of light, also known as fluorescence, when returning to the ground state. The emission wavelength is longer than the excitation wavelength due to non-radiative decay of the photon prior to relaxation to the ground state, resulting in a characteristic Stokes shift. For instance, the commonly used enhanced YFP (eYFP) has a peak absorption at 513 nm and a peak emission at 527 nm [114].

The excitation pathway of the microscope contains three lasers with different wavelengths. They are a 405 nm laser (Coherent OBIS 405), a 514 nm laser (Coherent Genesis MX514 MTM) and a 561 nm laser (Coherent Genesis MX 561 MTM). The 405 nm laser can be used for photoconversion or photoactivation of fluorescent proteins prior to their excitation. The 514 nm laser and 561 nm laser are used to excite fluorescent proteins. Each laser is launched into a separate, but functionally congruous, pathway. The laser is first expanded to create a collimated beam with a larger size than the input beam by two lenses. Then the excitation beam passes through a zero order quarter wave plate to circularly polarize the laser. In 514 nm laser excitation pathway, there is a band-pass filter (Chroma ET510/10bp) to limit the wavelength range in the pathway. All three laser lines are combined by using a set of dichroic mirrors (Chroma T470lpxr and Chroma T525lpxr) and reflecting mirrors. The shared pathway is directed to another dichroic mirror (Chroma ZT405-440/514/561rpc-UF1) before they go into the inverted microscopy objective lens (UPLSAPO 60X 1.4NA). The objective lens projects collimated laser beam onto the

sample, which enables wide-field illumination. It also serves as the detection lens, which collects the fluorescence from emitters within a sample. The sample is mounted on an xyz nano-positioning stage (Mad City Labs), which provides positioning and stability with nanometer precision. Between the sample holder and the objective lens, a drop of immersion oil is needed for best photon collection. The numerical aperture (NA) of the objective lens is given by

$$NA = n \cdot sin\theta \tag{2.5}$$

where n is the refractive index of immersion medium and the angle θ is the maximum half-angle of the light cone within which the light can be collected. As shown previously, the diffraction-limit of the microscope is reversely proportional to NA and the resolution of SMLM is inversely proportional to the square root of collected photon number. To improve the resolving power, it is necessary to use a high-NA objective lens. Specifically, we use an oil-immersed objective lens for which the immersion oil has a higher refractive index (n = 1.518) than water (n = 1.33) and air (n = 1). If necessary, the excitation and emission pathways can be adjusted to accommodate more lasers or color channels. Optical neutral density filters (Thorlabs FW2AND) can be inserted into individual laser lines to adjust the power of input laser.

The emitters within samples are excited and then emit fluorescence photons which are collected by the objective lens. The wave amplitude and phase at the back focal plane contain rich information which can be used to extract the aberrations present in the system as described in Chapter 4. The emission fluorescence then goes through the dichroic mirror (Chroma ZT405-440/514/561rpc-UF1) before it goes into the emission pathway. To limit the amount of scattered excitation photons that enter the emission pathway, a set of filters

are needed. Specifically, they are a 514 nm long-pass filter (Semrock LP02-514RU-25) and a 561 nm notch filter (Semrock NF03-561E-25), for 514 nm and 561 nm excitation lasers, respectively. There is an additional 700 nm short-pass filter (Chroma ET700SP-2P8) in the pathway which is to limit light outside the range of the fluorescence signal. The objective lens is an infinity-corrected objective, which means its image plane is at infinity. This necessitates a tube lens to focus the light beams and form an intermediate image. After the tube lens, there is a "flip mirror", which allows a switch between the emission and phase contrast pathways. When this electronically controlled flip mirror is flipped up, the light goes through the phase contrast pathway, which will be detailed in the next section. When the mirror is flipped down for fluorescence imaging, the fluorescence photons go through the emission pathways. The signal is passed through a 4f system, which consists of two lenses. The two lenses share the same focal plane, i.e., the Fourier plane between them, and it is conjugate with the back focal plane of the objective lens. The first lens performs a Fourier transform to the intermediate image, making the Fourier plane accessible. It allows the utilization of Fourier space information by introducing additional known aberrations into the system. For example, some research groups insert a deformable mirror in the Fourier space to compensate for existing aberrations [115]. In the case of our system, it enables the insertion of a phase mask (Double Helix, LLC) at the Fourier plane of the 4f system [19], which changes the phase of incident photons, thus changing the final PSFs. After the second lens of the 4f system, the photons from an individual emitter are recorded as DH-PSF rather than the regular Gaussian-like PSF on the detector.

As stated before, the microscope has two color channels. This is achieved by inserting a dichroic beam-splitter (Chroma T560lpxr-uf3) in the emission pathway after the first 4f

lens. Based on their wavelengths, photons are split into a “red” and “green” pathway, each with a dedicated detector. An additional 561 nm notch filter (Chroma ZET561NF) is inserted the “red” channel to block scattered excitation laser if any. This dual-color configuration allows quick switch between color channels or simultaneous dual-color imaging.

At last, in each color channel, the photons are projected onto a scientific Complimentary Metal-Oxide Semiconductor (sCMOS) detector (Hamamatsu ORCA-Flash 4.0 V2). The sCMOS camera offers an ultrawide field-of-view (diameters of up to 250 μm in our case) and fast frame rates, which has gained its popularity in imaging field in recent years [33, 116-118]. The ultra-wide field-of-view increases the imaging throughout, at the cost of considerable aberration, especially at the periphery of the field-of-view, which will be addressed in Chapter 4.

2.2.2 Phase Contrast Imaging

In addition to the fluorescence pathways, our home-built microscope has a phase contrast imaging pathway. Phase contrast microscopy, first invented by Fritz Zernike and awarded the Nobel Prize in Physics in 1953, allows cells or structures to be imaged without the need to fluorescently label them [119, 120]. It converts the phase change of light, due to passage through cells into brightness change in the image. The phase change can be caused by the refractive index mismatch between the cellular milieu and the surrounding medium, or even the heterogeneity within cells. For live cell imaging described in this dissertation, the phase contrast pathway provides the outline of bacterial cells and their

positions in the field-of-view. By aligning the cells with emitter localizations extracted from SMLM, we are able to assign localizations to specific cells and connect localizations within the same cell for single-molecule tracking.

A red light-emitting diode (LED) serves as the illumination source and it sits on top of an illumination tower above the inverted microscope stage. After going through a set of lenses, the collimated light goes through an annulus ring. The ring-shaped light then is focused onto the specimen by a condenser. Some of the light travels through the specimen and is scattered in all directions. The scattered light is typically phase-shifted by -90º compared to the unaffected background light. Then the light travels through the objective lens and the tube lens. To use the phase contrast pathway, the flip mirror mentioned in previous section is flipped up. The light is directed to go through a 4f system, at the Fourier plane of which a phase-shift ring is placed. The background light goes through the phase-shift ring and is phase-shifted by +90º, while the scattered light remains unchanged. This results in the background light 180º out of phase relative to the scattered light. After the 4f system, the scattered light and background light will interfere destructively, creating an image with dark cells and light background on the camera detector (Aptina MT9P031).

Chapter 3: Single-Molecule Tracking

3.1 Introduction

Diffusion of molecules is required for cells to perform various functions, such as metabolism, signaling and protein-protein interactions. The molecule of interest may behave differently in its native environment which is different from artificial *in vitro* solutions in a tube. It is challenging to re-create the appropriate proportions of proteins in a tube. Thus, it is of great importance to study the diffusion of molecules in living cells, which can provide important information about the cellular environment and interactions inside a cell. The diffusion of proteins is affected by the crowding of local surrounding environment [121, 122]. It was demonstrated with simulations done by Matsuda *et al.* that crowding led to reduced diffusion coefficient [121]. Additionally, a protein's diffusion can be changed upon interaction with other proteins. For instance, RelA, an important protein in stress adaptation mechanism, was found to diffuse much slower when binding to the ribosome [123]. Fluorescence recovery after photobleaching (FRAP) is commonly used to determine the diffusion of proteins at the ensemble level [124]. For that particular reason, FRAP fails to provide direct information on a single molecule's diffusive behavior. The result from FRAP obscures the heterogeneity of individual protein diffusion and may lead to rare and important events being undetected.

SMLM is able to probe single molecule in space and time in living cells, which makes it a powerful tool to extract invaluable information lost possibly in studies at ensemble level. Combining the spatial and temporal information of a single molecule from SMLM allows one to reconstruct the trajectory for each molecule. The trajectory allows for the calculation the apparent diffusion coefficient or the displacement between time points. When sufficient single molecule trajectories are sampled, it provides the full distribution

of molecular motion in cells. Further, it is possible to decipher the diffusive states and their population fractions when an appropriate statistical analysis method is used. A major objective of single-molecule tracking is to resolve the diffusive states and their fractions. However, this remains a difficult task and requires careful and thorough data analysis.

Single molecule tracking with fluorescent proteins is challenging due to the rather short trajectories compared with bright organic fluorophores. Moreover, an individual molecule could potentially transit from one diffusive state to another in one trajectory. Different from most *in vitro* experiments, confinement imposed by cellular geometry must be considered, especially for bacterial cells which contains a much smaller cytosolic volume than eukaryotic cells [125]. If a single molecule is diffusing in isotropic unconfined space and the diffusion is Brownian (random walk), the mean-squared displacement can be calculated for a trajectory with *N* time points by using:

$$MSD = \frac{1}{N-1}\sum_{n=2}^{N}(x_n - x_{n-1})^2 \, , N \geq 2 \tag{3.1}$$

where x_n denotes localization at the *n*-th time point in the trajectory. Then the diffusion coefficient can be calculated from with:

$$MSD = 2 \cdot Dim \cdot D \cdot t \tag{3.2}$$

where *Dim* = 2 or 3 is the dimensionality of trajectories, *D* is diffusion coefficient and *t* is the lag time. The diffusion coefficient *D* can be extracted as the slope by plotting MSD against lag time *t*. However, when the space is confined, molecules can collide with the boundary and change its direction, thus shortening the distance between two time points. The apparent diffusion coefficient, calculated directly from Eqn. 3.2, therefore is smaller

than the unconfined diffusion coefficient. When the diffusion coefficient is small, the effect of confinement is negligible, making it possible to still use Eqn. 3.2 to resolve the diffusion coefficient [123]. Importantly, confinement cannot be ignored when molecules are diffusing fast relative to the confinement length scale [111]. In a case of molecules diffusing fast in a confined space, the plot of MSD against lag time *t* is no longer linear [126], and it is reported the apparent diffusion coefficient is appreciably shifted toward smaller values than the unconfined diffusion coefficient [111]. The frame rate of single molecule imaging is at the millisecond level, during which fast diffusing molecules can transverse a distance larger than localization precision. As stated in Chapter 2, the localization precision, or the static localization uncertainty is closely related to the brightness of fluorophores, the pixel size and noise. In addition to the static localization uncertainty, movement of molecules adds to the uncertainty because it can blur the PSFs [11]. This dynamic localization uncertainty is given by [127]:

$$\sigma = \sigma_0 \sqrt{1 + \frac{D_0 t_E}{s_0^2}} \tag{3.3}$$

where σ_0 is the static localization uncertainty, D_0 is the true unconfined diffusion coefficient, t_E is the camera exposure time and s_0 is standard deviation of a static PSF size. It is obvious from Eqn. 3.3 that the dynamic localization uncertainty is larger than the static localization uncertainty and closely related to the diffusion coefficient D_0.

There are several methods that have been developed for single molecule tracking [24, 111, 126, 128-135]. The distribution of displacements or apparent diffusion coefficient, mean-squared displacement (MSD), probability distribution function (PDF) or cumulative distribution function (CDF) of apparent diffusion coefficients are commonly used to

resolve the diffusive states and their fractions. For example, to determine the diffusive states of tRNA, Plochowietz *et al.* fit the distribution of apparent diffusion coefficient to two Gamma-distributions [131]. Chen *et al.* employed an inverse transformation method to map 2D and 3D trajectories in confined space to trajectories in unconfined space [132]. Yet, there is no consensus in the field as to the best method or an objective way to determine the number of diffusive states.

Previous work from our lab developed a framework to resolve the diffusive states of proteins, their population fractions and in some cases even the timescale of the transition between states [111, 113]. By simulating realistic images of protein diffusing in a confined cylindrical space and subjecting these simulated images to the same localization and tracking algorithms as experimental data, the authors acquired the distributions of apparent diffusion coefficient for different unconfined diffusion coefficients. These distributions were combined and interpolated so that it enabled the generation the distribution of apparent diffusion coefficients for any unconfined diffusion coefficient within a reasonable range. The distribution of apparent diffusion coefficients from experimentally acquired images was then fit to a linear combination of a few distributions. This resolved the number of diffusive states and the coefficients of linear combination represented the population fractions of these states. The authors also compared the performance of this method in resolving multiple states using simulated 2D or 3D single molecule trajectories. Interestingly, they found that tracking with 2D data yielded slightly (3% - 7%) more accurate estimation. In living cells, molecules may bind to or dissociate from other cellular components, switching between diffusive states. A new method, termed time-averaged diffusion (TAD), was proposed to determine the time scale of molecules transitioning

between states from simulated camera-based tracking or MINFLUX tracking data. By changing the number of averaged displacements and determining the rate of change of fitting parameters, it is possible to estimate the timescale of diffusive state transitioning.

Experimentally acquired distributions of diffusing fluorescent proteins eYFP and mEos3.2 were both fit to a single diffusive state, validating this framework [111]. This is important for the field in that it demonstrates the nonperturbative behavior of eYFP or mEos3.2 as a label in addition to their high specificity. In fact, the capability of this workflow was first demonstrated before the workflow was published when it was used to resolve diffusive states of fluorescent protein-tagged proteins in pathogenic *Yersinia enterocolitica* [136]. However, there are several aspects that need to be more fully explored. How accurately can an unconfined diffusion coefficient be estimated with this framework? What is the closest two diffusion coefficients that the method can resolve? What is the optimal range of unconfined diffusion coefficient that can be resolved with confidence with this framework? The authors simulated and experimentally acquired images with an exposure time of 25 ms but will the same conclusion be reached with a different exposure time? Here in the work presented in this dissertation, an attempt to address the last question was performed.

3.2 Single Molecule Localization

When a fluorescently labelled sample is mounted on the single-molecule localization microscope which is detailed in Chapter 2, after repeated photoactivation or photoconversion and excitation, we obtain raw images from the sCMOS camera(s). The raw images first are in digital counts and must be converted to electrons. Moreover, they

contain not just signals but also background and noise. It requires thorough analysis to extract possible information. Mostly, a package of Matlab code is utilized to perform the analysis. The code is modified from Easy-DHPSF code from the Moerner lab at Stanford University [137]. This section will describe the initial imaging processing steps which produce localizations correlated with cells.

3.2.1 Camera Calibration

As described in Chapter 2, maximum likelihood estimation (MLE) achieves better accuracy and precision than least square algorithm. The use of MLE requires the knowledge of the signal and noise model. In an imaging system, the noise is contributed by various sources and will be described later.

Electron-multiplying charge-coupled devices (EMCCD) are commonly used for SMLM for their low read-out noise. However, the field-of-view size and frame rate are limited. Scientific Complementary Metal-Oxide-Semiconductor (sCMOS) cameras offer a larger field-of-view and faster reading speed. Its use in localization microscopy was first demonstrated in 2011 [138]. Its superior performance of sCMOS over EMCCD was also demonstrated in SOFI imaging modality [139].

When photons arrive at a camera pixel, they are converted to electrons at some probability, termed the quantum efficiency. The camera-recorded electrons are converted to digital counts in output image. The conversion factor from electrons to digital counts is gain. For example, a gain of 1.8 AU per photon means that each photon results in 1.8 arbitrary units or digital counts in a pixel. For EMCCD, the gain is uniform for every pixel.

Unfortunately, it is not the case with sCOMS. Each pixel of sCMOS has a unique gain and a different noise variance. Thus, it is necessary to calibrate the camera carefully. In the following part, I will describe the theory briefly and describe how the camera is calibrated.

For each pixel in sCMOS camera, the signals and noises are related through:

$$S_C = gS_E \tag{3.4}$$

and

$$N_C = gN_E \tag{3.5}$$

where S_C is the signal measured in count units, S_E is the signal recorded in electron units, g is the pixel-dependent gain to be characterized, N_C and N_E are the noise in count units and electrons, respectively. The noise comes from several sources, such as shot noise (σ_E), read-out noise (R_E) and some additional noise (σ_o). Shot noise arises from the quantum nature of photons arriving at the camera pixels, whereas read-out noise originates from the uncertainty during conversion between camera recorded electrons and digital counts. The different noise sources are independent of each other. They add up to the total noise in units of electrons:

$$N_E^2 = R_E^2 + \sigma_E^2 + \sigma_{o,E}^2 \tag{3.6}$$

The quantum nature of photons controls the shot noise which obeys the laws of the Possionian statistics, which means that square of the standard deviation is equal to the mean value. Thus, we have

$$\sigma_E^2 = S_E \tag{3.7}$$

and Eqn. 3.6 can be re-written as

$$N_E^2 = R_E^2 + S_E + \sigma_{o,E}^2 \tag{3.8}$$

We can further make substitutions using Eqns. 3.4 and 3.5 and get:

$$\frac{N_c^2}{g^2} = \frac{R_c^2}{g^2} + \frac{S_c}{g} + \frac{\sigma_{o,c}^2}{g^2} \tag{3.9}$$

which then gives:

$$N_c^2 = R_c^2 + gS_c + \sigma_{o,c}^2 \tag{3.10}$$

If we have a line in which N_c^2 is the *y*-axis, S_c is the *x*-axis, we can get the gain by calculating the slope of the line. In practice, the intensity of LED illumination was changed to obtain images at different signal levels by using optical density filters. For each pixel, the mean and standard deviation give S_c and N_c. By plotting N_c^2 against S_c, we obtained the gain by finding the slope. The extra noise $\sigma_{o,c}$ is not random and can be removed. When $S_c = 0$, the point where the line hits the y-axis is readout variance R_c^2. After all, the noise can be modeled as a combination of Poisson-distributed shot noise and Gaussian-distributed pixel-dependent readout noise. The calibrated gain and noise are later used in all localization analysis and simulation in this dissertation.

3.2.2 Point Spread Function Fitting

With the carefully calibrated pixel-dependent gain and read-out noise, raw images in counts are converted to images in photons. Offset, which can be experimentally acquire is first subtracted from images. As detailed in Chapter 2, we use a phase mask to engineer a regular PSF to a double-helix PSF (DH-PSF). A DH-PSF contains two lobes rotating

around their center and the relative angle between them depends on the z-position of emitter. A calibration curve is obtained for each experiment to find the angle-z relation. The calibration is done by scanning a fluorescent bead over an axial range (~ 3 μm). This also produces a series of template images of DH-PSFs with different angles. A template matching step is performed to find where the DH-PSF candidates are by matching the background-subtracted images and templates in their frequency space. Finally, the potential DH-PSFs are fit using a double Gaussian model.

Here, a median background estimator is used to find the background photons in each pixel [113]. It is tempting to subtract a uniform background across the field-of-view, which, however, is not the case in real imaging. Sources of background includes light from the illumination laser and inherent cell auto-fluorescence. The latter one can be bleached quickly, while the former one presents a Gaussian intensity profile. The median background estimator finds the median value of each pixel using a rolling window of 100 frames surrounding the frame of interest. The used fluorescent proteins in this work are sparse and moving inside live cells. On average, they last for about average 6 frames. Therefore, at a certain pixel, most of the 100 frames contain only background. The median value is representative of such a background. When the found background is subtracted, single-molecule signals remain.

The modified Easy-DHPSF package is able to perform both least-square (LSQ) estimation and maximum likelihood estimation (MLE). Of these two estimation methods, MLE is able to produce more accurate result, given that the noise model is carefully calibrated. MLE finds the localization by maximizing the likelihood of the data under the double Gaussian model. Fit localizations are first filtered by examining lobe distance, lobe

intensity ratio, lobe size and photon counts. During any imaging experiment, a fluorescent bead is placed within the field-of-view together with cells. It serves as a fiducial label to calibrate the stage drift. Then all drift-corrected localizations are subject to further analysis, such as correlation with cells.

3.2.3 Cell Registration

To assign the localizations resolved above to individual cells correctly, it is required to find the cell position and correlate cells with localizations. The SMLM microscope has a phase contrast channel that captures the cell positions in the field-of-view. Open-source OUFTI is used to find the cell outlines from the phase contrast image [140]. OUFTI can automatically find most cell outlines correctly. If necessary, researchers can manually modify, delete or add cell outlines. Single-molecule localization are registered to the cell outlines by a two-step 2D affine transformation using Matlab built-in function “cp2tform”. In the first step, five pairs of control points are manually selected to perform the initial transformation. A pair of control points consists of estimated cell poles from single molecule localizations and cell outlines. After the first transformation, cells containing less than 10 localizations and localizations that are not within any cells are discarded. The center of mass of remaining single molecule localizations and that of remaining cell outlines are then used for a second transformation, which used a larger set of control points. This gives more accurate transformation and guarantee that only single molecule localizations within cells remain.

3.3 Diffusion Analysis

3.3.1 Single-Molecule Tracking

To calculate the apparent diffusion coefficients of single molecules, the localizations within a cell in subsequent frames were linked into trajectories. A threshold of 2.2 μm was used to prevent unrealistic long trajectories, as used in [113]. This threshold was determined by calculating the longest distance a molecule diffusing at D = 20 $\mu m^2/s$ can traverse in 25 ms duration with an addition of a 25% buffer accounting for cell registration error. Short trajectories with less than 4 localizations were discarded for further analysis. Additionally, if two or more single molecules were present in the cell at the same time, the trajectories they were in were discarded to avoid linking problem and misassignment of localizations.

The MSD for each trajectory was calculated according to Eqn. 3.1. The apparent diffusion coefficient, D* was then calculated using:

$$D^* = \frac{MSD}{2 \cdot Dim \cdot t} \tag{3.11}$$

where Dim the dimensionality and t is the exposure time. Specifically, Dim = 3 and t is 25 ms or 10 ms, depending on the data acquisition parameters. It is important to note that the apparent diffusion coefficient D* can be different from the true diffusion coefficient due to localization uncertainty and confinement. To account for these factors, we simulated noised and motion-blurred images of diffusing molecules in confined rod-shape cell volume, which is detailed in the following section.

3.3.2 Monte-Carlo Simulations

The work in this dissertation follows the same workflow as in ref. [111] and ref. [113] but with slight modifications. In the work presented here, a library of CDFs of apparent diffusion coefficients was constructed by simulating images with 10 ms exposure time and localizing them with Easy-DHPSF. For each unconfined diffusion coefficient, 5000 tracks are simulated and each track consists of 6 localizations. The starting location of each track is randomly chosen in a confined cylindrical space (radius = 400 nm, length = 5 μm) to mimic confinement in a bacterial cell. In the duration of 10 ms of each frame, random walk of molecules is in a short time interval of 100 ns. This means that in a 10 ms duration, a single molecule changes its location for 100,000 times. To account for the effect of motion blur, 50 locations are used to simulate DH-PSFs, which are summed to get the frame for a 10 ms duration. The total signal of each frame is drawn from a normal distribution which centers at 2000 photons and has a standard deviation of 100 photons. A background of 13.5 photons per pixels is added to the simulated images. Poisson noise and Gaussian read-out noise are added. Then the frames are converted to be in unit of counts using the camera gain. The Gaussian read-out noise and the gain are experimentally calibrated as described in Section 3.2.1. With the discrete distributions, a two-step interpolation is performed to enable query of CDF for any unconfined diffusion coefficient within a range of 0.01-20 $\mu m^2/s$.

In addition to adding more simulated distributions to the library, several modifications were made. The first modification is how to redirect molecules back into cells. The confined cylindrical space imposes finite boundary to molecular diffusion. The random starting point and short interval makes it possible to sample all the space in the volume.

The predetermined location, calculated from unconfined random walk, can be placed outside the volume. In that case, the intersection point *x* where the diffusing molecule collides with the boundary is found and the length outside the volume *l* is calculated. The molecule is redirected into the volume from *x* and the distance it covers before next location is equal to *l*. Different from light being reflected at an interface, the redirection of molecule happens at a random angle as long as the molecule is directed back into the volume.

The second modification is how to find the 50 locations. To avoid sampling in a biased way, the 50 chosen locations are evenly spaced. Specifically, the exposure time duration is evenly divided in to 50 short time intervals. The locations at the center of the time intervals are used to simulate DH-PSFs.

The third modification is interpolation methods. As stated before, a two-step interpolation is incorporated in the workflow of simulation. The first step interpolates and smooths the empirical CDFs of apparent diffusion coefficient. The second step interpolates these curves along the unconfined diffusion coefficient direction. To avoid over-interpolation, the interpolation method is changed at certain unconfined diffusion coefficient D. At the first step, when the unconfined diffusion coefficient is smaller than the chosen D, a one-dimensional interpolation "interp1" function in Matlab is used with the "spline" method. When the unconfined diffusion coefficient is larger than the chosen D, a Matlab built-in function "csaps" is used and the value of *p* is 0.95 (arbitrarily chosen). Specifically, in both 10 ms and 25 ms cases, D is 2 $\mu m^2/s$. The change of method at D = 2 $\mu m^2/s$ is based on empirical observation. In Fig. 3.1, all the CDFs of all Ds used for simulation are shown. As D increases, the curve shifts to the right. The second step uses the "natural" interpolation method in "scatteredInterpolant" Matlab function. After the

two-step interpolation, we are able to get a smooth CDF map [Fig. 3.2], which enables query of cumulative probability at a given apparent diffusion coefficient for a certain unconfined diffusion coefficient. The quality of interpolation is quantified by calculating the RMSE for unconfined diffusion coefficients used for simulation [Fig. 3.3].

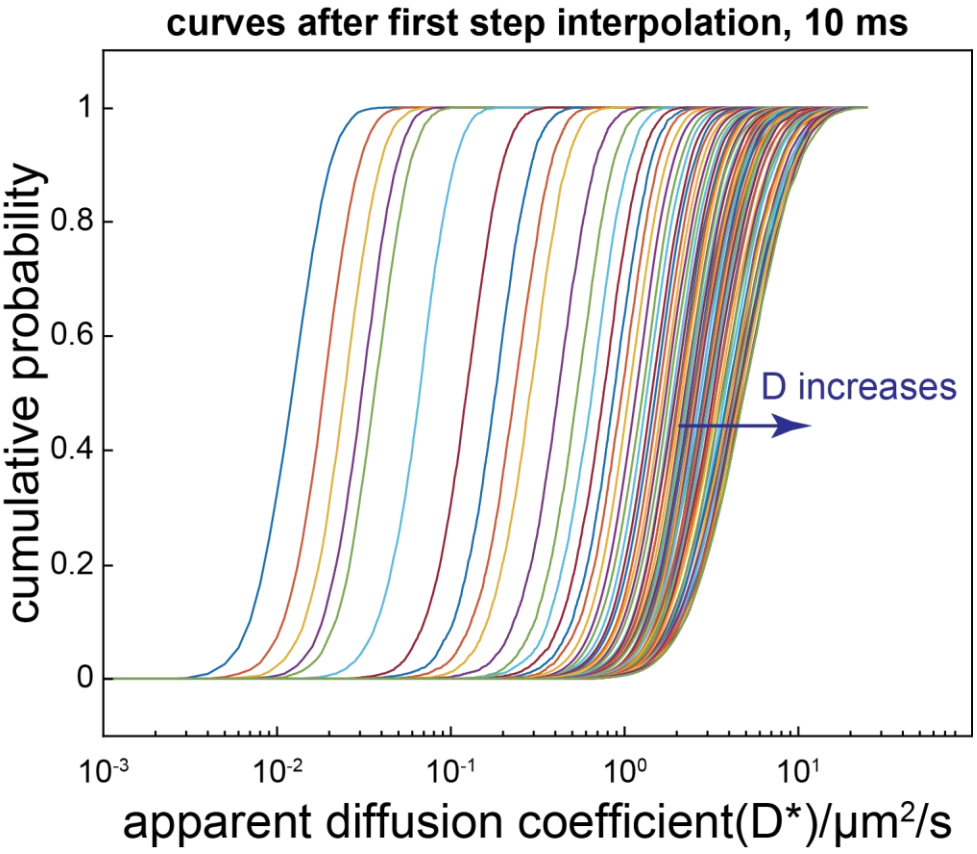

Figure 3.1. Curves after first step interpolation. D denotes the unconfined diffusion coefficient, while D* is the apparent diffusion coefficient. The simulation uses 68 different unconfined diffusion coefficients ranging from 0.01 – 20 $\mu m^2/s$. As the unconfined diffusion coefficient increases, the curves right shift. These curves are used for subsequent interpolation.

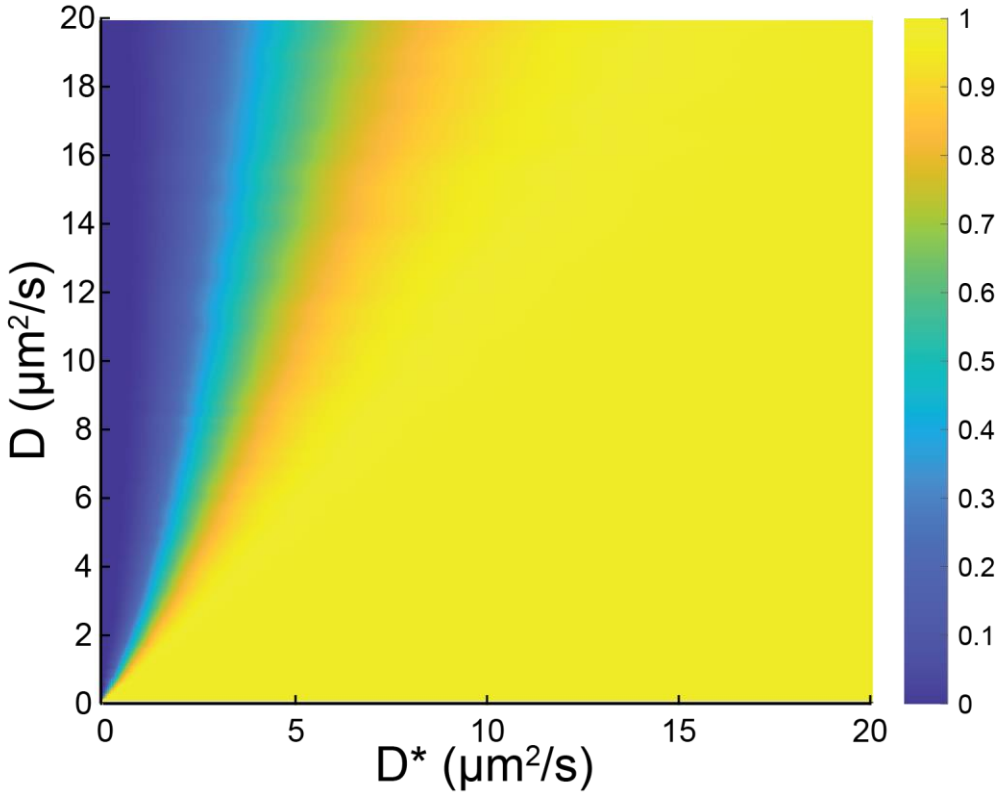

Figure 3.2. The CDF surface from simulated data with an exposure time of 10 ms. The color indicates the cumulative probability at a point (D*, D). From this surface, the CDF of apparent diffusion coefficient D* for a certain unconfined diffusion coefficient D can be queried for further data fitting.

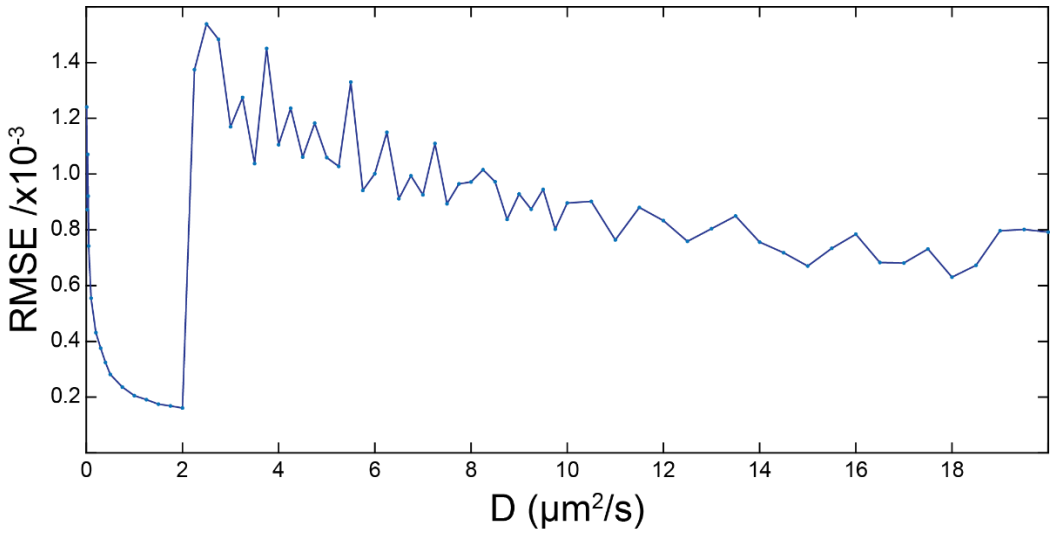

Figure 3.3. Root mean squared errors (RMSE) at every unconfined diffusion coefficient D used for simulation. For each D, an empirical CDF can be obtained from simulated images while an interpolated CDF can be queried from the surface in Fig. 3.2. They are compared and RMSE is calculated. When $D \leq 2$ $\mu m^2/s$, one-dimensional spline function is used. When $D \geq 2$ $\mu m^2/s$, a different function, cubic smooth spline function is used. The change of interpolation method is based on empirical observation to avoid over-interpolation. RMSE used to quantify the quality of the used spline method, increases substantially where the spline method changes.

3.3.3 Diffusion Coefficient Data fitting

The procedure to resolve the diffusive states and their population fractions is detailed in previous work [111]. Briefly, the CDF of apparent diffusion coefficients is fit as a linear combination of CDFs of simulated data. A periodically sampled array of simulated CDFs queried from the interpolation function described in Section 3.3.2 is used at first in a constrained linear least-square fit. This step provides an initial parameter vector which contains diffusion coefficient(s) and population fraction(s). Then diffusive states are

combined or split. A k-fold cross validation and nonlinear least-square fitting are performed to find the best parameter vector and fitting error for each data sub-set. Specifically, the full dataset is divided into k = 5 equal-sized subsamples. The parameter vector with least error is used for a last time nonlinear least-square fitting to achieve the final fitting result. All nonlinear least-square fitting uses "fmincon" function in Matlab. To quantify the uncertainties in the fitting parameters, bootstrapping is performed. Notably, states with unconfined diffusion coefficient $D < 0.5\ \mu m^2/s$ are not refined but combined and assigned to slowly diffusing or stationary molecules.

3.4 Experimental Procedures

3.4.1 Bacterial Strains and Plasmids

Plasmids for the expression of exogenous fluorescent proteins are derived from arabinose-inducible pBAD vectors.

A mEos3.2-N1 plasmid, gifted by Michael Davidson (plasmid number 54525; Addgene, Watertown, MA), is used to amplify the coding sequence of mEos3.2 gene. the PCR product is purified using a gel purification kit (Invitrogen, Carlsbad, CA). Then both PCR product and the pBAD backbone are digested with *Eco*RI and XhoI restriction enzymes (New England Biolabs). The digested gene sequence and backbone are ligated using T4 DNA ligase (New England Biolabs).

The pBAD-mEos3.2 is transformed into competent *E. coli* TOP10 cells. Only positive colonies on Luria broth (LB) agar (10 g/L peptone, 5 g/L yeast extract, 10 g/L NaCl and 1.5% agar) (Thermo Fisher Scientific) containing ampicillin (200 µg/mL) (Chem-Impex

International, Wood Dale, IL) are selected for PCR screening to confirm the presence of the correct insert using GoTaq DNA polymerase (Thermo Fisher Scientific). Plasmid pBAD-mEos3.2 is extracted from *E. coli* cells using a plasmid miniprep kit (Thermo Fisher Scientific) and then sequenced by GENEWIZ (South Plainfield, NJ) before electroporation into *Yersinia enterocolitica* cells. Transformed *Yersinia enterocolitica* cells are plated on LB agar containing ampicillin and 2,6-diaminopimelic acid (dap) (80 µg/mL) (Chem-Impex International, Wood Dale, IL). Positive colonies are picked, cultured and made into freezer stock containing 15% glycerol.

3.4.2 Cell Culture

One day before imaging, cells are inoculated from a freezer stock into media. *Y. enterocolitica* cells are cultured in brain heart infusion (BHI) media (Sigma-Aldrich, St. Louis, MO) containing ampicillin (200 µg/mL), nalidixic acid (35 µg/mL) (Sigma-Aldrich, St. Louis, MO) and 2,6-dap (80 µg/mL). They are grown at 30℃ overnight with shaking. After overnight culture (about 17 hours), 300 µL culture is diluted into 5 mL fresh media and grown at 30℃ for another hour. They are induced with D-arabinose (Chem-Impex International, Wood Dale, IL) at a final concentration of 0.2% (w/v) for another 3 hours at 37℃ in water bath before mounting on microscope for imaging.

3.4.3 Single Molecule Imaging

Cells are pelleted by centrifugation at 7200 × g for 3 min and washed three times with M2G media (4.9 mM Na_2HPO_4, 3.1 mM KH_2PO_4, 7.5 mM NH_4Cl, 0.5 mM $MgSO_4$, 10 µM $FeSO_4$, 0.5 mM $CaCl_2$ and 0.2% glucose (w/v)). The pellet is then suspended in about 200 µL M2G containing 2,6-dap (80 µg/mL) and tetraspeck fluorescent beads (Invitrogen) as fiducial markers that are diluted at a ratio of 1:10000 (v/v). Cells are placed between 1.5-2% agarose pad (w/v) (Thermo Fisher Scientific) and coverslip.

The SMLM set-up is detailed in Chapter 2. Photoconvertible fluorescent protein mEos3.2 [56] is an appealing probe for localization microscopy for its high photon budgets and weak dimer tendency in addition to the high specificity of genetical labelling. The protein is photoconverted from green form to red form with illumination of blue light, i.e., 405 nm laser in the case (~20 W/cm^2) and excited with 561 nm laser (~300-500 W/cm^2). The fluorescence emission is mostly collected in “red” channel. Up to 20,000 frames are collected per field-of-view. For each field-of-view, after single molecule imaging, a phase contrast image is collected.

3.5 Results

To compare the diffusive behavior of the fluorescent protein mEos3.2 at different exposure times, images of 25 ms exposure time and 10 ms exposure time were collected. The distributions of apparent diffusion coefficient D* are compared [Fig. 3.4].

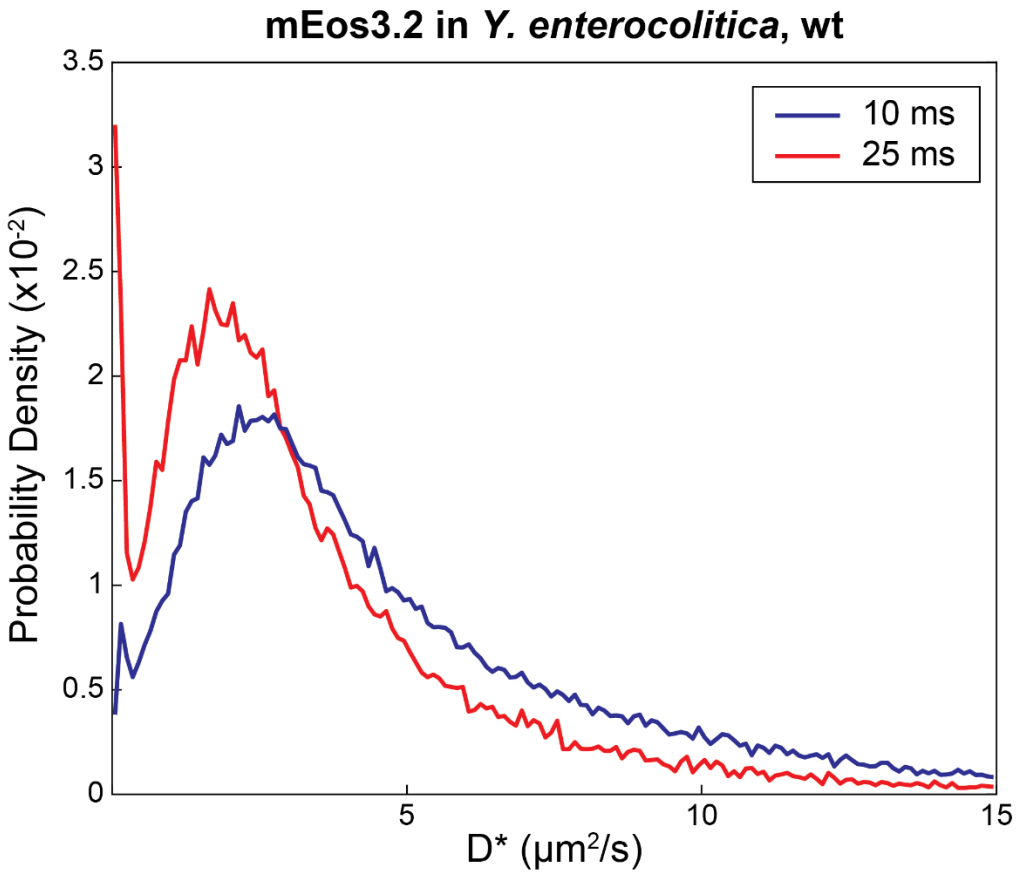

Figure 3.4. Overlay of apparent diffusion coefficient (D*) distributions. The distribution of apparent diffusion coefficient of 25 ms exposure time (N = 39301) presents more stationary population and less fast diffusing population than that of 10 ms exposure time (N = 105531).

We notice that the two distributions reach their peaks at roughly the same D*, about 2 $\mu m^2/s$. Notably, the distribution of 25 ms exposure time has more slow diffusing population and less fast diffusing population than that of 10 ms exposure time.

The difference between distributions can be attributed to the different amount of motion blur effect. First, we compare the distributions of apparent diffusion coefficient of simulated data with different exposure time. It shows that the distributions of 10 ms

exposure time is right shifted compared to the distribution of 25 ms exposure time [Fig. 3.5]. This comparison demonstrates that shorter exposure time has better detection efficiency for fast diffusing molecules. It is also obvious that the distribution of apparent diffusion coefficients is left shifted with the peak probability at D* smaller than the unconfined diffusion coefficient, consistent with previous work [111].

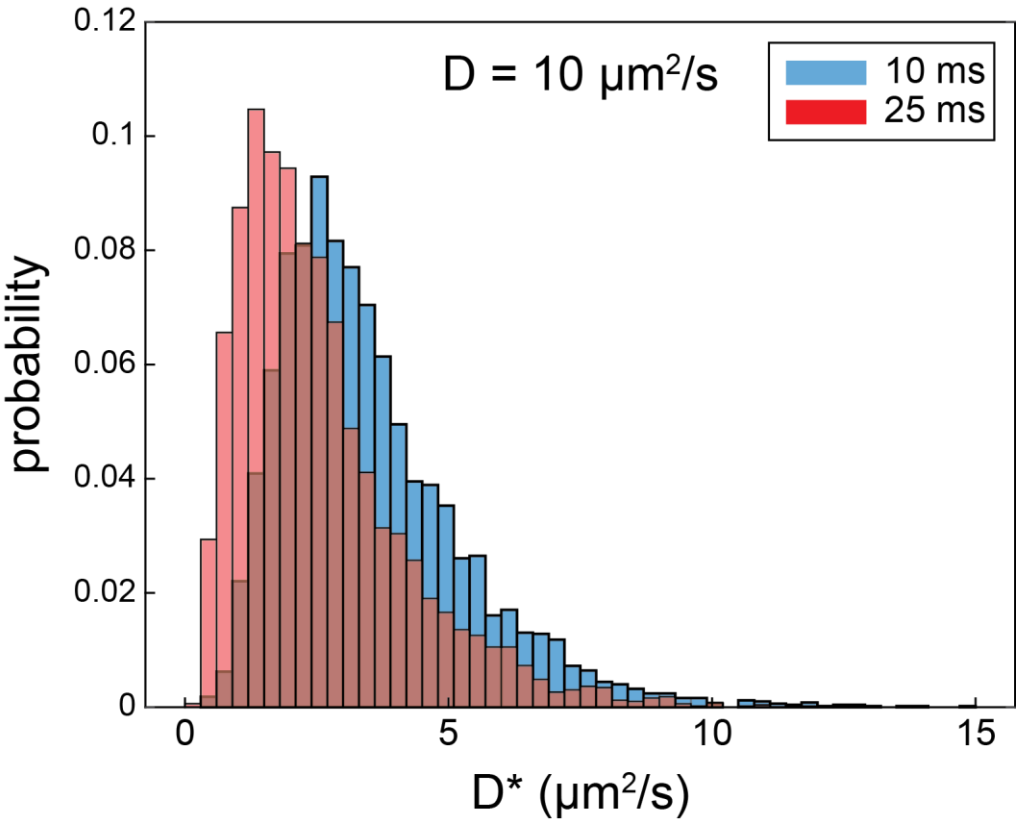

Figure 3.5. Overlay of apparent diffusion coefficient distributions of simulated data. The unconfined diffusion coefficient used to simulate images is 10 $\mu m^2/s$. The distribution of 10 ms data is right-shifted compared to the distribution of 25 ms data. This finding shows that imaging with shorter exposure time is better at probing the fast motion of molecules.

To determine if consistent results can be obtained, the approach described above was applied to experimental apparent diffusion coefficient data acquired at 10 ms and 25 ms separately [Fig. 3.6]. When the exposure time is 25 ms, the distribution is fit well using a single diffusive state with D = 15.0 $\mu m^2/s$, which is consistent with previous work [111]. When the exposure time is 10 ms, the distribution is fit well with a single state of D = 14.5 $\mu m^2/s$. There is a small (6% or less) stationary ($D < 0.5\ \mu m^2/s$) population for both datasets, which may be due to the non-specific interaction with other cellular components. We notice that the stationary population for the 10 ms dataset is smaller than that for 25 ms dataset. We reason that the difference is due to the fact that imaging with shorter exposure time is less affected by motion blur, thus able to detect molecules with better accuracy. In spite of the small difference, the resolved unconfined diffusion coefficients are the same within error. The fact that both 25 ms and 10 ms datasets can be fit with the same single state proves that the robustness of the above protein diffusion analysis framework is independent of exposure time. The assumption of our simulation is that proteins are undergoing Brownian motion in a confined volume. Thus, we conclude that the fluorescent protein mEos3.2 is diffusing in a Brownian way in the cytoplasm of *Y. enterocolitica* cells. This property is important for the use of mEos3.2 as a nonperturbative label in *Y. enterocolitica* cells. Labeling a protein with mEos3.2 in *Y. enterocolitica* cells does not alter its diffusive behavior except that the diffusion rate is slowed due to increased molecular weight.

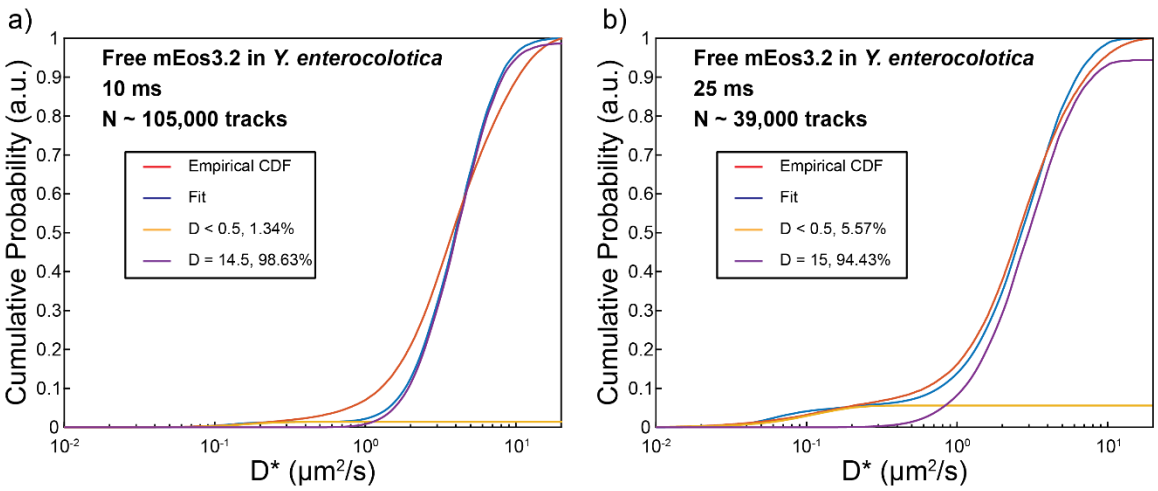

Figure 3.6. The 3D diffusion of cytosolic fluorescent protein mEos3.2 in *Y. enterocolitica* can be explained using a single diffusive state. The diffusive behavior of mEos3.2 is independent of experimental exposure time. a) the distribution acquired experimentally with an exposure time of 10 ms is fit well with a single diffusive state (D = 14.5 $\mu m^2/s$). b) the distribution acquired with an exposure time of 25 ms is fit well with a single diffusive state (D = 15.0 $\mu m^2/s$). A small fraction of population is stationary (D < 0.5 $\mu m^2/s$) in both datasets. The fraction of stationary population is smaller in the dataset of 10 ms exposure time.

3.6 Conclusions

Single molecule tracking is able to provide information about protein diffusion, thus facilitating the understanding of the cellular environment and dynamic behavior of proteins. However, a robust analysis method is needed to extract the rich information from the experimentally acquired distribution of apparent diffusion coefficients. Here, we further demonstrate the robustness of a protein diffusion analysis framework based on Monte-

Carlo simulation of confined Brownian diffusion. The framework estimates the diffusive states and their relative population fractions in confined bacterial cell volumes from camera-based trajectories. We apply the analysis to datasets collected with different exposure times, specifically, 10 ms and 25 ms, and find the fluorescent protein mEos3.2 is diffusing as a single diffusive state in *Y. enterocolitica* cells. The results indicate that mEos3.2 undergoes Brownian motion in living cells, which validates the underlying assumption of our analysis method. Moreover, we find that imaging with shorter exposure time captures the diffusing behavior of proteins with better detection efficiency due to less motion blur effect.

Chapter 4: Computational Aberration Correction

This chapter is adapted from the published paper [141].

4.1 Introduction

The accuracy and precision of localizing a single molecule in SMLM is of prime importance for they affect the subsequent data interpretation and the faithfulness of the extracted information. The accuracy, i.e., the deviation from the true position, depends largely on the choice of a model for fitting PSFs. The precision, i.e., the random statistical variability upon repeated measurements, depends primarily on the signal-to-background ratios (SBRs) of the collected PSFs. Thus, an algorithm and model which accurately represent how images are formed from light emitted by target emitter is needed to derive the true localizations of emitters. Any mismatch between model and experimental optical systems results in inaccuracy in spatial estimation. Among these contributing factors to the mismatch, optical aberrations of the system have been intensely investigated, and it is a problem we are trying to address in our SMLM.

Optical aberrations can arise from the fact that the imaging instruments are designed for samples with specific optical properties, otherwise the performance of the optical instruments is compromised. The commonly used high-NA objective lenses are oil-immersion lenses. However, biological samples are water-based, which means a refractive index mismatch exists in the light propagation. According to Huygens' principle, every point on a wave is a source of spherical wave. Due to the refractive index mismatch, however, the directions and phases of light rays from an emitter are changed so that the wavefronts are distorted instead of being spherical. Thus, the rays are not focused to the same point, which indicated the presence of spherical aberration. The effect of refractive index mismatch on light focusing has been studied by Torok *et al.* [142, 143]. In their work of careful theoretical calculation, they found that the degree of spherical aberration is

dependent on emitter depth and numerical aperture of the objective lens. Hell *et al*. reported the effect of refractive index mismatch on confocal fluorescence microscopy theoretically and experimentally [144]. In their work using a high-NA oil immersion objective lens, they found that the oil-water refractive index mismatch led to a decrease in resolution and peak intensity.

Another factor leading to aberrations is optical components, such as the lens are not perfect. To achieve an ideal, stigmatic image, which means all ray emitted from a single point will converge to the same single point, the surface of the lens must be aspheric, opposed to the spherical surfaces that is easier to manufacture in practice [145]. In reality, the center of the spherical lens is close to an ideal aspheric surface which is required to produce a stigmatic image. As the distance from the lens center increases, the surface deviates more from ideal. Therefore, light rays incident on the periphery of the lens are refracted differently from theoretical, ideal calculations. It is well established that optical aberrations become more pronounced as emitters are localized far away from the central optical axis [34, 116, 146-148]. Fig. 4.1 shows an image acquired with fluorescent beads all over the field-of-view on the home-built SMLM which is detailed in Chapter 2. When the fluorescent bead at the center is in focus and the angle of its DH-PSF is about 90º, as the distance of a bead to the center increase, the angle between two lobes of DH-PSFs deviates more from 90º.

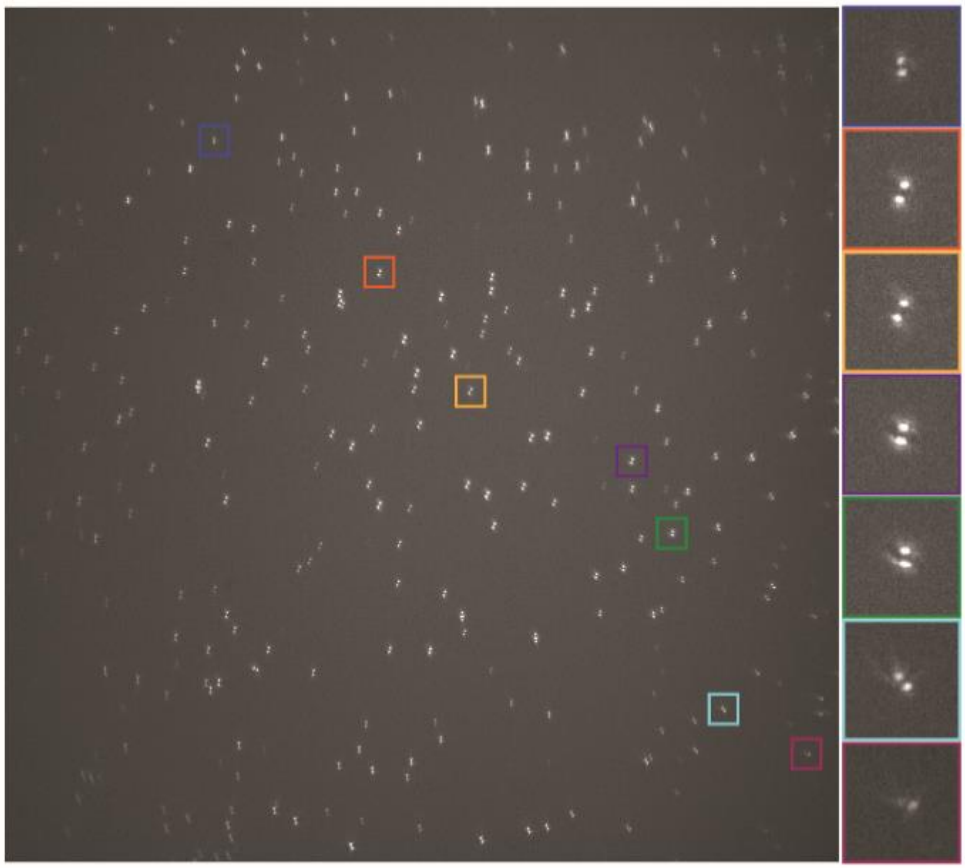

Figure 4.1. DH-PSFs of fluorescent beads depend on position relative to the central imaging axis. On the right are the magnified DH-PSFs in different colored boxes. The fluorescent beads are placed between a coverslip and agarose pad (1.5%, w/v) in PBS. The angle between the two lobes changes as the location of bead changes. For instance, the angle between two lobes of the DH-PSF in yellow box is close to 90º, while the angle of DH-PSF in red box is close to 0º. Note that the angle of DH-PSF in navy blue box is close to 90º, which may be because it is stuck in the agarose pad. Additionally, the intensity of the two lobes and the side lobe pattern change from bead to bead throughout the field-of-view.

As mentioned before, SMLM uses high-NA lenses to increase the quantity of collected photons. However, this increased NA comes at a cost of including higher order aberrations,

leading to PSFs that are further distorted [28]. Additional aberrations are introduced through imperfections in alignment of the optical components, resulting in increased degradation of image quality.

In addition to those introduced through optical components, biological samples being imaged can also introduces aberrations into the system. Biological samples are heterogeneous mixtures of different molecules, such as proteins, RNAs, DNAs, lipids etc. They may also contain different compartments, such as ER, Golgi, and nucleus as is the case in eukaryotic cells, each containing a unique environment. Molecules are not homogenously distributed in cytoplasm, and the membrane surrounding the cell has different subregions [149-151]. Thick tissues are more complex, with refractive index varying from tissue to tissue[152, 153]. When light travels through such a heterogeneous sample, the wavefront is degraded, and the image recorded on camera is distorted as a result. As the imaging depth increases, the aberrations increase as well. Fig. 4.2 shows the effect of imaging depth on DH-PSF. When the fluorescent bead is deeply embedded in the agarose, even when in focus, the intensity distribution of DH-PSF is more dispersed compared to that of a bead on the coverslip. Further, there is irregularity in the shape of the DH-PSFs when scanning in the axial dimension.

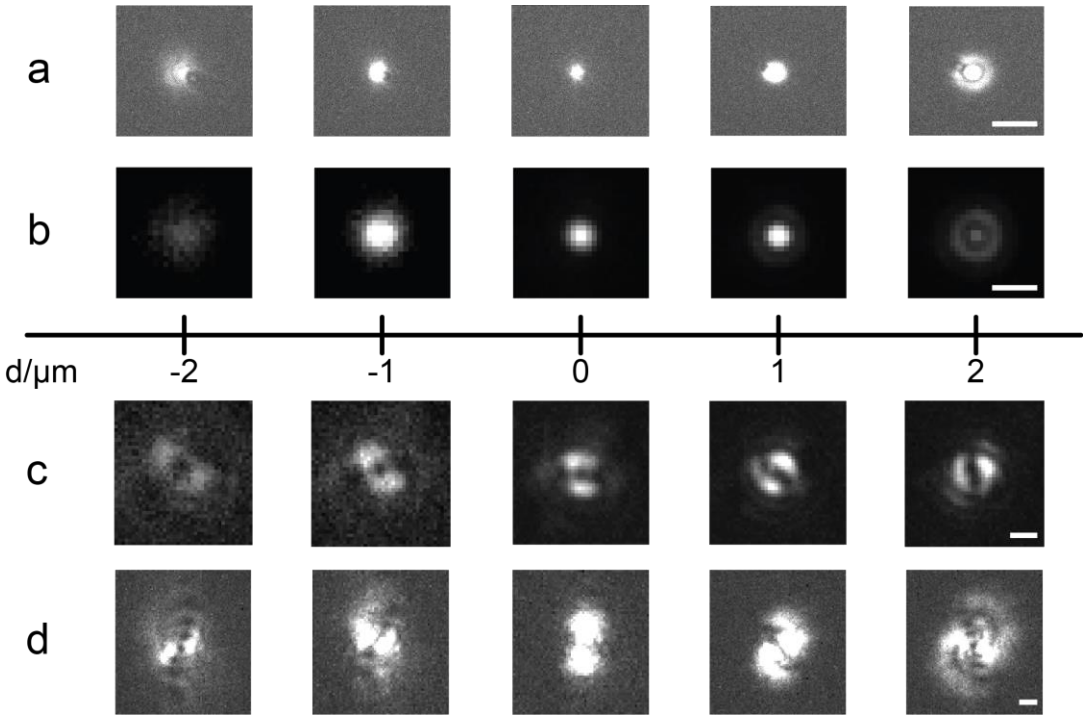

Figure 4.2. PSF change relative to imaging depth and distance to focal plane. a) regular PSF of fluorescent bead on coverslip; b) regular PSF of fluorescent bead at ~20 μm depth in agarose; c) DH-PSF of fluorescent bead at ~20 μm depth in agarose; d) DH-PSF of fluorescent bead on coverslip. The distance *d* is the relative axial position of fluorescent bead to the focal plane. The intensity in each image is scaled differently for better contrast. The regular PSF is highly symmetric around the focal plane. For both regular PSF and DH-PSF, when the imaging depth increases, the intensity and shape are affected by the depth. DH-PSF, due to its enlarged size, is more prone to be distorted by aberrations. Each row uses the same scale. Scale bar: 1 μm.

SMLM derives the localization of emitters by fitting distinct PSFs. Importantly, the accuracy of localization from blurred and distorted PSF is questionable if aberrations remain uncorrected. Correction of aberrations is imperative when a modern sCMOS camera with a large chip size is used for collecting images. The sCMOS camera provides the ability to image an ultrawide field-of-view (diameters of up to 250 μm) with fast frame

rates, thus improving the data acquisition throughout [33, 116-118]. However, the aberrations become pronounced at the periphery of such a large field-of-view. Thus, correction of spatially-variant aberrations is required when colleting SM images on an sCMOS detector.

4.2 Spatially-Variant Vectorial PSF Model

Optical aberrations are known to deteriorate image quality and impair the accuracy and precision of emitter localizations. Previous works have employed different methods to characterize and/or correct aberrations in a microscope system. Decades ago, aberration correction was performed on a confocal microscope [154]. Sheppard and Gu compensated for the spherical aberrations introduced by refractive index mismatch in confocal microscope system by altering the tube length where the objective lens is used. This aberration correction method is compatible with a high-NA objective lens and can increase the imaging depth to 150 μm in aqueous samples. However, this method is static and hard, if not impossible, to adjust to varying depths. Adaptive optics, which was first used astronomical telescopes to correct for atmospheric aberrations, is a dynamic means to measure and/or correct aberrations which change as a function of the sample, and the depth within the same sample [28]. In adaptive optics, a deformable mirror (DM) or liquid crystal spatial light modulator (SLM) are most commonly used. A wavefront sensor is used to directly measure the phase profile of the wavefront but it further complicates the instrumentation. Sherman et al. used a deformable mirror to adaptively correct depth-induced aberrations in multiphoton scanning microscopy [155]. In their work, without inserting a wavefront sensor to directly measure aberrations, they used a genetic algorithm

to help determine the optimal shape of the DM and were able to maximize the signal from the sample. Phase retrieval algorithm, which calculates the wavefront phase from images with high resolution, facilitated the correction of microscope system aberrations of a wide-field microscope [156-158]. By imaging fluorescent beads and deriving the phase of the wavefront using the phase retrieval technique, Kner et al. were able to set a deformable mirror to correct aberrations, thus improving the PSFs from a three-dimensional wide-field microscope.

Since these initial implementations, adaptive optics methods have been applied to SMLM [115, 159, 160]. Izeddin *et al.* used a deformable mirror to correct aberrations, which allows the restoring of ideal PSF shape [115]. Burke *et al.* demonstrated the use of adaptive optics in two-dimensional and three-dimensional STORM imaging to correct complex specimen-induced aberrations up to a few micrometers in the specimen [159]. Mlodzianoski *et al.* extended the imaging depth to up to 170 μm in thick samples by combining adaptive optics and active PSF shaping[160].

Adaptive optics are powerful in that they can correct for aberration by adding another optical component to the system. In some cases, simply characterizing the aberrations is beneficial because the aberrations can be accounted for in data processing. Through direct measurement of 3D PSFs and computationally extracting the wavefront phase at the back focal plane of objective lens, i.e., the pupil function, and adding other aberrations, McGorty *et al.* were able to calculate rather realistic PSFs at given depths [161]. Other researchers have used piecewise polynomial functions to interpolate experimentally-acquired PSFs [29, 162-164]. Such interpolated model functions contain larger numbers of adjustable parameters, which makes them more flexible to approximate the PSF intensity profiles.

There are models based on scalar or vectorial diffraction theory, explicitly accounting for the propagation of light through high numerical aperture imaging systems [32, 165, 166]. For instance, Petrov et al. employed a scalar diffraction theory and phase retrieval to extract the pupil function and existing aberrations in the microscope system [32]. Augmented vectorial models also include the glass-water refractive index boundary at the microscope coverslip to enable estimation of PSF shapes for emitters located within a refractive index mismatched medium [30, 167]. These models help improve the accuracy and resolution of localization in a small field-of-view. However, few of these abovementioned interpolated or diffraction-theory-based models have addressed the spatial variance of experimental PSFs in SMLM. von Diezmann et al. addressed aberrations' dependence on emitter's position in the field-of-view by experimentally generating finely sampled local calibration curves with a nanohole array filled with fluorescent dyes [34].

Here, in the work presented in this dissertation, a refined vectorial PSF model is described which uses computational phase retrieval to quantify the spatially-variant optical aberrations in two different color channels of a single-molecule localization microscope. Briefly, the pupil function is extracted from experimental DH-PSFs and the aberrations are characterized by decomposing them into eleven Zernike polynomials. i.e., 4-15 in Noll indices [168]. Then the amount of aberrations is accounted for when localizing emitters. I will detail this in follow sections.

4.2.1 Vectorial PSF Model

Previously, a vectorial model of light propagation in a refractive index mismatched medium were reported [30, 167]. We apply this model to simulate PSFs and compare the

simulated PSFs with experimental PSFs from fluorescent beads at different locations in an ultra-wide field-of-view. The simulation will be detailed here in this section and how to acquire experimental PSFs will be described in Section 4.2.2.

In our imaging system, a dipole emitter emits polarized light which propagates through the refractive index boundary, specifically, from water to glass and then oil. At the interface between these two media, light is refracted [Fig. 4.3]. The refracted light waves are then collected by a high-NA objective lens. The light waves are then further propagated through the imaging system (one tube lens and two 4f lenses with a phase mask in between, the same microscope system described in Chapter 2) using Fourier optics to ultimately yield the final intensity profile in the image plane.

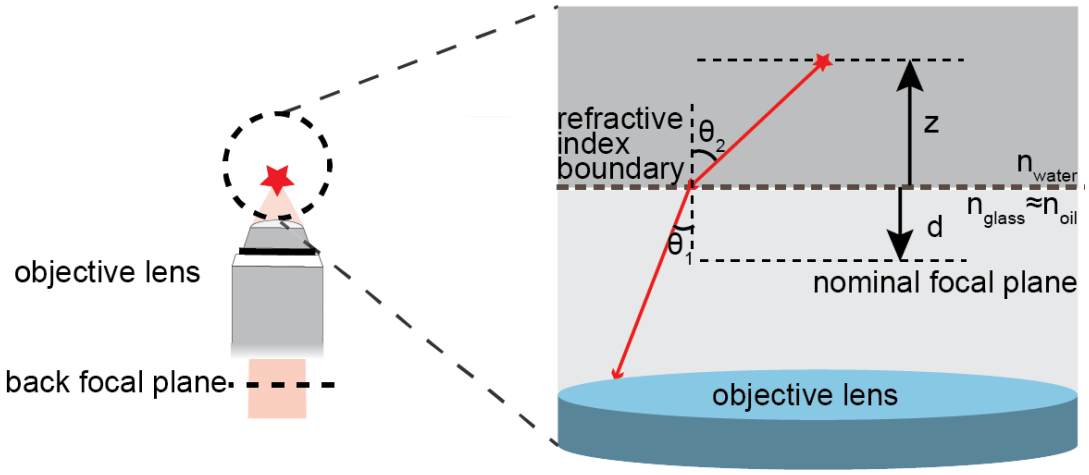

Figure 4.3. Enlarged visualization of the refractive index mismatch interface between water and glass coverslip. The figure shows the distance *d* of nominal focal plane relative to the refractive index boundary, as well as the emitter depth *z* in the refractive index mismatched medium. The nominal focal plane is equal to the focal plane in absence of a refractive index boundary. Positive values of *d* place the nominal focal plane below the refractive index boundary, whereas a negative distance *d* places the nominal focal plane into the refractive index mismatched medium. Emitter depths are parameterized by positive values of *z*, i.e. they are

always localized above the refractive index boundary. The back focal plane of the objective lens is shown. For simplicity, the rest of the emission pathway is omitted here.

At the back focal plane (BFP) of the objective lens, the phases and amplitudes of light waves, which are the pupil function, contain aberration-related information of the optical system. This vectorial PSF model is able to provide the phases that are dependent on the position of the emitter. Amplitudes are not dependent on the arbitrary position of the emitter. The mathematical details of the model are described in the following.

The refraction and transmission of the emitted light at the refractive index boundary is described, respectively, by Snell's law, $n_1 \sin\theta_1 = n_2 \sin\theta_2$, and the Fresnel coefficients. The Fresnel coefficients for transmission of *s*- and *p*-polarized light are given by

$$T_s = 1 + \frac{n_2 \cos\theta_2 - n_1 \cos\theta_1}{n_2 \cos\theta_2 + n_1 \cos\theta_1} = \frac{2 n_2 \cos\theta_2}{n_2 \cos\theta_2 + n_1 \cos\theta_1} \tag{4.1}$$

$$T_p = (1 + \frac{n_2 \sec\theta_2 - n_1 \sec\theta_1}{n_2 \sec\theta_2 + n_1 \sec\theta_1})(\frac{\cos\theta_2}{\cos\theta_1}) = \frac{2 n_2 \cos\theta_2}{n_2 \cos\theta_1 + n_1 \cos\theta_2} \tag{4.2}$$

where $n_1 = n_{glass} \approx n_{oil} = 1.52$, $n_2 = n_{water} = 1.33$ in our case. The variables θ and ϕ correspond to the polar and azimuthal angles of emitted light rays. The polar angle θ maps to the BFP polar coordinate ρ through $\rho = \sin\theta_1 = n_2 \sin\theta_2 / n_1$, whereas the azimuthal angle ϕ maps one-to-one to the BFP azimuthal coordinate. The numerical aperture of the objective lens defines the range of angle θ_1 that can be collected and thus the maximum radius ρ_{max} in the BFP according to

$$\rho_{\max} = \frac{NA}{n_1} \tag{4.3}$$

The emitter's dipole orientation can be defined in both Cartesian and spherical coordinates according to

$$\vec{\mu} = \begin{bmatrix} \mu_x \\ \mu_y \\ \mu_z \end{bmatrix} = \begin{bmatrix} \sin\Theta\cos\Phi \\ \sin\Theta\sin\Phi \\ \cos\Theta \end{bmatrix} \tag{4.4}$$

Then the electric field amplitudes of *x*- and *y*- polarized light, E_x^A and E_y^A, are calculated using Eqns. 4.5 and 4.6, respectively.

$$E_x^A = \begin{bmatrix} \left(\frac{n_1}{n_2}\right)\cdot\left(\left(\frac{\cos\theta_1}{\cos\theta_2}\right)T_s\sin^2\phi + T_p\cos^2\phi\sqrt{1-\rho^2}\right) \\ -\frac{\sin 2\phi\cdot\left(\frac{n_1}{n_2}\right)\cdot\left(\left(\frac{\cos\theta_1}{\cos\theta_2}\right)T_S - T_p\sqrt{1-\rho^2}\right)}{2} \\ -\left(\frac{n_1}{n_2}\right)^2\left(\frac{\cos\theta_1}{\cos\theta_2}\right)T_P\rho\cos\phi \end{bmatrix}^T \cdot \begin{bmatrix} \mu_x \\ \mu_y \\ \mu_z \end{bmatrix} \tag{4.5}$$

and

$$E_y^A = \begin{bmatrix} -\frac{\sin 2\phi\cdot\left(\frac{n_1}{n_2}\right)\cdot\left(\left(\frac{\cos\theta_1}{\cos\theta_2}\right)T_s - T_p\sqrt{1-\rho^2}\right)}{2} \\ \left(\frac{n_1}{n_2}\right)\cdot\left(T_P\sin^2\phi\sqrt{1-\rho^2} + \left(\frac{\cos\theta_1}{\cos\theta_2}\right)T_s\cos^2\phi\right) \\ -\left(\frac{n_1}{n_2}\right)^2\left(\frac{\cos\theta_1}{\cos\theta_2}\right)T_P\rho\sin\phi \end{bmatrix}^T \cdot \begin{bmatrix} \mu_x \\ \mu_y \\ \mu_z \end{bmatrix} \tag{4.6}$$

The phases of the electric field in the Fourier plane (FP) (the location of the phase mask between the two 4f lenses) depend on several factors, namely the *z*-position of the emitter above the refractive index boundary [30]

$$\psi_{depth} = \frac{2\pi n_2 z}{\lambda}\sqrt{1-\left(\frac{n_1}{n_2}\rho\right)^2} \tag{4.7}$$

and the distance *d* between the nominal focal plane and the refractive index boundary (modified from [32])

$$\psi_d = \begin{cases} \frac{2\pi n_1 d}{\lambda}\sqrt{1-\rho^2}, d > 0 \\ \frac{2\pi n_2 d}{\lambda}\sqrt{1-\rho^2}, d < 0 \end{cases} \tag{4.8}$$

and the lateral *x*,*y*-displacement of the emitter from the central optical axis (modified from [32])

$$\psi_{lateral} = \frac{2\pi \cdot NA \cdot M}{\lambda\sqrt{M^2 - NA^2}} \cdot \rho(x\cos\phi + y\sin\phi) \tag{4.9}$$

where in these expressions λ is the emission wavelength and *M* is the magnification of the imaging system.

The overall phase in the FP is thus given by

$$\psi = \psi_{depth} + \psi_d + \psi_{lateral} \tag{4.10}$$

and the complex amplitudes in the FP are then given by

$$E_x^{FP} = E_x{}^A e^{i\psi} \tag{4.11}$$

and

$$E_y^{FP} = E_y{}^A e^{i\psi} \tag{4.12}$$

To compute the PSF in the image plane, we propagate the light wave through the rest of the imaging system using Fourier optics

$$PSF = \left| \hat{F}\left\{ P(u,v) \cdot E_x^{FP} \right\} \right|^2 + \left| \hat{F}\left\{ P(u,v) \cdot E_y^{FP} \right\} \right|^2 \tag{4.13}$$

where *P(u,v)* is the phase mask, which, in our case, alters the standard PSF to the DHPSF, and is known *a priori*.

The model described so far produces DH-PSFs assuming no optical aberrations. To account for optical aberrations, Eqn. 4.13 is modified to

$$PSF = \left| \hat{F}\left\{ e^{iW(x,y;\rho,\phi)} P(u,v) \cdot E_x^{FP} \right\} \right|^2 + \left| \hat{F}\left\{ e^{iW(x,y;\rho,\phi)} P(u,v) \cdot E_y^{FP} \right\} \right|^2 \tag{4.14}$$

where $W(x,y;\rho,\phi)$ is the wavefront aberration phase which depends on both the emitter's position and BFP/FP coordinates, described by a summation of a set of Zernike polynomials

$$W(x,y;\rho,\phi) = \sum_{j=4}^{15} a_j(x,y) \cdot Z_j(\rho,\phi) \tag{4.15}$$

For each Noll index (*j*), $a_j(x,y)$ is the spatially-variant aberration coefficient, and Z_j is the Zernike polynomial normalized to π. Each Zernike polynomial represents a kind of aberration. For example, when the Noll index j = 11, the corresponding Zernike polynomial is the primary spherical aberration. Notably, Zernike polynomials are orthogonal over a circular pupil, thus only one set of a_j will be determined.

In the vectorial PSF model, we assume that the fluorescence emission from each emitter is isotropic. To model the PSF of an isotropic emitter, the PSFs of three specific dipole orientations are summed in the image plane [30, 169]. Specifically, the three anisotropic emission dipoles have orientations with angle Φ and Θ of (0, π/2), (π/2, π/2), and (π/2, 0) (See Eqn. 4.4). In practice, we use fluorescent beads of 100 nm diameter to acquire experimental PSFs. To account for the finite spherical volume of these beads, a Gaussian

blur with a radius of 0.58 pixels (62.6 nm) is added to the simulated image. This blur radius is determined by minimizing the difference between a simulated 100 nm sphere filled with isotropic emitters and a simulated blurred isotropic point emitter in the absence of noise and aberration.

4.2.2 Experimental Procedure

For the initial phase mask alignment and aberration characterization, the sample is the same as a standard calibration sample, which places fluorescent beads on the coverslip. Briefly, 100 nm tetraspeck fluorospheres (Invitrogen) are diluted in PBS at a ratio of 1:3000 (v/v) and then spin-coated onto a microscope coverslip (Schott, Nexterion® Coverslip Glass D). To maintain a refractive index similar to water, we cover the beads with a 1.5% (w/v) low-melting point agarose (Fisher Scientific) pad made with PBS buffer to mimic experimental conditions used for live cell imaging [14, 136, 170]. With the sample mounted on the stage, we scan the nominal focal plane of the objective lens through the fluorescent beads with equally-sized steps (50 nm) along an axial range of 3 μm. At each focal plane position, ten frames are collected with an exposure time of 30 ms.

The alignment of the phase mask must be well aligned in each experiment to avoid further complicating the system. In practice, we acquire the images of a centermost fluorescent bead in the field-of-view, which is considered to be the least aberrated. Easy-DHPSF software [171] is used and we ensure that the intensities of DH-PSF's two lobes are even and that the lateral shift of the fitted positions at different nominal focal plane positions, i.e. the wobble effect [172], is minimal.

Calibration images to determine the spatially-variant aberration profiles are acquired by scanning the nominal focal plane through fields-of-view containing many immobilized fluorescent beads along the *z*-axis. The size of these fields-of-view is more than 150-by-150 μm^2.

To generate a sample containing fluorescent beads immobilized at different depths in the agarose and beads on coverslip simultaneously, we first spin-coat the coverslip with fluorescent beads as described earlier in this section, then spot a 10 µL mixture of fluorescent beads suspended in molten 1.5% agarose on top of the coverslip.

The same field-of-view is imaged in two color channels. All images were acquired with an exposure time of 30 ms and illumination intensities of 3-50 W/cm^2 on the sample.

4.2.3 Data Processing

As described in Section 4.2.2, we scan over the fluorescent beads back and forth across an axial range of 3 µm with a step size of 50 nm, collecting 10 frames at each nominal focal plane position. In data processing, 10 frames from each position are averaged. This produces a set of 120 averaged images, each with different distance between fluorescent beads and the nominal focal plane.

As shown in Fig. 4.1, the rotation angle of DH-PSFs changes across the field-of-view. The optical axis is an important reference for it is the least aberrated pathway a light ray can travel. To determine the optical axis, we fit a 2-dimensional Gaussian function to the rotation angles of DH-PSFs in each image and define the apex as the optical axis.

We adjust the lateral position of phase mask prior to each experiment. However, it is still reasonable to suspect that phase mask can be misaligned to a degree that cannot be

detect by using only Easy-DHPSF software. We use the bead closest to the optical axis determined as earlier described to determine the nominal focal plane position *d* [as shown in Fig. 4.3] relative to the refractive index boundary in each image, as well as the phase mask's rotation and lateral displacement from the optical axis. The fluorescent bead closest to the optical axis is assumed to be least aberrated. Maximum Likelihood Estimation [89] is used to minimize the difference between its experimental PSFs and simulated aberration-free PSFs using our vectorial PSF model. To estimate the position of the nominal focal plane relative to the refractive index boundary, the *z*-position relative to the refractive index boundary of the bead was assumed to be 50 nm (the diameter of the beads in our calibration measurements is 100 ± 6 nm, according to the manufacturer). The *x*- and *y*-postion of the abovementioned bead are fitting parameters in this step. In one experiment, nine fields-of-view were collected and after this step, the mean and standard deviation of position and orientation parameters were: x-shift: 47.0180 +/- 5.6662 μm, y-shift: 45.5806 +/- 8.7760 μm, rotation angle: 97.5443 +/- 0.8857 degrees. The diameter of phase mask pixel is 3.733 mm, which is three orders higher than the standard deviation of the lateral estimation. After the phase mask's parameters and nominal focal plane positions are determined, they are not changed anymore in following data processing.

In our model, we consider Zernike polynomials in Noll indices $j = 2,\ldots,15$. To quantify the amount of the aberrations these polynomials represent, the coefficients $a_j(x,y)$ are estimated at all bead locations as previously reported [Fig. 4.4 (a)] [32, 166]. Briefly, this is done by minimizing the difference between experimental PSFs and simulated PSFs based vectorial model using MLE. For each experiment, we pool all bead locations and corresponding coefficients together to resolve final coefficient maps. We do not include

the coefficients for Zernike polynomials with Noll indices 2 and 3, for that they correspond to tip and tilt, which do not change the shape of the PSF.

To estimate the Zernike coefficients $a_j(x,y)$ with $j = 4,\ldots,15$ at any location in the field-of-view, for each Zernike mode, we fit a two-dimensional polynomial function of low order (usually 2-4, not to be confused with the Zernike polynomials) to the coefficients [Fig. 4.4 (b)] [173]. The residual at a certain location, defined as the vertical distance between experimentally-determined coefficient and value on the polynomial surface, is checked to keep a mean that is close to zero [Fig. 4.4 (c)]. Moreover, we make sure that any spatial dependence of residuals is eliminated by increasing the order of polynomial surfaces, if necessary [Fig. 4.4 (d)]. Specifically, the final orders are: 2 for j = 4-6, 3 for j = 7-10 and 4 for j = 11-15.

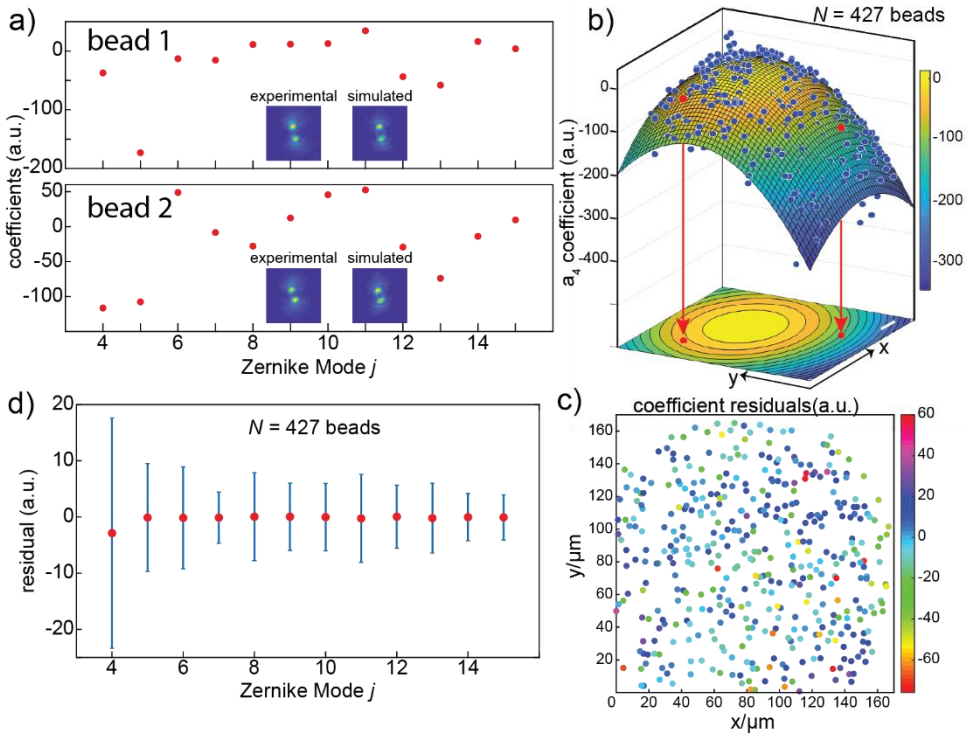

Fig. 4.4. Spatially-variant Zernike coefficients. a) Coefficients for Zernike polynomials j = 4,…, 15 at two different bead positions in the field-of-view (indicated by red arrows and the red dots in panel b). Insets: experimentally

measured DHPSFs (left) and simulated DHPSFs (right) based on the estimated Zernike coefficients. b) Spatial variation of Zernike coefficients a_4 (defocus). The amount of defocus aberration was estimated at N = 427 bead positions (blue dots and red dots) pooled from three separately acquired fields-of-view. The surface is a second-order polynomial fit to the experimentally determined defocus coefficients. The corresponding contour map is also shown. Scale bar: 20 μm. c) The coefficient residuals, defined as the vertical difference between the blue dots and the polynomial surface. No spatial dependence is evident. d) Mean (red circles) and standard deviation (error bars) of coefficient residuals for all Zernike modes considered.

When estimating the coefficients from all fluorescent beads, we notice that the coefficients of some beads are lying at a distance more than three standard deviations of residuals from the polynomial surfaces. This can result from the wiggling of fluorescent beads, fluorescent beads embedded in the agarose pad, overlapping DH-PSFs or intensity bleeding from neighboring beads. These beads are iteratively removed from surface fits until all remaining beads fall within three standard deviations range. Such beads are removed from surface fits of all other Zernike polynomial as well. We also notice that outliers are evenly distributed throughout the field-of-view, ruling out possible spatial dependence.

The final polynomial surfaces can then each be queried at any location of the field-of-view to obtain the local aberration coefficients. The combined aberration coefficients provide the overall spatially-dependent wavefront aberration phase $W(x, y; \rho, \phi)$, which allows us to compute spatially-variant aberrated PSFs.

As stated before, we combined estimations from multiple fields-of-view. To verify the accuracy of the polynomial fits, we performed cross-validation. First, we randomly remove one subset of fluorescent beads from one acquired fields-of-view. Then, the same polynomial fits are performed to the rest of the acquired fields-of-view. The differences between surfaces created from all and subset of fields-of-view are not significant, i.e., they are within one standard deviations of the distribution of residuals [Fig. 4.5 (a)].

In practice, we have an illumination intensity of Gaussian profile which leads to the signal-to-background ratio uneven across the field-of-view. Specifically, the SBR is high at the center and low at the periphery of the field-of-view. And we notice that the coefficient map of defocus, of which Noll index is 4, is close to Gaussian profile [Fig. 4.4 (b)]. To rule out the possibility that coefficient estimation is dependent on the illumination intensity profile, we lower the illumination intensity and image the same fields-of-view. The difference between the obtained coefficient maps is within errors [Fig. 4.5 (b)].

As stated previously, we assume the position of fluorescent beads to be 50 nm, because of the 100 nm diameter. The effect of heterogeneity of bead size on coefficient estimation should be considered, for that z-position of emitter directly affects the phase at BFP and then collected images. We first simulate aberrated images of beads at z-position of either 20 nm or 80 nm, using spatially-dependent aberration profiles determined with bead z-position of 50 nm, as demonstrated before. The aberration coefficients are then estimated by assuming the z-position of 50 nm. The difference of estimated coefficients relative to the ground truth is within one standard deviation of the coefficient residuals for every considered aberration except for defocus (j = 4) [Fig. 4.5 (c)]. And we notice that the difference of coefficients for primary spherical aberration (j = 11) is second largest. This

is not surprising because the defocus (j = 4) and primary spherical (j = 11) aberrations are strongly coupled with the distance d and emitter z-position. However, these simulations overestimate the bead size variation, which is 6 nm in diameter for the unstained microspheres according to manufacturer. When we repeat the same simulations with 6 nm depth variations, all Zernike coefficient differences were withing one standard deviation of the coefficient residuals.

We also investigate to what extent the precision of coefficient estimation of each Zernike mode limits the 3D localization accuracy. For a certain Zernike mode, we simulate aberrated images with coefficient that is computationally shifted one standard deviation of the residuals away from the original value while the coefficients of other Zernike modes remain unchanged. The aberrated DH-PSFs are used to localize emitters and the deviation, defined as the differences between localized positions and the ground truth, is less than 5 nm at x,y-dimensions in all cases. The deviation in the z-dimension was less than 10 nanometers except for defocus (j = 4) or primary spherical aberration (j = 11) [Fig. 4.5 (d)]. Again, the larger deviations for defocus and primary spherical aberrations can be attributed to their strong coupling with an emitter's axial position.

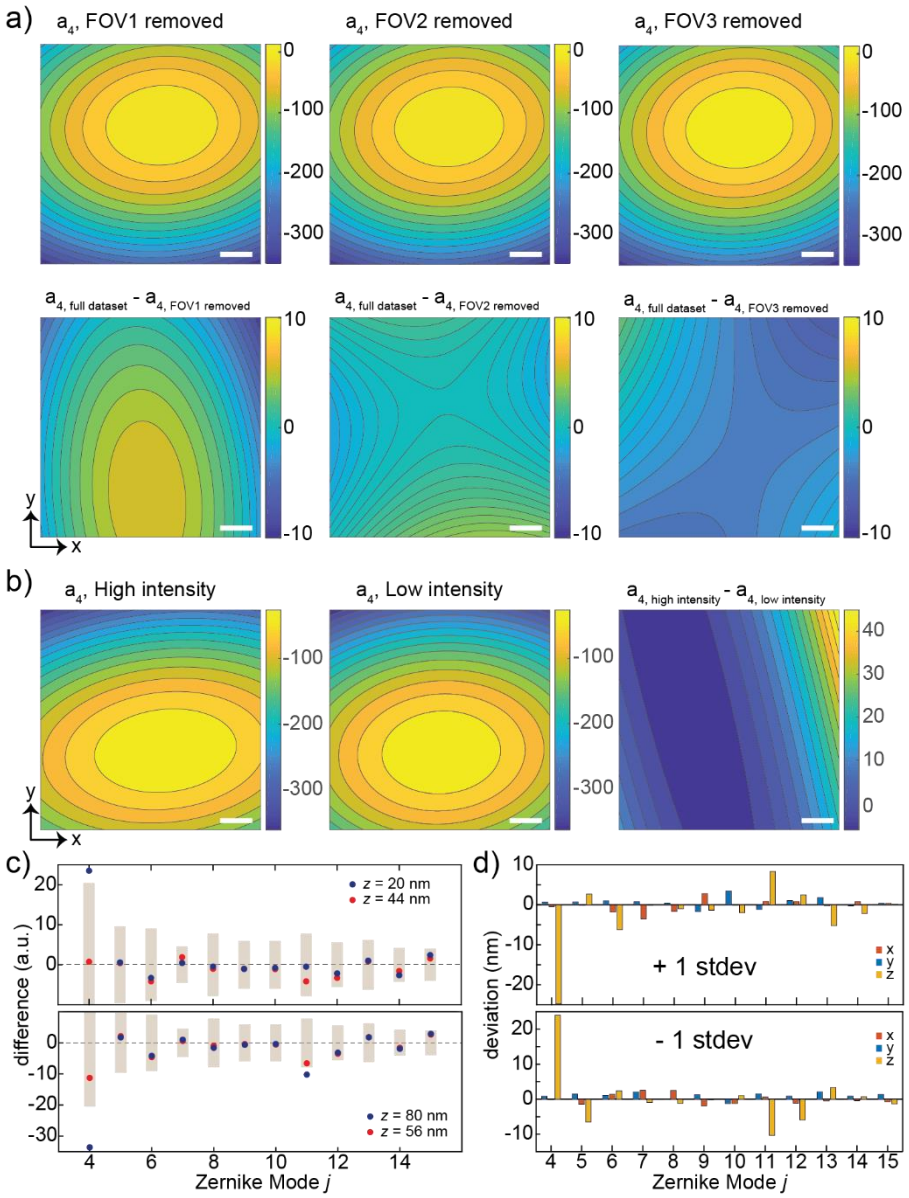

Fig. 4.5. a) Cross-validation of polynomial surface fitting. The first row shows contour surfaces of the defocus aberration coefficient a_4 obtained after removing the beads acquired in one of three fields-of-view. The second row shows the difference contours relative to the full dataset contour map shown in Fig. 4.4 (b). Scale bars: 20 μm. b) Defocus aberration coefficient a_4 contours in the other (green) channel of our microscope acquired using different laser intensities. The peak intensities are 23.5 W/cm^2 amd 4 W/cm^2 for high and low illumination intensity, respectively. The size of the excitation spot was 320 μm (1/e^2 radius) in both cases. For this dataset, the standard deviation of a_4 residuals was 57 a.u.. Scale bars: 20

μm. c) Effect of bead size on aberration coefficient estimation at a single position in the field-of-view. The difference between estimated and true coefficients are shown for different bead sizes (blue and red circles). Gray bars represent ± one standard deviation of the experimentally-determined coefficient residuals [Fig. 4.4(d)] centered at zero. Among the Zernike modes considered here, only the defocus (j = 4) and primary spherical aberration (j = 11) exhibit strong coupling with emitter z-position. d) Effect of coefficient estimation on localization accuracy. Zernike coefficients were changed one at a time by the amount of one standard deviation of the corresponding residuals and the resulting DHPSFs were analyzed using the original coefficients.

Based on these experimental and simulated measurements, we conclude that polynomial surface fitting is robust. We can accurately estimate the spatially-variant aberration coefficient profiles through a large field-of-view by assuming bead z-position of 50 nm, removing outliers and performing surface fitting of a certain order.

4.2.4 Coefficient Maps in Two Color Channels

As described in Chapter 2, the home-built single-molecule localization microscope has two color channels, one green channel and one red channel. They share the same optical path until the light wave incidents on the dichroic beam-splitter, which splits the photons into different color channels based on their wavelengths. The same estimation and fitting procedure are performed to both color channels. In Fig. 4.6, we compare the coefficient maps of three different kinds of aberrations. The three aberrations have very different maps, which also confirms that our estimation is not affected by the Gaussian profile of illumination intensity. Interestingly, the shapes of the corresponding surfaces between the

two color channels are qualitatively similar, differing only in overall magnitude. The reason for the similarity can be that aberrations of low order Zernike polynomials described here originate predominantly from optical components that are shared by both color channels.

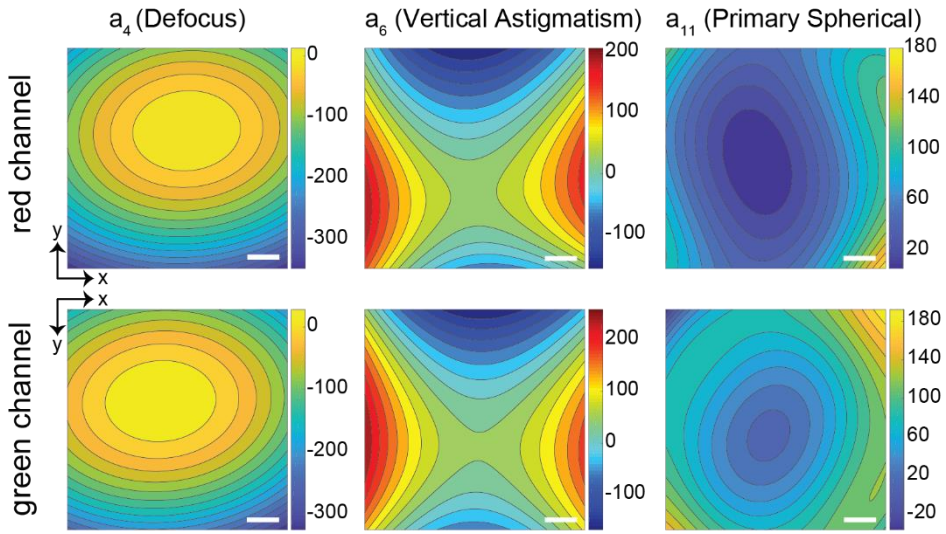

Fig. 4.6. Aberration coefficient profiles in both color channels of our microscope. Top row: Aberration coefficient contour maps for a_4 (defocus), a_6 (vertical astigmatism) and a_{11} (primary spherical aberration) in the red channel. Bottom row: Corresponding contour maps in the green color channel. Scale bars: 20 µm.

4.3 Performance of Spatially-Variant Vectorial PSF Model

In previously described sections, the vectorial PSF model is described and applied to images of fluorescent beads placed across a larger field-of-view. By minimizing the difference between simulated images and experimental images with MLE and fitting to a polynomial surface, we obtain the coefficient maps of aberrations of Zernike mode j = 4, …,15 in two color channels in a home-built single-molecule localization microscope. They provide a way to quantify local aberration amount at a certain location in the field-

of-view. We aim to facilitate more accurate and precise localization of emitters, compared with other existing models.

4.3.1 Localize Emitters Immobilized on Coverslip

As demonstrated in our model, the z-position of emitter and the position of the nominal focal plane affect the wavefront in a similar way. In other words, they are not orthogonal. And due to stage drift, the position of the nominal focal plane can change from frame to frame. Thus, the position of the nominal focal plane in every frame has to be determined prior to estimating the x,y- and z-positions of emitters that are to be localized.

The distance *d* between the refractive index boundary and nominal focal plane, as shown in Fig. 4.3, can be estimated using a reference marker with known *z*-position. In our case, a fluorescent bead immobilized on the coverslip is used. Similarly, the z position of such a reference bead is 50 nm because of its 100 nm diameter. Using the same reference marker in each frame, we then track changes in *d* over time due to stage drift [Fig. 4.7 (a)]. Knowledge of the nominal focal plane position allows us to estimate the *x*,*y*- and *z*-positions of all other beads in the field-of-view in every frame. We prepare the sample by immobilizing fluorescent beads between coverslip and agarose pad, which does not contain additional fluorescent beads so we expect a small variation in bead z-positions. However, the estimated bead depths cover a wider range (standard deviation = 68 nm, range = [2, 343] nm). The statistical localization precisions, defined as the standard deviations in the estimated *x*,*y*- and *z*-coordinates of each bead, are on the same scale of bead size variation [blue localizations in top panel of Fig. 4.7 (b) and (c)]. There exist several beads with larger

localization precision [colored in red in bottom panel of Fig. 4.7 (b) and (c)]. This is not because our method is not able to correctly localize emitters. Instead, these beads are localized at larger depths and/or show noticeable motion from frame to frame. Not considering these insufficiently immobilized beads, the averaged localization precisions at all dimensions are σ_x = 2.4 nm, σ_y = 2.9 nm, and σ_z = 3.6 nm.

The major contributor to the observed bead depth variance is the fact that some beads can get displaced into the agarose during sample preparation. A second contributing factor is the thickness variations of the glass coverslip. Microscope coverslips are not polished to optical flatness, which for high quality optics can reach λ/20~25 nm. The random thickness variations of the coverslip, which appear to be on the order of tens of nanometers, is uncorrected and its correction is beyond the scope of this dissertation.

A third contribution could come from the possibility that the aberration coefficients are not accurately estimated. To rule out this possibility, we displace the field-of-view laterally by 10 μm and estimate the depths of the same beads again [yellow localizations in top panel of Fig. 4.7 (b)]. Fig. 4.7 (b) compares the depths of the same fluorescent beads. Before and after the shift of field-of-view, the z-positions and the z-precisions are not changed considerably. The average difference between bead depths before and after lateral displacement was 0.6 nm [Fig. 4.7 (b), bottom panel]. Thus, our method is robust in estimating emitter depths accurately throughout the field-of-view.

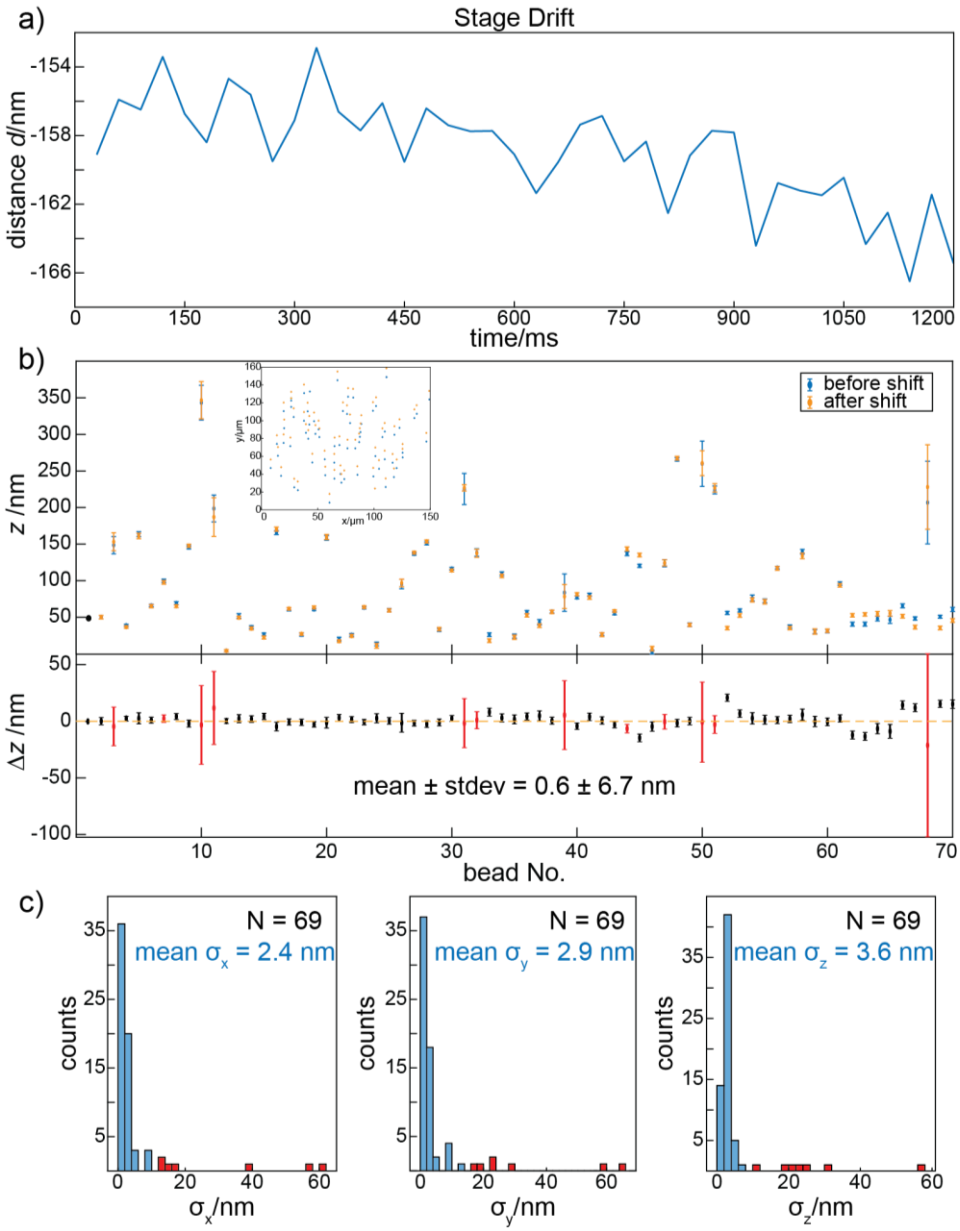

Figure 4.7. a) Change in the distance *d* due to stage drift. The same bead was used as a constant *z*-position reference. b) top panel: *z*-position measurements for different fluorescent beads on a flat coverslip immobilized by agarose before (blue) and after (yellow) a 10 μm lateral shift. The first bead (black) is the reference bead fixed at $z = 50$ nm. The red dots represent mean values from 40 measurement and the error bars represent the standard deviations. Inset: the spatial distribution of localized beads before and after the lateral shift. Bottom panel: the difference between *z*-position measurements before and after the lateral shift. Beads with

noticeable motion from frame to frame in *x*,*y*- and/or *z*-directions are colored red. c) distribution of standard deviations of individual bead position measurement in the *x*-, *y*- and *z*-dimensions. Red colored bars represent beads with localization precisions of more than 10 nm (arbitrarily chosen threshold). The mean precision here is calculated excluding these aforementioned beads. If those beads were not excluded, the mean precision is: σ_x = 5.3 nm, σ_y = 5.7 nm, and σ_z = 5.1 nm.

4.3.2 Localize Emitters in Two Color Channels

Intermolecular interaction and their proximity have been long studied, which, if successfully resolved, provide key information about molecular behavior or molecular arrangement in the same structure. Two-color imaging provides a way to obtain such information by imaging two differently labelled molecules. However, as shown in Fig. 4.6, the amount of aberrations differs in different color channels so that the images from two color channels are distorted differentially, limiting co-localization accuracy if without any further data processing. Previous work has established the use of 3D transformation functions to correct the distortion and register two 3D super-resolution datasets acquired in different color channels [14]. In order to achieve 3D registration errors of less than 10 nm, transformation functions have to be computed based on large numbers of control points distributed throughout the 3D image volume. Such an approach leads to increased computational cost when imaging control points of similarly high density in an ultrawide field-of-view.

If the use of the spatially-variant vectorial PSF model is able to correctly calibrate the aberrations in two separate color channels, it would yield depth accuracies sufficient to justify the use of 2D transformation functions to register 3D localization data. To test this

hypothesis, fluorescent beads are embedded in agarose to create samples that contain emitters at various depths. They are imaged and localized in both color channels as described before. Briefly, the same bead immobilized on the coverslip is used as reference maker in both channels to estimate the positions of the nominal focal plane. With the nominal focal plane's z-position known, the positions of other fluorescent beads are estimated and the depths are compared [top panel of Fig. 4.8 (a), red and green dots, reference marker colored in black].

Of all 25 beads presented here, they are widely distributed across the field-of-view [Fig. 4.8 (b)]. The depths of the same beads match up well with a mean difference of 0.8 nm and a standard deviation of 23.3 nm [Fig. 4.8 (c)]. We conclude that systematic *z*-colocalization errors can be eliminated and *z*-colocalization accuracies of about 20 nm can be achieved using the spatially-variant vectorial PSF model. We also note that the differences of more than 20 nm still occur for four of the beads considered here [bottom panel of Fig. 4.8 (a) and 4.8 (c)]. This observation may result from the existence of higher-order aberrations or sample-induced aberrations that are not accounted for by our model. With the aberrations in two color channels characterized and incorporated in data processing, the same emitters can be co-localized in two different color channels with an accuracy better than 25 nm, which matches localization precisions typically achieved in live-cell SMLM. To reduce *z*-colocalization errors into sub-10 nanometer regime, a locally calibrated 3D transformation function could be employed, possibly with lower control point densities [14].

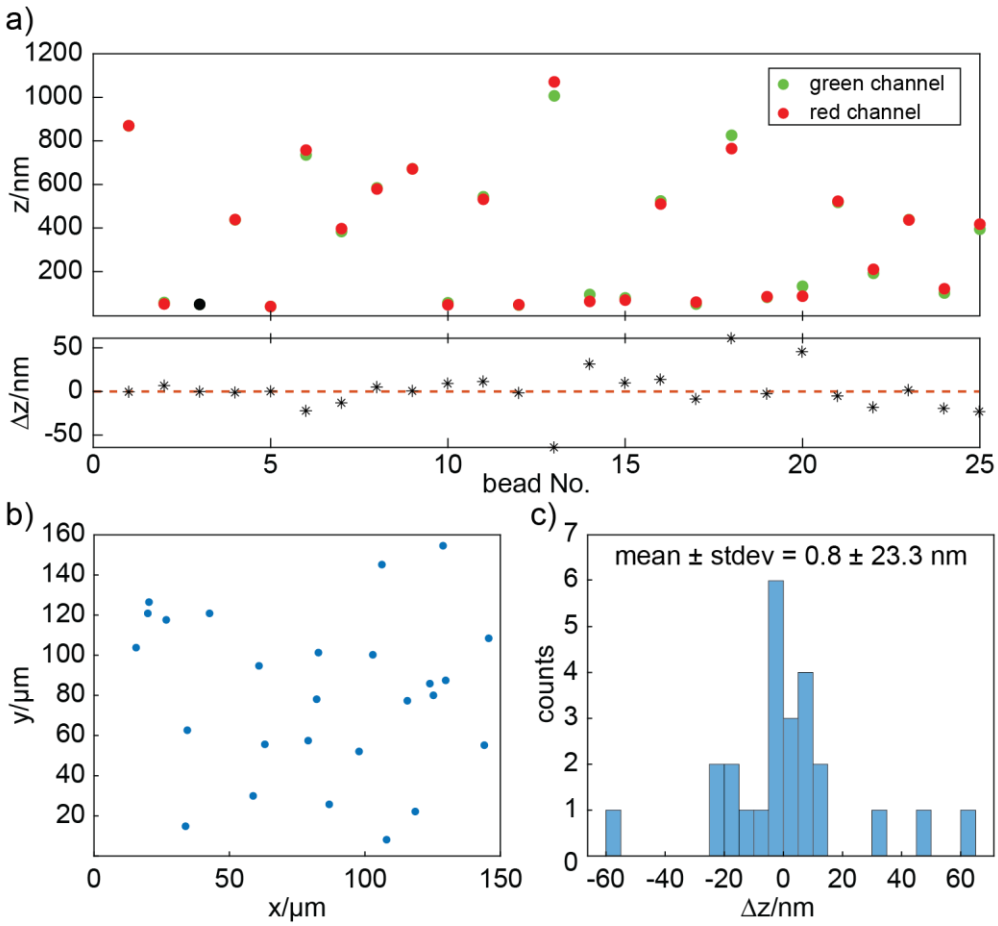

Fig. 4.8. a) Top panel: *z*-positions of the same beads as measured in two separate color channels. The bead colored in black was used as a reference marker in both channels. Bottom panel: *z*-position differences for each bead shown in the top panel. b) The distribution of localized beads in the green channel across the field-of-view. c) *z*-position differences.

4.3.3 Comparison with Double-Gaussian Model

In our microscope, by inserting a phase mask, the regular PSF is engineered into a DH-PSF. DH-PSF can be approximated as two Gaussian lobes rotating around the center. As shown in Fig.1, experimental data of fluorescent beads demonstrates the change of DH-PSFs across the field-of-view. A calibration curve or a look-up table is used to find the z-

position of an emitter based on the relative angle between its two lobes. In most cases, Easy-DHPSF algorithm[171] uses a look-up table generated at a certain location in the field-of-view globally. Due to the spatially-variant aberrations, the look-up tables from different locations are significantly different. By simulation, we can generate look-up tables of ten fluorescent beads randomly placed in the field-of-view [Fig. 4.9]. Apparently, if a global look-up table is used to interpret the z-position, the z-error can be as large as hundreds of nanometers.

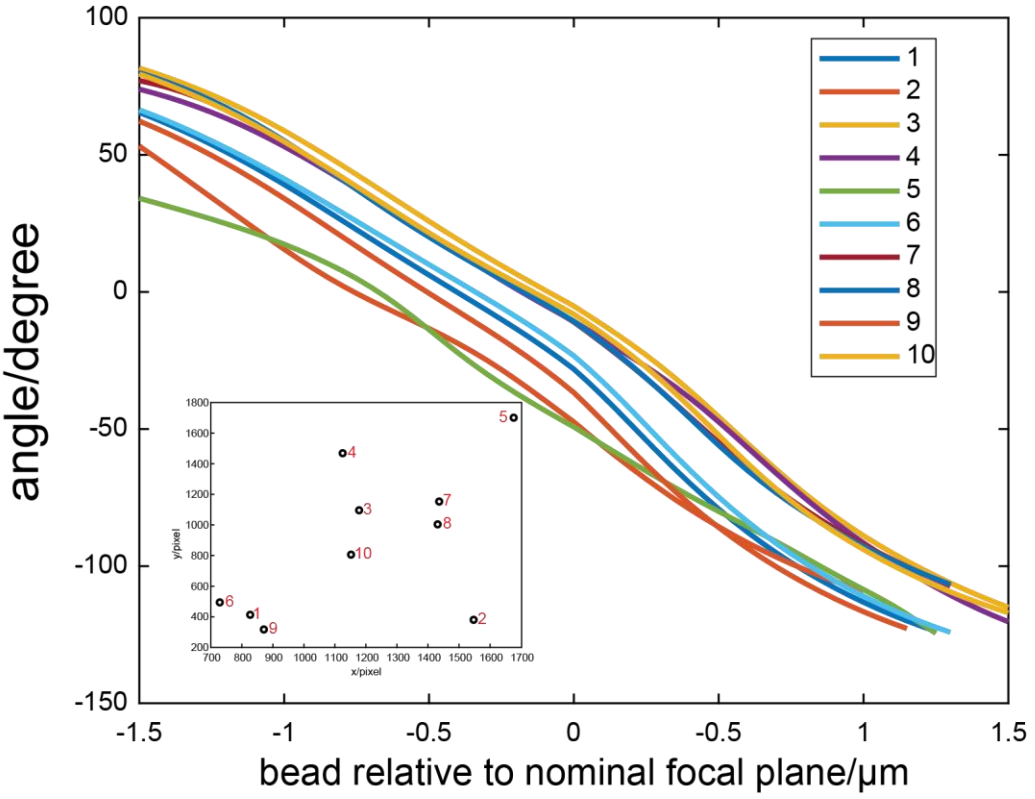

Figure 4.9. Simulated look-up tables of ten fluorescent beads in the field of view. Inset: the locations of the ten fluorescent beads. The camera size is 2048-by-2048 pixels and the pixel size is 108 nm. By simulation, the nominal focal plane is scanning through the bead below and above 1.5 μm at a step size of 50 nm. Coefficient maps described previously are used to generate realistic and aberrated images. The look-up tables are generated with Easy-DHPSF software. At a certain

angle, the inferred positions from different look-up tables can differ as large as 500 nm, for instance, between bead 1 and bead 5.

To assess the improvements in accuracy and precision of position estimates made with the spatially-variant vectorial PSF model, we compare its performance to that of the double Gaussian model used in the Easy-DHPSF algorithm. For those fluorescent beads immobilized on coverslips, Easy-DHPSF yields bead z-positions that map out a bowl shape [Fig. 4.10 (a)]. The z-positions of beads at the periphery can be up to 800 nm higher than that of beads near the center of the field-of-view. This is not surprising because the spatially-variant aberrations are not accounted for in the double-Gaussian model used in Easy-DHPSF, especially defocus (j = 4), which we have shown it affects the z-localization strongly in our simulation [Fig. 4.5 (d)]. With the aberration coefficient maps determined experimentally, we simulate images of bright fluorescent beads at the same z-depth of 50 nm above the refractive index boundary across the field-of-view. In this simulation, we make the nominal focal coincident with the boundary (d = 0). We are able to recapitulate the bowl shape if the simulated images are analyzed by Easy-DHPSF [Fig. 4.10 (b)]. It is expected because this commonly used Easy-DHPSF algorithm provides a global look-up table, leaving spatially-variant aberrations unaccounted for and uncorrected. The *z*-error, defined as the average z-positions of N = 5 individual estimates relative to the ground truth, maps out a bowl shape similar to the experimental measurement. When we refit the same data using many local look-up tables[34], the *z*-errors are reduced by roughly one order of magnitude, but they still displayed a spatial dependence [Fig. 4.10 (c)]. Note here the nominal focal plane is placed coincident with the refractive index boundary. In this

case, most of the z-errors lie within the range of [-60, 80] nm range, which is a good improvement of many local look-up tables over only a global look-up table.

We aim to test to what degree the change of the nominal focal plane, thus the change of distance between emitter positions and the nominal focal plane, will affect the z-error and its distribution. If the improvement is dependent on the relative distance, it may shed lights on how we can optimize experiments. We simulate images of fluorescent beads at z = 50 nm and the nominal focal plane at d = -500 nm, which means the they are both above the refractive index boundary into water medium. In this case, with many local look-up tables, the *z*-error range increased to [0, 200] nm [Fig. 4.10 (d)]. Importantly, in both the *d* = 0 nm and *d* = -500 nm cases, the *z*-error remained spatially-variant [Fig. 4.10 (c) and 4.10 (d)]. By comparison, the spatially-variant vectorial PSF model estimated the *z*-positions without any spatial dependence (absolute mean z-error = 1.4 nm), because the *z*-errors were determined solely by the signal-to-background-limited localization precision. If molecules inside the bacterial cell with a diameter of 1000 nm are to be studied, the distance between emitters and the nominal focal plane may vary greatly when the nominal focal plane position is fixed. We simulate the images of bright emitters displaced randomly within a range of ±500 nm relative to the nominal focal plane while maintaining the nominal focal plane at d = -500 nm. The benefit of using many local lookup tables is not as pronounced as for a constant separation distance. The *z*-error range is expanded to a larger range of [0, 300] nm and the z-errors show spatially dependence [Fig. 4.10 (e)]. Notably, the Easy-DHPSF algorithm often converges to incorrect estimates, especially when the simulated PSFs are severely aberrated. While these incorrect estimates can be filtered out during data post-processing based on reasonable criterion, such steps can reduce data acquisition

throughput which may lead to other undesired outcome, for instance, longer acquisition time and photo-toxicity.

The experiment and simulation described above are of bright emitters, which have a high signal-to-background ratio (SBR). However, a fluorescent protein is much dimmer than beads which are coated with many dyes. The signal-to-background ratio has a profound effect on the accuracy and precision of localization algorithm [27]. To evaluate and compare the accuracy and precision of different methods at different SBRs, we simulate noised images of a single emitter. The emitter is placed at z-position of 50 nm at an off-center position in the field-of-view (70 μm lateral shift), while the nominal focal plane is kept at d = 0. The background photon count is held constant at 10 photons per pixel while the signal from the emitter varies from 10^3 to 10^5 photons. For each SBR, 50 frames are simulated and analyzed to extract the x,y- and z-positions. At different SBRs, the accuracy of the double Gaussian model can be improved by using a local look-up table instead of a global look-up table, while the precision remains unchanged. For all SBRs evaluated here, the vectorial PSF model yields better accuracy and precision than the double Guassian model [Fig. 4.10 (f)].

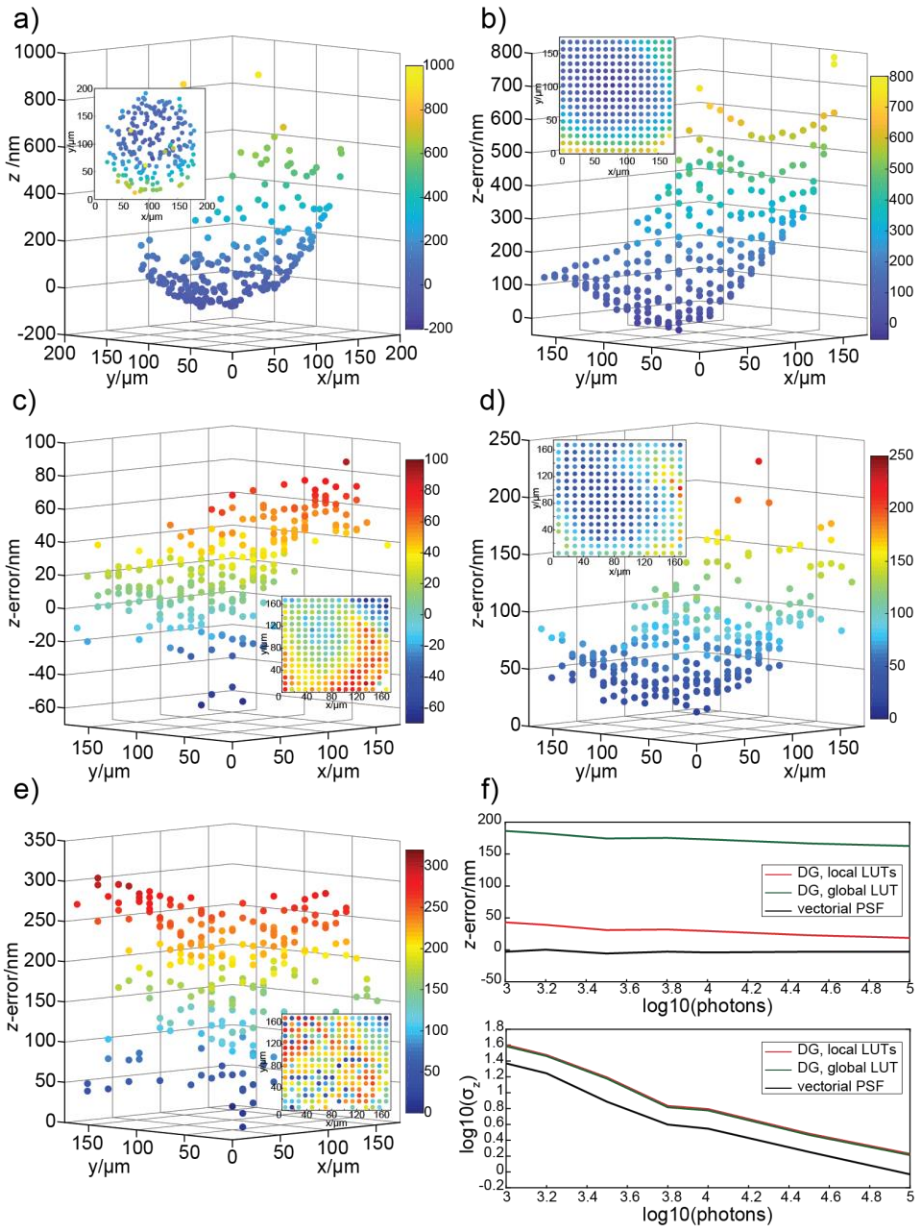

Figure 4.10. Comparison of double-Gaussian and the spatially-variant vectorial PSF model. a) *z*-positions estimates of fluorescent beads immobilized on the coverslip obtained by using the double-Gaussian PSF model and a global lookup table. Inset: Scatterplot of bead *x*, *y*-positions with each bead colored according to its *z*-position. b) Same results as in panel a, except that simulated DHPSFs of isotropic emitters were used as inputs. The *z*-error is defined as the difference between estimated *z*-positions and the ground truth (50 nm). The nominal focal plane is coincident with the refractive index boundary (d = 0 nm). Inset in panels

b-e: the projection of emitters in *x*, *y*-plane with beads colored according to their z-errors. c) The same simulation as in panel b, but processed with a double Gaussian model using many local look-up tables. d) The same simulation as in panel c, but the nominal focal plane was placed 500 nm above the refractive index boundary (*d* = -500 nm). e) The same simulation as in panel d (*d* = -500 nm, local lookup tables), but *z*-positions for DHPSF simulations were randomly chosen in the interval [0, 1000] nm. f) Accuracy and precision comparison of double Gaussian vs. spatially-variant vectorial PSF model fitting. Both analytical models perform worse than the vectorial PSF model.

4.4 Applications

As we demonstrated on experimental and simulated data, the spatially-variant vectorial PSF model enables more accurate and precise localization than commonly used double Gaussian model. However due to its heavy computation, we did not pursue its application to biological samples. Instead, we have leveraged it to optimize experimental data collection and extend the simulation to other imaging modes, specifically light-sheet microscope[174].

4.4.1 Single Molecule Imaging

Single molecule imaging and single particle tracking have revealed key information about protein diffusive behavior in its native environment in live cells, such as the diffusive states present in cells [111, 136]. We have demonstrated the better performance of our spatially-variant vectorial PSF model over the double-Gaussian model utilized in the Easy-DHPSF algorithm. However, its heavy computation cost (~2 min/localization when run on

a single core of a workstation computer) hinders the integration of the spatially-variant PSF model into data analysis if the time cost issue remains unsolved. Data processing time could be shortened by using Graphics Processing Units (GPUs), as demonstrated for interpolated PSF models [29]. We choose to leverage the power of our model by taking another direction.

In practice, stage drift is corrected by using a fiducial marker which is able to emit over the course of the data acquisition time, such as a bright fluorescent bead [175]. When the fluorescent beads are directly placed on the coverslip, and imaged cytosolic proteins are diffusing in a 1000 nm sized-bacterial cell in a Brownian way, the difference between the upmost protein z-position and fluorescent bead z-position is at the scale of ~1 μm, and the angle difference between them is close to 90º. Importantly, when the fiducial bead is in focus, the relative angle of DH-PSFs from proteins close to the upper boundary of bacterial cells is close to 0 or π. Due to aberrations, the lobes can be distorted, which further adds difficulty to correctly resolve the localizations of the emitters. YopE, an effector protein of pathogenic *Yersinia enterocolitica*, can be secreted through the type III secretion system (T3SS) into human host cells, and result in disruption of target cells [176]. Here we show the distribution of localized diffusing protein YopE, which has been truncated to its chaperone-binding domain, and fluorescently labeled with eYPF [Fig. 4.11 (a)]. When the focal plane is placed near the refractive index boundary, loss or compression of localizations at the upper half of the cell is considerable, which may result in inaccurate and incomplete analysis of molecular behavior in the cell. By simulating a circle with evenly distributed emitters and placing nominal focal plane at varied depths, we find that when the nominal focal plane is at ~400 nm, the unbiased dispersion of localizations is

recovered. Thus, it is advised that when experimentally imaging a bacterial cell, the nominal focal plane should be placed around the center of the cell instead of keeping fiduciary bead on the coverslip in focus. This produces an almost circular distribution of molecules diffusing in cytoplasm [Fig. 4.11(b)].

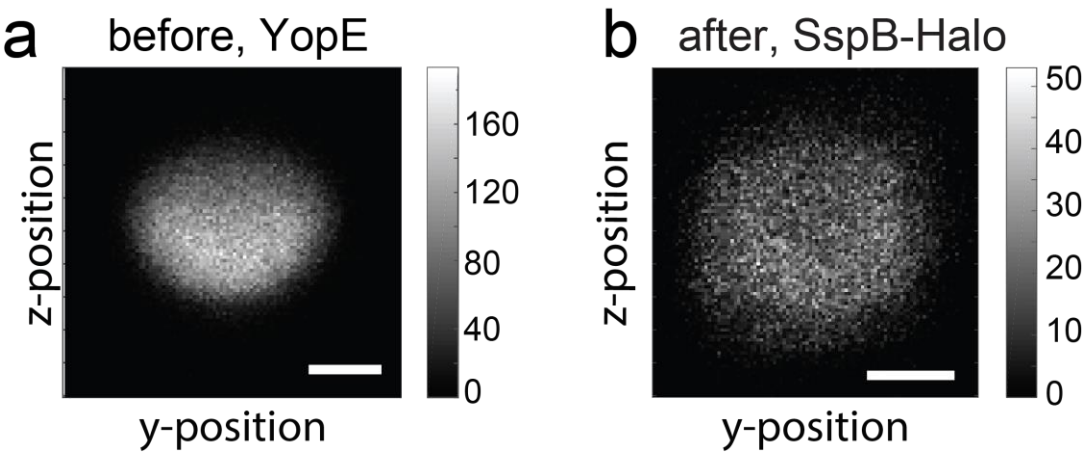

Figure. 4.11. 2D projection of molecular localizations along the cell axis. a) truncated YopE, an effector protein in pathogenic *Y. enterocolotica*, tagged with eYFP is diffusing in the cytoplasm. When imaging, fiduciary marker, in this case a brightly fluorescent bead (not shown in the figure), is placed on the coverslip. When the nominal focal plane is placed at the refractive index mismatch boundary between the coverslip and water-based bacterial, the upper half of cell suffers from a loss of localizations. Thus, the resolved localizations do not recapitulate the roundness of cells. b) After we find that placing nominal focal plane at ~400 nm above the refractive index mismatch boundary helps recover the cell shape by simulation, we experimentally validate this by imaging diffusing adaptor protein SspB [177] in *Y. enterocolitica* cytoplasm. The SspB protein is genetically tagged with the Halo-tag and stained with Janelia Fluor 549 (Promega). When imaging, the nominal focal plane is placed at ~400 nm above the mismatch boundary. The resolved z-positions of SspB-Halo recovers the roundness of cells. Scale bar: 400 nm. Colorbar: localization density, counts per 100×100 nm^2.

4.4.2 Light-Sheet Microscopy Data Simulation

In recent years, light sheet-based fluorescence imaging approached has been developed to illuminate a given selected plane within a volume, thus reducing possible photo-toxicity or photo-bleaching[108, 174]. At the same time, it provides the capability of excellent optical sectioning, rejecting unwanted background fluorescence. Light sheet microscopy is also combined with super-resolution microscopy to visualize emitters deep into samples[178, 179]. Because of its compelling performance, Zhang *et al.* used the non-invasive light sheet microscopy combined with deep convolutional neural to resolve single cells with a 3D biofilm, which is a complex community of bacterial cells[174]. This provides important information on single-cell level, such as cell size, orientation, etc. CNN-based single-cell segmentation requires training data which is computationally simulated from known ground truth. The simulated images must be representative of images in experimental conditions. Otherwise, the trained CNN cannot extract information with high accuracy if experimental data is analyzed. Therefore, it is of great importance to simulate images with a PSF model that is closest to the truth. Vectorial PSF model serves as a better approximation to the PSF under experimental conditions.

The home-built lattice light sheet microscope is equipped with two objective lenses opposed to each other [109, 174]. The biofilm sample to be studied is in a flow channel, and the scanning direction of the sample is not perpendicular to either of the objective lenses. Experimental PSF can be acquired by using a fluorescent bead and then used to simulate images. Even though such a PSF contains information of the system, such as aberrations we characterized in previous sections, it has the drawback that a fluorescent

bead is a sphere with a non-zero size. By using the vectorial PSF model, we can simulate images of cells that is close to experimental images.

4.4 Conclusions

Aberrations present in an optical system have been a haunting problem for they can significantly impair the image quality. The characterization and correction of aberrations has been intensively researched to facilitate the accuracy of information that can be extracted from images. Here we provide a quantitative frame work to characterize and correct aberrations in a two-color 3D SMLM. The use of spatially-variant PSF model is an optimal solution to localize emitters with high accuracy and precision in an ultrawide field-of-view, where aberrations can vary substantially between different locations.

Fluorescent bead images are obtained at different positions in the field-of-view and at different nominal focal plane positions. By minimizing the difference between experimental bead images and the simulated images with a vectorial diffraction model using MLE algorithm, we are able to characterize the aberrations at distinct locations in an ultra-wide field-of-view. The aberrations are quantified as linear combinations of Zernike polynomials, and the coefficients of these linear combinations represent the magnitudes of different aberrations at these locations. To facilitate the knowledge of aberrations in any location through the field-of-view, a polynomial surface fitting is performed for each aberration, thus creating the aberration maps. The aberration maps enable the query of aberration amount at any location through the field-of-view for further accurate localization or realistic image simulation.

By comparing with simplified analytical model, specifically, double Gaussian model for DH-PSFs, we show that the spatially-variant vectorial PSF model outperform the double Gaussian model. It can resolve the 3D localizations of emitters with both better accuracy and higher precision. Moreover, careful measurements show that it can localize the same emitters in two color channels with a *z*-colocalization accuracies of less than 25 nm, which lies in the precision range of common live cell imaging.

In this work, we use a phase mask that engineers a regular PSF into a double-helix PSF. Groups have reported other engineered PSFs, such as tetrapod [77], and learned PSF [81]. In our model we take other important factors into account, to be specific, the emitter dipole, the refractive index boundary. We believe that our model can be extended to characterize other models corresponding to differently engineered PSF, anisotropic emitters such as a fixed dipole in refractive index mismatched medium. Li *et al.* interpolated experimental PSFs to reconstruct a complete and realist PSF models which contain the aberrations in the optical system [29]. Alternatively, spatially-variant interpolated PSFs could be generated based on the method presented here. Such an approach would result in improved localization accuracy, because locally-aberrated PSF models could be used for interpolation by computationally moving the emitter to different *z*-positions instead of experimentally scanning the nominal focal plane through emitters at constant (but unknown) *z*-position. Recently years, deep leaning has been used to characterize or correct the aberrations in the optical system [31, 180, 181]. Spatially-variant PSF can be used to simulate training data that reflect possible experimental images, thus improving the accuracy of result from deep learning.

Limitations of the approach include the inability to calibrate the thickness variation of microscope coverslips *in situ*. Unknown undulations in the refractive index boundary limit the accuracy in Zernike coefficients estimation and thus the absolute *z*-localization accuracy to tens of nanometers, as quantified in Fig. 4.7. The substantial computational cost limits us to Zernike polynomials only up to $j = 15$, which leaves out aberrations of higher order. The heterogeneity of refractive index within sample is not considered in the model yet. These limitations leave space for future improvements that will be discussed in Chapter 5.

Chapter 5: Significances and Future Directions

5.1 Significances

As a powerful tool, SMLM is widely used and has enabled many important and interesting discoveries in biology. It has been used to determine the structure [182] or conformational changes [15] of macrostructures or individual proteins. Borrowing methods from cryo-electron microscopy, such as classification and single-particle averaging, scientists were able to determine the structure of complex macromolecular organizations [182-184]. Leveraging slowed photochemistry at cryogenic temperatures, Weisenburger *et al.* were able to localize fluorophores at different sites of a small protein with Angstrom-level precision [185]. It has also been used to count protein copy number [186], and in multicolor colocalization microscopy [14, 170]. In addition to static localization, the capability of SMLM to observe at the single molecule level allows the dynamic movement of individual molecules to be tracked.

The first half of this dissertation describes the application of SMLM in single-molecule tracking. On the basis of previous work [111], this work focuses on extending and further validating the diffusion analysis framework to resolve the prevalent diffusive states of freely diffusing cytoplasmic proteins. The previous framework is slightly modified and updated. Previous work involved both simulated data and experimental data with an exposure time of 25 ms and it handled fluorescent proteins eYFP and mEos3.2 in *Yersinia enterocolitica*. To further validate the framework, we simulated data with an exposure time of 10 ms to mimic experimental single molecule tracking data. By subjecting the simulated data to the same localization and tracking workflow, we created distributions of apparent diffusion coefficients in a confined cellular volume with known unconfined diffusion coefficients. Experimental data is fit with these distributions to resolve the diffusive states

and the relative population fractions. The fluorescent protein mEos3.2 diffusing in *Y. enterocolitica* cytosol was analyzed. We found that experimental data at exposure times of 25 ms and 10 ms were fit well with the same state, which supports the underlying hypothesis that cytosolic mEos3.2 undergoes confined Brownian motion in *Y. enterocolitica*.

While SMLM is widely used for its excellent performance, the aberrations intrinsic in the optical system or introduced by samples have hindered localization accuracy and precision. The second half of this dissertation is dedicated to the efforts to computationally quantify the aberrations present in the optical system. We take into account the spatial variance of aberrations, which must be corrected to image a large field-of-view. By sampling points at different locations across a large field-of-view and fitting the aberration coefficients to polynomial functions, we generated aberration coefficient maps for the two color channels in a single molecule localization microscope. The aberrations can be computationally corrected, and our PSF model is able to localize emitters with better accuracy and precision than commonly used double-Gaussian model for DH-PSFs. With slight modifications, this aberration correction model can be extended to other engineered PSFs.

5.2 Future directions

Single-molecule tracking with SMLM is able to provide invaluable information of biomolecular behavior in its native environment. Fluorescent proteins provide high specificity because they can be genetically inserted and expressed together with the protein of interest. However, as discussed in Chapter 2, the main drawback of fluorescent proteins

is that they are dimmer than organic dyes. This leads to larger localization uncertainty and short trajectories. Previous work has shown that increasing the trajectory length helps extract information on dynamics [111]. In the future, efforts can be made to use other labelling methods to get longer trajectories, such as dye labeling or unnatural amino acid labeling. Fluorescent dyes with high photon yields enable localizing molecules of interest with better precision. The use of noncanonical amino acids (ncAAs) provides high specificity, and it can be combined with the use of bright fluorophores. Either method has to deal with the problem of artifacts introduced by possible non-specific labelling or high levels of background due to insufficient wash of free dyes. Live cell imaging compatibility and cell permeability of fluorophores are other issues that need considering when choosing a labeling system. In the case of ncAAs, researchers may have to consider possible complications of introducing orthogonal pairs of tRNAs and aminoacyl-tRNA synthetases into cells.

Future directions of the protein diffusion analysis framework include improvement of the fit quality. As shown in Fig. 3.6, especially for experimental data with an exposure time of 10 ms, the fit is not perfect yet. On the other hand, the assumption in the simulation of single molecule trajectories is that the proteins are diffusing in a Brownian way in a confined homogenous volume. The assumption is justifiable in our case because the localizations and diffusing trajectories (data not shown) do not show any spatial dependence. It has been reported that molecules can undergo subdiffusion in bacterial cells due to interaction with surroundings, especially for larger moving molecules [187, 188]. Future work can investigate diffusion in a heterogenous volume. It can also include the

comparison between subdiffusion and confined Brownian motion, which may reveal the possibility to probe unseen molecular movement.

The aberrations in optical systems are difficult to remove. In addition to efforts in industry to manufacture optical components of high quality, future studies can focus on improving the performance of existing models. The model presented in this dissertation incorporates Zernike polynomials up to mode $j = 15$. However, it is beneficial to include additional Zernike modes beyond $j = 15$ to account for aberrations of higher order. This will increase the computational cost, but this problem can be mitigated by using Graphics Processing Units (GPUs) or cloud computing services. The heterogeneity of the refractive index within the imaged specimen contributes to the inaccuracy of localization, which should be modeled. This, however, is not easy due to the fact that the heterogeneity is unknown and may be specimen-dependent. More extensive calibration measurements and incorporation of the fine bandwidth of the fluorescence emission spectrum may also help to improve the accuracy of aberration coefficient estimation. It will further improve the agreement between simulated and experimental PSFs.

Applying this new PSF model to biological samples can lead to important findings. In recent years, deep learning has been used to characterize and/or correct for the aberrations [31, 180, 181]. The computational power of deep learning enables fast localization of emitters. It is possible that the combination of deep learning and the spatially-variant vectorial PSF model could lead to fast and accurate results simultaneously. This can be further incorporated into the existing single-molecule tracking workflow.

On the microscopy front, future efforts can be made to develop correlative microscopy that combines different imaging modalities and leverage the complementary strengths

[189]. Expansion microscopy (ExM) was first reported in 2015 by Chen *et al.* [190], and was later updated to be compatible with commonly used fluorophores and fluorescent proteins [191, 192]. Briefly, proteins or fluorophores are anchored to a swellable gel, and then the distance between them are increased isotopically when the gel expands. Iterative expansion microscopy [193] combined with global labelling has enabled the visualization of the nanoarchitecture of eukaryotic cells with electron microscopy-like contrast [194]. By imaging the isotopically swelled samples from ExM, aberration-corrected SMLM is able to provide accurate and precise estimation of localization and copy number of proteins that are otherwise crowded in a tight complex. For instance, type III secretion system (T3SS) is such a macromolecular complex, which is used by many pathogenic bacteria as a virulence mechanism to infect host cells [195]. The relative stoichiometry of some proteins within T3SS is still under debate and could benefit from rigorous SMLM paired with ExM. However, the rigid cell wall poses technical issues for expansion. It is important to note that this correlative technique requires fixation of the sample, and thus is not able to provide dynamic information.

5.3 Conclusions

The work presented here validates the robustness of a protein diffusion analysis framework. When applied to experimental data collected at different exposure times, this framework is able to resolve the diffusive states of fluorescent proteins diffusing in living cells. Specifically, we characterized the diffusion of the fluorescent protein mEos3.2 as undergoing confined Brownian motion. To improve the localization accuracy and precision of single molecule localization microscopy, a phase-retrieved vectorial PSF model is

introduced to correct for spatially-variant aberrations in ultra-wide field-of-view imaging. The applications and limitations of the work are thoroughly discussed. Further application and improvement of the protein diffusion analysis in an aberration-corrected single-molecule microscope will facilitate better understanding of molecule behavior.

References

1. S. W. Hell, and J. Wichmann, "Breaking the diffraction resolution limit by stimulated emission: stimulated-emission-depletion fluorescence microscopy," Opt. Lett. **19**, 780-782 (1994).
2. M. J. Rust, M. Bates, and X. Zhuang, "Sub-diffraction-limit imaging by stochastic optical reconstruction microscopy (STORM)," Nat. Methods **3**, 793-795 (2006).
3. E. Betzig, R. Patterson Gh Fau - Sougrat, O. W. Sougrat R Fau - Lindwasser, S. Lindwasser Ow Fau - Olenych, J. S. Olenych S Fau - Bonifacino, M. W. Bonifacino Js Fau - Davidson, J. Davidson Mw Fau - Lippincott-Schwartz, H. F. Lippincott-Schwartz J Fau - Hess, and H. F. Hess, "Imaging intracellular fluorescent proteins at nanometer resolution."
4. S. T. Hess, T. P. Girirajan, and M. D. Mason, "Ultra-high resolution imaging by fluorescence photoactivation localization microscopy," Biophys J **91**, 4258-4272 (2006).
5. L. Mockl, D. C. Lamb, and C. Brauchle, "Super-resolved fluorescence microscopy: Nobel Prize in Chemistry 2014 for Eric Betzig, Stefan Hell, and William E. Moerner," Angew Chem Int Ed Engl **53**, 13972-13977 (2014).
6. S. W. Hell, and M. Kroug, "Ground-state-depletion fluorscence microscopy: A concept for breaking the diffraction resolution limit," Appl. Phys. B **60**, 495-497 (1995).
7. M. Hofmann, C. Eggeling, S. Jakobs, and S. W. Hell, "Breaking the diffraction barrier in fluorescence microscopy at low light intensities by using reversibly photoswitchable proteins," Proc. Natl. Acad. Sci. U. S. A. **102**, 17565-17569 (2005).
8. J. Keller, A. Schönle, and S. W. Hell, "Efficient fluorescence inhibition patterns for RESOLFT microscopy," Opt. Express **15**, 3361-3371 (2007).
9. M. G. L. Gustafsson, "Surpassing the lateral resolution limit by a factor of two using structured illumination microscopy," J. Microsc. **198**, 82-87 (2000).
10. M. Heilemann, S. van de Linde, M. Schuttpelz, R. Kasper, B. Seefeldt, A. Mukherjee, P. Tinnefeld, and M. Sauer, "Subdiffraction-resolution fluorescence imaging with conventional fluorescent probes," Angew Chem Int Ed Engl **47**, 6172-6176 (2008).
11. A. Gahlmann, and W. E. Moerner, "Exploring bacterial cell biology with single-molecule tracking and super-resolution imaging," Nat Rev Microbiol **12**, 9-22 (2014).
12. X. Mao, C. Liu, M. Hesari, N. Zou, and P. Chen, "Super-resolution imaging of non-fluorescent reactions via competition," Nat Chem **11**, 687-694 (2019).
13. V. J. Sabinina, M. J. Hossain, J.-K. Hériché, P. Hoess, B. Nijmeijer, S. Mosalaganti, M. Kueblbeck, A. Callegari, A. Szymborska, M. Beck, J. Ries, and J. Ellenberg, "3D super-resolution fluorescence microscopy maps the variable molecular architecture of the Nuclear Pore Complex," bioRxiv, 2020.2011.2027.386599 (2020).
14. A. Gahlmann, J. L. Ptacin, G. Grover, S. Quirin, A. R. von Diezmann, M. K. Lee, M. P. Backlund, L. Shapiro, R. Piestun, and W. E. Moerner, "Quantitative multicolor subdiffraction imaging of bacterial protein ultrastructures in three dimensions," Nano Lett **13**, 987-993 (2013).
15. T. I. Moore, J. Aaron, T. L. Chew, and T. A. Springer, "Measuring Integrin Conformational Change on the Cell Surface with Super-Resolution Microscopy," Cell Rep **22**, 1903-1912 (2018).
16. C. Manzo, and M. F. Garcia-Parajo, "A review of progress in single particle tracking: from methods to biophysical insights," Rep. Prog. Phys. **78**, 124601 (2015).
17. M. F. Juette, T. J. Gould, M. D. Lessard, M. J. Mlodzianoski, B. S. Nagpure, B. T. Bennett, S. T. Hess, and J. Bewersdorf, "Three-dimensional sub-100 nm resolution fluorescence microscopy of thick samples," Nat. Methods **5**, 527-529 (2008).

18. G. Shtengel, J. A. Galbraith, C. G. Galbraith, J. Lippincott-Schwartz, J. M. Gillette, S. Manley, R. Sougrat, C. M. Waterman, P. Kanchanawong, M. W. Davidson, R. D. Fetter, and H. F. Hess, "Interferometric fluorescent super-resolution microscopy resolves 3D cellular ultrastructure," Proceedings of the National Academy of Sciences **106**, 3125-3130 (2009).
19. S. R. P. Pavani, and R. Piestun, "Three dimensional tracking of fluorescent microparticles using a photon-limited double-helix response system," Opt. Express **16**, 22048-22057 (2008).
20. G. R. Bullock, "The current status of fixation for electron microscopy: A review," J. Microsc. **133**, 1-15 (1984).
21. C. M. Oikonomou, and G. J. Jensen, "A new view into prokaryotic cell biology from electron cryotomography," Nat Rev Microbiol **14**, 205-220 (2016).
22. G. Rayan, J. E. Guet, N. Taulier, F. Pincet, and W. Urbach, "Recent applications of fluorescence recovery after photobleaching (FRAP) to membrane bio-macromolecules," Sensors (Basel) **10**, 5927-5948 (2010).
23. V. Bayle, J. B. Fiche, C. Burny, M. P. Platre, M. Nollmann, A. Martiniere, and Y. Jaillais, "Single-particle tracking photoactivated localization microscopy of membrane proteins in living plant tissues," Nat. Protoc. (2021).
24. F. Persson, M. Linden, C. Unoson, and J. Elf, "Extracting intracellular diffusive states and transition rates from single-molecule tracking data," Nat. Methods **10**, 265-269 (2013).
25. E. M. M. Manders, "Chromatic shift in multicolour confocal microscopy," J. Microsc. **185**, 321-328 (1997).
26. A. Matsuda, L. Schermelleh, Y. Hirano, T. Haraguchi, and Y. Hiraoka, "Accurate and fiducial-marker-free correction for three-dimensional chromatic shift in biological fluorescence microscopy," Sci Rep **8**, 7583 (2018).
27. R. E. Thompson, D. R. Larson, and W. W. Webb, "Precise Nanometer Localization Analysis for Individual Fluorescent Probes," Biophys. J. **82**, 2775-2783 (2002).
28. N. Ji, "Adaptive optical fluorescence microscopy," Nat. Methods **14**, 374-380 (2017).
29. Y. Li, M. Mund, P. Hoess, J. Deschamps, U. Matti, B. Nijmeijer, V. J. Sabinina, J. Ellenberg, I. Schoen, and J. Ries, "Real-time 3D single-molecule localization using experimental point spread functions," Nat. Methods **15**, 367-369 (2018).
30. A. S. Backer, and W. E. Moerner, "Extending single-molecule microscopy using optical Fourier processing," J Phys Chem B **118**, 8313-8329 (2014).
31. L. Mockl, P. N. Petrov, and W. E. Moerner, "Accurate phase retrieval of complex 3D point spread functions with deep residual neural networks," Appl Phys Lett **115**, 251106 (2019).
32. P. N. Petrov, Y. Shechtman, and W. E. Moerner, "Measurement-based estimation of global pupil functions in 3D localization microscopy," Opt. Express **25**, 7945-7959 (2017).
33. F. Huang, T. M. Hartwich, F. E. Rivera-Molina, Y. Lin, W. C. Duim, J. J. Long, P. D. Uchil, J. R. Myers, M. A. Baird, W. Mothes, M. W. Davidson, D. Toomre, and J. Bewersdorf, "Video-rate nanoscopy using sCMOS camera-specific single-molecule localization algorithms," Nat. Methods **10**, 653-658 (2013).
34. A. von Diezmann, M. Y. Lee, M. D. Lew, and W. E. Moerner, "Correcting field-dependent aberrations with nanoscale accuracy in three-dimensional single-molecule localization microscopy," Optica **2**, 985-993 (2015).
35. E. Abbe, "Beiträge zur Theorie des Mikroskops und der mikroskopischen Wahrnehmung," Archiv für Mikroskopische Anatomie **9**, 413-468 (1873).
36. W. Liu, K. C. Toussaint, C. Okoro, D. Zhu, Y. Chen, C. Kuang, and X. Liu, "Breaking the Axial Diffraction Limit: A Guide to Axial Super-Resolution Fluorescence Microscopy," Laser & Photonics Reviews **12** (2018).

37. M. Osborn, R. E. Webster, and K. Weber, "Individual microtubules viewed by immunofluorescence and electron microscopy in the same PtK2 cell," J. Cell Biol. **77**, R27-R27 (1978).
38. B. O. Leung, and K. C. Chou, "Review of super-resolution fluorescence microscopy for biology," Appl Spectrosc **65**, 967-980 (2011).
39. A. G. Godin, B. Lounis, and L. Cognet, "Super-resolution microscopy approaches for live cell imaging," Biophys J **107**, 1777-1784 (2014).
40. C. Coltharp, and J. Xiao, "Superresolution microscopy for microbiology," Cell. Microbiol. **14**, 1808-1818 (2012).
41. S. Pujals, N. Feiner-Gracia, P. Delcanale, I. Voets, and L. Albertazzi, "Super-resolution microscopy as a powerful tool to study complex synthetic materials," Nature Reviews Chemistry **3**, 68-84 (2019).
42. W. E. Moerner, and L. Kador, "Optical detection and spectroscopy of single molecules in a solid," Phys Rev Lett **62**, 2535-2538 (1989).
43. Y. Sako, S. Minoghchi, and T. Yanagida, "Single-molecule imaging of EGFR signalling on the surface of living cells," Nat. Cell Biol. **2**, 168-172 (2000).
44. T. Funatsu, Y. Harada, M. Tokunaga, K. Saito, and T. Yanagida, "Imaging of single fluorescent molecules and individual ATP turnovers by single myosin molecules in aqueous solution," Nature **374**, 555-559 (1995).
45. R. Diekmann, M. Kahnwald, A. Schoenit, J. Deschamps, U. Matti, and J. Ries, "Optimizing imaging speed and excitation intensity for single-molecule localization microscopy," Nat. Methods **17**, 909-912 (2020).
46. G. H. Patterson, and J. Lippincott-Schwartz, "A photoactivatable GFP for selective photolabeling of proteins and cells."
47. G. Patterson, M. Davidson, S. Manley, and J. Lippincott-Schwartz, "Superresolution imaging using single-molecule localization," Annu Rev Phys Chem **61**, 345-367 (2010).
48. N. C. Shaner, G. H. Patterson, and M. W. Davidson, "Advances in fluorescent protein technology," J Cell Sci **120**, 4247-4260 (2007).
49. O. Shimomura, F. H. Johnson, and Y. Saiga, "Extraction, Purification and Properties of Aequorin, a Bioluminescent Protein from the Luminous Hydromedusan, Aequorea," Journal of Cellular and Comparative Physiology **59**, 223-239 (1962).
50. F. H. Johnson, O. Shimomura, Y. Saiga, L. C. Gershman, G. T. Reynolds, and J. R. Waters, "Quantum efficiency of Cypridina luminescence, with a note on that of Aequorea," Journal of Cellular and Comparative Physiology **60**, 85-103 (1962).
51. H. Morise, O. Shimomura, F. H. Johnson, and J. Winant, "Intermolecular energy transfer in the bioluminescent system of Aequorea," Biochemistry **13**, 2656-2662 (1974).
52. O. Shimomura, "Structure of the chromophore of Aequorea green fluorescent protein," FEBS Lett. **104**, 220-222 (1979).
53. M. V. Matz, A. F. Fradkov, Y. A. Labas, A. P. Savitsky, A. G. Zaraisky, M. L. Markelov, and S. A. Lukyanov, "Fluorescent proteins from nonbioluminescent Anthozoa species," Nat. Biotechnol. **17**, 969-973 (1999).
54. L. A. Gross, G. S. Baird, R. C. Hoffman, K. K. Baldridge, and R. Y. Tsien, "The structure of the chromophore within DsRed, a red fluorescent protein from coral," Proceedings of the National Academy of Sciences **97**, 11990-11995 (2000).
55. D. D. Deheyn, K. Kubokawa, J. K. McCarthy, A. Murakami, M. Porrachia, G. W. Rouse, and N. D. Holland, "Endogenous Green Fluorescent Protein (GFP) in Amphioxus," Biol. Bull. **213**, 95-100 (2007).

56. M. Zhang, H. Chang, Y. Zhang, J. Yu, L. Wu, W. Ji, J. Chen, B. Liu, J. Lu, Y. Liu, J. Zhang, P. Xu, and T. Xu, "Rational design of true monomeric and bright photoactivatable fluorescent proteins," Nat. Methods **9**, 727-729 (2012).
57. M. Fernandez-Suarez, and A. Y. Ting, "Fluorescent probes for super-resolution imaging in living cells," Nat Rev Mol Cell Biol **9**, 929-943 (2008).
58. R. Feng, Y. Sun, M. Tian, G. Zhang, R. Zhang, L. Guo, X. Li, X. Yu, and N. Zhao, "A membrane-permeable dye for living cells with large two-photon excited fluorescence action cross-sections for bioimaging," J Mater Chem B **3**, 8644-8649 (2015).
59. C. E. Shannon, "Communication in the Presence of Noise," Proceedings of the IRE **37**, 10-21 (1949).
60. H. Shroff, C. G. Galbraith, J. A. Galbraith, and E. Betzig, "Live-cell photoactivated localization microscopy of nanoscale adhesion dynamics," Nat. Methods **5**, 417-423 (2008).
61. I. Chen, and A. Y. Ting, "Site-specific labeling of proteins with small molecules in live cells," Curr Opin Biotechnol **16**, 35-40 (2005).
62. L. Xue, I. A. Karpenko, J. Hiblot, and K. Johnsson, "Imaging and manipulating proteins in live cells through covalent labeling," Nat. Chem. Biol. **11**, 917-923 (2015).
63. J. B. Grimm, B. P. English, H. Choi, A. K. Muthusamy, B. P. Mehl, P. Dong, T. A. Brown, J. Lippincott-Schwartz, Z. Liu, T. Lionnet, and L. D. Lavis, "Bright photoactivatable fluorophores for single-molecule imaging," Nat. Methods **13**, 985-988 (2016).
64. A. Keppler, H. Pick, C. Arrivoli, H. Vogel, and K. Johnsson, "Labeling of fusion proteins with synthetic fluorophores in live cells," Proc. Natl. Acad. Sci. U. S. A. **101**, 9955-9959 (2004).
65. A. Gautier, A. Juillerat, C. Heinis, I. R. Correa, Jr., M. Kindermann, F. Beaufils, and K. Johnsson, "An engineered protein tag for multiprotein labeling in living cells," Chem Biol **15**, 128-136 (2008).
66. G. V. Los, L. P. Encell, M. G. McDougall, D. D. Hartzell, N. Karassina, C. Zimprich, M. G. Wood, R. Learish, R. F. Ohana, M. Urh, D. Simpson, J. Mendez, K. Zimmerman, P. Otto, G. Vidugiris, J. Zhu, A. Darzins, D. H. Klaubert, R. F. Bulleit, and K. V. Wood, "HaloTag: A Novel Protein Labeling Technology for Cell Imaging and Protein Analysis," ACS Chem. Biol. **3**, 373-382 (2008).
67. I. C. Vreja, I. Nikić, F. Göttfert, M. Bates, K. Kröhnert, T. F. Outeiro, S. W. Hell, E. A. Lemke, and S. O. Rizzoli, "Super-resolution Microscopy of Clickable Amino Acids Reveals the Effects of Fluorescent Protein Tagging on Protein Assemblies," ACS Nano **9**, 11034-11041 (2015).
68. M. E. Tanenbaum, L. A. Gilbert, L. S. Qi, J. S. Weissman, and R. D. Vale, "A protein-tagging system for signal amplification in gene expression and fluorescence imaging," Cell **159**, 635-646 (2014).
69. I. Nikic, J. H. Kang, G. E. Girona, I. V. Aramburu, and E. A. Lemke, "Labeling proteins on live mammalian cells using click chemistry," Nat. Protoc. **10**, 780-791 (2015).
70. J. Deschamps, M. Mund, and J. Ries, "3D superresolution microscopy by supercritical angle detection," Opt. Express **22**, 29081-29091 (2014).
71. N. Bourg, C. Mayet, G. Dupuis, T. Barroca, P. Bon, S. Lécart, E. Fort, and S. Lévêque-Fort, "Direct optical nanoscopy with axially localized detection," Nature Photonics **9**, 587-593 (2015).
72. C. Cabriel, N. Bourg, P. Jouchet, G. Dupuis, C. Leterrier, A. Baron, M. A. Badet-Denisot, B. Vauzeilles, E. Fort, and S. Leveque-Fort, "Combining 3D single molecule localization strategies for reproducible bioimaging," Nat Commun **10**, 1980 (2019).
73. P. Prabhat, S. Ram, E. S. Ward, and R. J. Ober, "Simultaneous Imaging of Different Focal Planes in Fluorescence Microscopy for the Study of Cellular Dynamics in Three Dimensions," IEEE Transactions on Nanobioscience **3**, 237-242 (2004).
74. F. Huang, G. Sirinakis, E. S. Allgeyer, L. K. Schroeder, W. C. Duim, E. B. Kromann, T. Phan, F. E. Rivera-Molina, J. R. Myers, I. Irnov, M. Lessard, Y. Zhang, M. A. Handel, C. Jacobs-Wagner, C.

P. Lusk, J. E. Rothman, D. Toomre, M. J. Booth, and J. Bewersdorf, "Ultra-High Resolution 3D Imaging of Whole Cells," Cell **166**, 1028-1040 (2016).
75. B. Huang, W. Wang, M. Bates, and X. Zhuang, "Three-dimensional super-resolution imaging by stochastic optical reconstruction microscopy," Science **319**, 810-813 (2008).
76. S. R. Pavani, M. A. Thompson, J. S. Biteen, S. J. Lord, N. Liu, R. J. Twieg, R. Piestun, and W. E. Moerner, "Three-dimensional, single-molecule fluorescence imaging beyond the diffraction limit by using a double-helix point spread function," Proc. Natl. Acad. Sci. U. S. A. **106**, 2995-2999 (2009).
77. Y. Shechtman, L. E. Weiss, A. S. Backer, S. J. Sahl, and W. E. Moerner, "Precise Three-Dimensional Scan-Free Multiple-Particle Tracking over Large Axial Ranges with Tetrapod Point Spread Functions," Nano Lett **15**, 4194-4199 (2015).
78. M. D. Lew, S. F. Lee, M. Badieirostami, and W. E. Moerner, "Corkscrew point spread function for far-field three-dimensional nanoscale localization of pointlike objects," Opt. Lett. **36**, 202-204 (2011).
79. A. S. Backer, M. P. Backlund, A. R. von Diezmann, S. J. Sahl, and W. E. Moerner, "A bisected pupil for studying single-molecule orientational dynamics and its application to three-dimensional super-resolution microscopy," Appl Phys Lett **104**, 193701 (2014).
80. S. Jia, J. C. Vaughan, and X. Zhuang, "Isotropic 3D Super-resolution Imaging with a Self-bending Point Spread Function," Nat. Photon **8**, 302-306 (2014).
81. E. Nehme, D. Freedman, R. Gordon, B. Ferdman, L. E. Weiss, O. Alalouf, T. Naor, R. Orange, T. Michaeli, and Y. Shechtman, "DeepSTORM3D: dense 3D localization microscopy and PSF design by deep learning," Nat. Methods **17**, 734-740 (2020).
82. H. Deschout, F. Cella Zanacchi, M. Mlodzianoski, A. Diaspro, J. Bewersdorf, S. T. Hess, and K. Braeckmans, "Precisely and accurately localizing single emitters in fluorescence microscopy," Nat. Methods **11**, 253-266 (2014).
83. K. A. Winick, "Cramér–Rao lower bounds on the performance of charge-coupled-device optical position estimators," Journal of the Optical Society of America A **3**, 1809-1815 (1986).
84. J. Chao, E. Sally Ward, and R. J. Ober, "Fisher information theory for parameter estimation in single molecule microscopy: tutorial," J Opt Soc Am A Opt Image Sci Vis **33**, B36-57 (2016).
85. R. Henriques, M. Lelek, E. F. Fornasiero, F. Valtorta, C. Zimmer, and M. M. Mhlanga, "QuickPALM: 3D real-time photoactivation nanoscopy image processing in ImageJ," Nat. Methods **7**, 339-340 (2010).
86. R. Parthasarathy, "Rapid, accurate particle tracking by calculation of radial symmetry centers," Nat. Methods **9**, 724-726 (2012).
87. A. Small, and S. Stahlheber, "Fluorophore localization algorithms for super-resolution microscopy," Nat. Methods **11**, 267-279 (2014).
88. C. S. Smith, N. Joseph, B. Rieger, and K. A. Lidke, "Fast, single-molecule localization that achieves theoretically minimum uncertainty," Nat. Methods **7**, 373-375 (2010).
89. A. V. Abraham, S. Ram, J. Chao, E. S. Ward, and R. J. Ober, "Quantitative study of single molecule location estimation techniques," Opt. Express **17**, 23352-23373 (2009).
90. K. I. Mortensen, L. S. Churchman, J. A. Spudich, and H. Flyvbjerg, "Optimized localization analysis for single-molecule tracking and super-resolution microscopy," Nat. Methods **7**, 377-381 (2010).
91. H. Mazidi, T. Ding, A. Nehorai, and M. D. Lew, "Quantifying accuracy and heterogeneity in single-molecule super-resolution microscopy," Nat Commun **11**, 6353 (2020).
92. N. Gustafsson, S. Culley, G. Ashdown, D. M. Owen, P. M. Pereira, and R. Henriques, "Fast live-cell conventional fluorophore nanoscopy with ImageJ through super-resolution radial fluctuations," Nat Commun **7**, 12471 (2016).

93. H. Mazidi, J. Lu, A. Nehorai, and M. D. Lew, "Minimizing Structural Bias in Single-Molecule Super-Resolution Microscopy," Sci Rep **8**, 13133 (2018).
94. J. Min, C. Vonesch, H. Kirshner, L. Carlini, N. Olivier, S. Holden, S. Manley, J. C. Ye, and M. Unser, "FALCON: fast and unbiased reconstruction of high-density super-resolution microscopy data," Sci Rep **4**, 4577 (2014).
95. S. J. Holden, S. Uphoff, and A. N. Kapanidis, "DAOSTORM: an algorithm for high- density super-resolution microscopy," Nat. Methods **8**, 279-280 (2011).
96. J. Yu, J. Xiao, X. Ren, K. Lao, and X. S. Xie, "Probing Gene Expression in Live Cells, One Protein Molecule at a Time," Science **311**, 1600-1603 (2006).
97. S. Waldchen, J. Lehmann, T. Klein, S. van de Linde, and M. Sauer, "Light-induced cell damage in live-cell super-resolution microscopy," Sci Rep **5**, 15348 (2015).
98. R. A. Hoebe, C. H. Van Oven, T. W. Gadella, Jr., P. B. Dhonukshe, C. J. Van Noorden, and E. M. Manders, "Controlled light-exposure microscopy reduces photobleaching and phototoxicity in fluorescence live-cell imaging," Nat. Biotechnol. **25**, 249-253 (2007).
99. H. Schneckenburger, P. Weber, M. Wagner, S. Schickinger, V. Richter, T. Bruns, W. S. Strauss, and R. Wittig, "Light exposure and cell viability in fluorescence microscopy," J Microsc **245**, 311-318 (2012).
100. D. A. Helmerich, G. Beliu, S. S. Matikonda, M. J. Schnermann, and M. Sauer, "Photoblueing of organic dyes can cause artifacts in super-resolution microscopy," Nat. Methods (2021).
101. T. Bernas, J. W. Zarebski M Fau - Dobrucki, P. R. Dobrucki Jw Fau - Cook, and P. R. Cook, "Minimizing photobleaching during confocal microscopy of fluorescent probes bound to chromatin: role of anoxia and photon flux."
102. J. K. Sugden, "Photochemistry of dyes and fluorochromes used in biology and medicine: some physicochemical background and current applications."
103. Q. Zheng, S. Jockusch, Z. Zhou, and S. C. Blanchard, "The contribution of reactive oxygen species to the photobleaching of organic fluorophores," Photochem. Photobiol. **90**, 448-454 (2014).
104. J. Icha, M. Weber, J. C. Waters, and C. Norden, "Phototoxicity in live fluorescence microscopy, and how to avoid it," Bioessays **39** (2017).
105. C. C. Winterbourn, "Reconciling the chemistry and biology of reactive oxygen species," Nat. Chem. Biol. **4**, 278-286 (2008).
106. J. H. Stockley, K. Evans, M. Matthey, K. Volbracht, S. Agathou, J. Mukanowa, J. Burrone, and R. T. Karadottir, "Surpassing light-induced cell damage in vitro with novel cell culture media," Sci Rep **7**, 849 (2017).
107. K. N. Fish, "Total internal reflection fluorescence (TIRF) microscopy," Curr Protoc Cytom **Chapter 12**, Unit12 18 (2009).
108. C. Dunsby, "Optically sectioned imaging by oblique plane microscopy," Opt. Express **16**, 20306-20316 (2008).
109. B. C. Chen, W. R. Legant, K. Wang, L. Shao, D. E. Milkie, M. W. Davidson, C. Janetopoulos, X. S. Wu, J. A. Hammer, 3rd, Z. Liu, B. P. English, Y. Mimori-Kiyosue, D. P. Romero, A. T. Ritter, J. Lippincott-Schwartz, L. Fritz-Laylin, R. D. Mullins, D. M. Mitchell, J. N. Bembenek, A. C. Reymann, R. Bohme, S. W. Grill, J. T. Wang, G. Seydoux, U. S. Tulu, D. P. Kiehart, and E. Betzig, "Lattice light-sheet microscopy: imaging molecules to embryos at high spatiotemporal resolution," Science **346**, 1257998 (2014).
110. A. Sharonov, and R. M. Hochstrasser, "Wide-field subdiffraction imaging by accumulated binding of diffusing probes," Proceedings of the National Academy of Sciences **103**, 18911-18916 (2006).

111. J. Rocha, J. Corbitt, T. Yan, C. Richardson, and A. Gahlmann, "Resolving Cytosolic Diffusive States in Bacteria by Single-Molecule Tracking," Biophys J **116**, 1970-1983 (2019).
112. J. M. Rocha, and A. Gahlmann, "Single-Molecule Tracking Microscopy - A Tool for Determining the Diffusive States of Cytosolic Molecules. LID - 10.3791/59387 [doi]."
113. J. Rocha, "Dynamic Assembly of the Type-3 Secretion System in Yersinia enterocolitica Probed by Super-Resolution Fluorescence Imaging," https://doi.org/10.18130/v18133-qqs18133-et18140 (2021).
114. M. Ormö, A. B. Cubitt, K. Kallio, L. A. Gross, R. Y. Tsien, and S. J. Remington, "Crystal Structure of the Aequorea victoria Green Fluorescent Protein," Science **273**, 1392-1395 (1996).
115. I. Izeddin, M. El Beheiry, J. Andilla, D. Ciepielewski, X. Darzacq, and M. Dahan, "PSF shaping using adaptive optics for three-dimensional single-molecule super-resolution imaging and tracking," Opt. Express **20**, 4957-4967 (2012).
116. P. Almada, S. Culley, and R. Henriques, "PALM and STORM: Into large fields and high-throughput microscopy with sCMOS detectors," Methods **88**, 109-121 (2015).
117. K. M. Douglass, C. Sieben, A. Archetti, A. Lambert, and S. Manley, "Super-resolution imaging of multiple cells by optimised flat-field epi-illumination," Nat. Photon **10**, 705-708 (2016).
118. Z. Zhao, B. Xin, L. Li, and Z. L. Huang, "High-power homogeneous illumination for super-resolution localization microscopy with large field-of-view," Opt. Express **25**, 13382-13395 (2017).
119. F. Zernike, "Phase contrast, a new method for the microscopic observation of transparent objects," Physica **9**, 686-698 (1942).
120. F. Zernike, "How I Discovered Phase Contrast," Science **121**, 345-349 (1955).
121. H. Matsuda, G. G. Putzel, V. Backman, and I. Szleifer, "Macromolecular crowding as a regulator of gene transcription," Biophys J **106**, 1801-1810 (2014).
122. J. A. Dix, and A. S. Verkman, "Crowding effects on diffusion in solutions and cells," Annu Rev Biophys **37**, 247-263 (2008).
123. B. P. English, V. Hauryliuk, A. Sanamrad, S. Tankov, N. H. Dekker, and J. Elf, "Single-molecule investigations of the stringent response machinery in living bacterial cells," Proc. Natl. Acad. Sci. U. S. A. **108**, E365-373 (2011).
124. A. S. Verkman, "Solute and macromolecule diffusion in cellular aqueous compartments," Trends in Biochemical Sciences **27**, 27-33 (2002).
125. X. Michalet, and A. J. Berglund, "Optimal diffusion coefficient estimation in single-particle tracking."
126. S. Bakshi, B. P. Bratton, and J. C. Weisshaar, "Subdiffraction-limit study of Kaede diffusion and spatial distribution in live Escherichia coli," Biophys J **101**, 2535-2544 (2011).
127. X. Michalet, "Mean square displacement analysis of single-particle trajectories with localization error: Brownian motion in an isotropic medium."
128. J. D. Karslake, E. D. Donarski, S. A. Shelby, L. M. Demey, V. J. DiRita, S. L. Veatch, and J. S. Biteen, "SMAUG: Analyzing single-molecule tracks with nonparametric Bayesian statistics," Methods (2020).
129. S. Mohapatra, H. Choi, X. Ge, S. Sanyal, and J. C. Weisshaar, "Spatial Distribution and Ribosome-Binding Dynamics of EF-P in Live Escherichia coli," mBio **8** (2017).
130. S. Uphoff, R. Reyes-Lamothe, F. Garza de Leon, D. J. Sherratt, and A. N. Kapanidis, "Single-molecule DNA repair in live bacteria," Proc. Natl. Acad. Sci. U. S. A. **110**, 8063-8068 (2013).
131. A. Plochowietz, I. Farrell, Z. Smilansky, B. S. Cooperman, and A. N. Kapanidis, "In vivo single-RNA tracking shows that most tRNA diffuses freely in live bacteria," Nucleic Acids Res **45**, 926-937 (2017).

132. T. Y. Chen, W. Jung, A. G. Santiago, F. Yang, L. Krzeminski, and P. Chen, "Quantifying Multistate Cytoplasmic Molecular Diffusion in Bacterial Cells via Inverse Transform of Confined Displacement Distribution," J Phys Chem B **119**, 14451-14459 (2015).
133. P. K. Koo, and S. G. Mochrie, "Systems-level approach to uncovering diffusive states and their transitions from single-particle trajectories," Phys Rev E **94**, 052412 (2016).
134. D. Lucena, M. Mauri, F. Schmidt, B. Eckhardt, and P. L. Graumann, "Microdomain formation is a general property of bacterial membrane proteins and induces heterogeneity of diffusion patterns," BMC Biol. **16**, 97 (2018).
135. S. Matsuoka, T. Shibata, and M. Ueda, "Statistical analysis of lateral diffusion and multistate kinetics in single-molecule imaging," Biophys J **97**, 1115-1124 (2009).
136. J. M. Rocha, C. J. Richardson, M. Zhang, C. M. Darch, E. Cai, A. Diepold, and A. Gahlmann, "Single-molecule tracking in live Yersinia enterocolitica reveals distinct cytosolic complexes of injectisome subunits," Integr Biol (Camb) **10**, 502-515 (2018).
137. M. Lew, M. D. Lew*, A. R. S. von Diezmann*, and W. E. Moerner, "Easy-DHPSF open-source software for three-dimensional localization of single molecules with precision beyond the optical diffraction limit," Protocol Exchange (2013).
138. Z.-L. Huang, H. Zhu, F. Long, H. Ma, L. Qin, Y. Liu, J. Ding, Z. Zhang, Q. Luo, and S. Zeng, "Localization-based super-resolution microscopy with an sCMOS camera," Opt. Express **19**, 19156-19168 (2011).
139. X. Chen, Z. Zeng, R. Li, B. Xue, P. Xi, and Y. Sun, "Superior performance with sCMOS over EMCCD in super-resolution optical fluctuation imaging," J Biomed Opt **21**, 66007 (2016).
140. A. Paintdakhi, B. Parry, M. Campos, I. Irnov, J. Elf, I. Surovtsev, and C. Jacobs-Wagner, "Oufti: an integrated software package for high-accuracy, high-throughput quantitative microscopy analysis," Mol Microbiol **99**, 767-777 (2016).
141. T. Yan, C. J. Richardson, M. Zhang, and A. Gahlmann, "Computational correction of spatially variant optical aberrations in 3D single-molecule localization microscopy," Opt. Express **27**, 12582-12599 (2019).
142. P. Török, P. Varga, Z. Laczik, and G. R. Booker, "Electromagnetic diffraction of light focused through a planar interface between materials of mismatched refractive indices: an integral representation," Journal of the Optical Society of America A **12**, 325-332 (1995).
143. P. Török, P. Varga, A. Konkol, and G. R. Booker, "Electromagnetic diffraction of light focused through a planar interface between materials of mismatched refractive indices: structure of the electromagnetic field. II," Journal of the Optical Society of America A **13**, 2232-2238 (1996).
144. S. HELL, G. REINER, C. CREMER, and E. H. K. STELZER, "Aberrations in confocal fluorescence microscopy induced by mismatches in refractive index," J. Microsc. **169**, 391-405 (1993).
145. A. Small, "Spherical aberration, coma, and the Abbe sine condition for physicists who don't design lenses," American Journal of Physics **86**, 487-494 (2018).
146. A. W. Lohmann, and D. P. Paris, "Space-variant image formation," J. Opt. Soc. Am. **55**, 1007-1013 (1965).
147. M. Rerabek, and P. Pata, "The space variant PSF for deconvolution of wide-field astronomical images," Proc. SPIE **7015** (2008).
148. M. Rerabek, P. Pata, and K. Fliegel, "Enhancement of the accuracy of the astronomical measurements carried on the wide-field astronomical image data," Proc. SPIE **8135** (2011).
149. E. Sezgin, I. Levental, S. Mayor, and C. Eggeling, "The mystery of membrane organization: composition, regulation and roles of lipid rafts," Nat Rev Mol Cell Biol **18**, 361-374 (2017).
150. H. Walter, and D. E. Brooks, "Phase separation in cytoplasm, due to macromolecular crowding, is the basis for microcompartmentation," FEBS Lett. **361**, 135-139 (1995).

151. M. R. Lindsay, R. I. Webb, M. Strous, M. S. Jetten, M. K. Butler, R. J. Forde, and J. A. Fuerst, "Cell compartmentalisation in planctomycetes: novel types of structural organisation for the bacterial cell," Arch. Microbiol. **175**, 413-429 (2001).
152. G. J. Tearney, M. E. Brezinski, J. F. Southern, B. E. Bouma, M. R. Hee, and J. G. Fujimoto, "Determination of the refractive index of highly scattering human tissue by optical coherence tomography," Opt. Lett. **20**, 2258-2260 (1995).
153. L. E. Bolin Fp Fau - Preuss, R. C. Preuss Le Fau - Taylor, R. J. Taylor Rc Fau - Ference, and R. J. Ference, "Refractive index of some mammalian tissues using a fiber optic cladding method."
154. M. Sheppard Cj Fau - Gu, and M. Gu, "Aberration compensation in confocal microscopy."
155. L. Sherman, J. Y. Ye, O. Albert, and T. B. Norris, "Adaptive correction of depth-induced aberrations in multiphoton scanning microscopy using a deformable mirror," J. Microsc. **206**, 65-71 (2002).
156. B. M. Hanser, M. G. L. Gustafsson, D. A. Agard, and J. W. Sedat, "Phase retrieval for high-numerical-aperture optical systems," Opt. Lett. **28**, 801-803 (2003).
157. B. M. Hanser, M. G. L. Gustafsson, D. A. Agard, and J. W. Sedat, "Phase-retrieved pupil functions in wide-field fluorescence microscopy," J. Microsc. **216**, 32-48 (2004).
158. P. Kner, L. Winoto, D. A. Agard, and J. W. Sedat, "Closed loop adaptive optics for microscopy without a wavefront sensor," Proc SPIE Int Soc Opt Eng **7570** (2010).
159. D. Burke, B. Patton, F. Huang, J. Bewersdorf, and M. J. Booth, "Adaptive optics correction of specimen-induced aberrations in single-molecule switching microscopy," Optica **2**, 177-185 (2015).
160. M. J. Mlodzianoski, P. J. Cheng-Hathaway, S. M. Bemiller, T. J. McCray, S. Liu, D. A. Miller, B. T. Lamb, G. E. Landreth, and F. Huang, "Active PSF shaping and adaptive optics enable volumetric localization microscopy through brain sections," Nat. Methods **15**, 583-586 (2018).
161. R. McGorty, J. Schnitzbauer, W. Zhang, and B. Huang, "Correction of depth-dependent aberrations in 3D single-molecule localization and super-resolution microscopy," Opt. Lett. **39**, 275-278 (2014).
162. A. Tahmasbi, E. S. Ward, and R. J. Ober, "Determination of localization accuracy based on experimentally acquired image sets: applications to single molecule microscopy," Opt. Express **23**, 7630-7652 (2015).
163. H. P. Babcock, and X. Zhuang, "Analyzing Single Molecule Localization Microscopy Data Using Cubic Splines," Sci. Rep **7**, 552 (2017).
164. H. Kirshner, C. Vonesch, and M. Unser, "Can localization microscopy benefit from approximation theory?," in 2013 IEEE 10th International Symposium on Biomedical Imaging(2013), pp. 588-591.
165. C. Smith, M. Huisman, M. Siemons, D. Grunwald, and S. Stallinga, "Simultaneous measurement of emission color and 3D position of single molecules," Opt. Express **24**, 4996-5013 (2016).
166. M. Siemons, C. N. Hulleman, R. O. Thorsen, C. S. Smith, and S. Stallinga, "High precision wavefront control in point spread function engineering for single emitter localization," Opt. Express **26**, 8397-8416 (2018).
167. D. Axelrod, "Fluorescence excitation and imaging of single molecules near dielectric-coated and bare surfaces: a theoretical study," J Microsc **247**, 147-160 (2012).
168. R. J. Noll, "Zernike polynomials and atmospheric turbulence," Journal of the Optical Society of America (1917-1983) **66**, 207 (1976).
169. B. Richards, and E. Wolf, "Electromagnetic diffraction in optical systems, II. Structure of the image field in an aplanatic system," Proc. R. Soc. Lond. A **253**, 358-379 (1959).

170. J. L. Ptacin, A. Gahlmann, G. R. Bowman, A. M. Perez, A. R. von Diezmann, M. R. Eckart, W. E. Moerner, and L. Shapiro, "Bacterial scaffold directs pole-specific centromere segregation," Proc. Natl. Acad. Sci. U. S. A. **111**, E2046-2055 (2014).
171. M. D. Lew, A. R. S. von Diezmann, and W. E. Moerner, "Easy-DHPSF open-source software for three-dimensional localization of single molecules with precision beyond the optical diffraction limit," Protocol Exchange, doi:10.1038/protex.2013.1026 (2013).
172. L. Carlini, S. J. Holden, K. M. Douglass, and S. Manley, "Correction of a Depth-Dependent Lateral Distortion in 3D Super-Resolution Imaging," PLoS ONE **10**, e0142949 (2015).
173. G. Zheng, X. Ou, R. Horstmeyer, and C. Yang, "Characterization of spatially varying aberrations for wide field-of-view microscopy," Opt. Express **21**, 15131-15143 (2013).
174. M. Zhang, J. Zhang, Y. Wang, J. Wang, A. M. Achimovich, S. T. Acton, and A. Gahlmann, "Non-invasive single-cell morphometry in living bacterial biofilms," Nat Commun **11**, 6151 (2020).
175. S. H. Lee, M. Baday, M. Tjioe, P. D. Simonson, R. Zhang, E. Cai, and P. R. Selvin, "Using fixed fiduciary markers for stage drift correction," Opt. Express **20**, 12177-12183 (2012).
176. K. Pha, and L. Navarro, "Yersinia type III effectors perturb host innate immune responses," World J Biol Chem **7**, 1-13 (2016).
177. J. M. Flynn, I. Levchenko, R. T. Sauer, and T. A. Baker, "Modulating substrate choice: the SspB adaptor delivers a regulator of the extracytoplasmic-stress response to the AAA+ protease ClpXP for degradation," Genes Dev **18**, 2292-2301 (2004).
178. R. Galland, G. Grenci, A. Aravind, V. Viasnoff, V. Studer, and J. B. Sibarita, "3D high- and super-resolution imaging using single-objective SPIM," Nat. Methods **12**, 641-644 (2015).
179. A. K. Gustavsson, P. N. Petrov, and W. E. Moerner, "Light sheet approaches for improved precision in 3D localization-based super-resolution imaging in mammalian cells [Invited]," Opt. Express **26**, 13122-13147 (2018).
180. Y. Yang, W. Chen, J. L. Fan, and N. Ji, "Adaptive optics enables aberration-free single-objective remote focusing for two-photon fluorescence microscopy," Biomed Opt Express **12**, 354-366 (2021).
181. W. Wang, B. Wu, B. Zhang, X. Li, and J. Tan, "Correction of refractive index mismatch-induced aberrations under radially polarized illumination by deep learning," Opt. Express **28**, 26028-26040 (2020).
182. A. Szymborska, A. de Marco, N. Daigle, V. C. Cordes, J. A. G. Briggs, and J. Ellenberg, "Nuclear Pore Scaffold Structure Analyzed by Super-Resolution Microscopy and Particle Averaging," Science **341**, 655-658 (2013).
183. D. Salas, A. Le Gall, J. B. Fiche, A. Valeri, Y. Ke, P. Bron, G. Bellot, and M. Nollmann, "Angular reconstitution-based 3D reconstructions of nanomolecular structures from superresolution light-microscopy images," Proc. Natl. Acad. Sci. U. S. A. **114**, 9273-9278 (2017).
184. C. Sieben, N. Banterle, K. M. Douglass, P. Gonczy, and S. Manley, "Multicolor single-particle reconstruction of protein complexes," Nat. Methods **15**, 777-780 (2018).
185. S. Weisenburger, D. Boening, B. Schomburg, K. Giller, S. Becker, C. Griesinger, and V. Sandoghdar, "Cryogenic optical localization provides 3D protein structure data with Angstrom resolution," Nat. Methods **14**, 141-144 (2017).
186. F. C. Zanacchi, C. Manzo, A. S. Alvarez, N. D. Derr, M. F. Garcia-Parajo, and M. Lakadamyali, "A DNA origami platform for quantifying protein copy number in super-resolution," Nat. Methods **14**, 789-792 (2017).
187. I. Golding, and E. C. Cox, "Physical nature of bacterial cytoplasm," Phys Rev Lett **96**, 098102 (2006).
188. D. S. Banks, and C. Fradin, "Anomalous diffusion of proteins due to molecular crowding," Biophys J **89**, 2960-2971 (2005).

189. M. Hauser, M. Wojcik, D. Kim, M. Mahmoudi, W. Li, and K. Xu, "Correlative Super-Resolution Microscopy: New Dimensions and New Opportunities," Chem Rev (2017).
190. F. Chen, P. W. Tillberg, and E. S. Boyden, "Expansion microscopy," Science **347**, 543 (2015).
191. P. W. Tillberg, F. Chen, K. D. Piatkevich, Y. Zhao, C. C. Yu, B. P. English, L. Gao, A. Martorell, H. J. Suk, F. Yoshida, E. M. DeGennaro, D. H. Roossien, G. Gong, U. Seneviratne, S. R. Tannenbaum, R. Desimone, D. Cai, and E. S. Boyden, "Protein-retention expansion microscopy of cells and tissues labeled using standard fluorescent proteins and antibodies," Nat. Biotechnol. **34**, 987-992 (2016).
192. T. J. Chozinski, A. R. Halpern, H. Okawa, H. J. Kim, G. J. Tremel, R. O. Wong, and J. C. Vaughan, "Expansion microscopy with conventional antibodies and fluorescent proteins," Nat. Methods **13**, 485-488 (2016).
193. J. B. Chang, F. Chen, Y. G. Yoon, E. E. Jung, H. Babcock, J. S. Kang, S. Asano, H. J. Suk, N. Pak, P. W. Tillberg, A. T. Wassie, D. Cai, and E. S. Boyden, "Iterative expansion microscopy," Nat. Methods **14**, 593-599 (2017).
194. O. M'Saad, and J. Bewersdorf, "Light microscopy of proteins in their ultrastructural context," Nat Commun **11**, 3850 (2020).
195. A. Diepold, and S. Wagner, "Assembly of the bacterial type III secretion machinery," FEMS Microbiol Rev **38**, 802-822 (2014).